

Kinetics of Strand Displacement Reaction with Acyclic Artificial Nucleic Acids, and Its Application to Multiplexed Fluorescent Imaging

(非環状型人工核酸の鎖置換反応の反応速度解析と多分子蛍光イメージングへの応用)

MAKINO Koki

牧野 航海

2023

Table of contents

Chapter 1. General Introduction.....	1
1-1. DNA: deoxyribonucleic acid	1
1-2. Nucleic acid nanotechnology.....	2
1-3. Strand displacement reaction	4
1-4. Artificial nucleic acids for strand displacement reaction	6
1-5. Acyclic nucleic acids: D- <i>a</i> TNA, SNA, L- <i>a</i> TNA	7
1-6. Purpose of this study	8
1-7. References.....	10
Chapter 2. Development of Color-Changing Fluorescent Barcode (CCFB) Using Strand Displacement Reaction.....	14
2-1. Abstract.....	14
2-2. Introduction.....	15
2-3. Design of color-changing fluorescent barcode (CCFB).....	16
2-4. Results and discussions.....	18
2-4-1. Fluorescent color changes of CCFB.....	18
2-4-2. <i>In vitro</i> multiplexed CCFB imaging on beads	21
2-4-3. <i>In situ</i> Protein imaging with CCFB.....	23
2-4-4. The design for sequential fluorescence color changes with CCFB.....	29
2-5. Conclusion	31
2-6. Experimental section	32
2-7. Reference	37
2-8. Appendixes.....	40
Chapter 3. Kinetics of Strand Displacement Reaction with Acyclic Artificial Nucleic Acids.....	61
3-1. Abstract.....	61
3-2. Introduction.....	61

3-3. Design to study kinetics of strand displacement reaction	64
3-4. Results and discussions.....	65
3-4-1. Heterochiral strand displacement reaction with artificial nucleic acids	65
3-4-2. The kinetics of strand displacement reaction with artificial nucleic acids	67
3-4-3. Thermodependency of strand displacement reaction.....	68
3-4-4. Orthogonal strand displacement reaction system.....	70
3-5. Conclusion	71
3-6. Experimental section	72
3-7. Reference	74
3-8. Appendixes.....	76
List of Publications	83
List of Presentations.....	83
List of Awards.....	84
Acknowledgment.....	85

Chapter 1. General Introduction

1-1. DNA: deoxyribonucleic acid

Deoxyribonucleic acid (DNA) is one of the essential biopolymers for all living things because DNA carried genetic information to maintain their lives. DNA consists of deoxyribose, phosphodiester linkage, and nucleobases including Adenine (A), Thymine (T), Guanine (G), and Cytosine (C) (Figure 1-1). Adenine bonds only to thymine with two hydrogen bonds, and guanine bonds only to cytosine with three hydrogen bonds. These complementary base pairings, termed Watson-Crick base pairing rule¹ in which T-A and C-G recognize each other, allow DNA to form B-form right-handed double helix with a complementary base sequence oligomer. This duplex formation is the essential ability to store and transmit genetic information for living organisms. From the viewpoint of molecular biochemistry, this property is unique and will extend widely research such as nucleic acid chemistry and nucleic acid nanotechnology. The development of DNA synthetic techniques such as phosphoramidite chemistry² also contributes to accelerating the development of DNA nanotechnology.

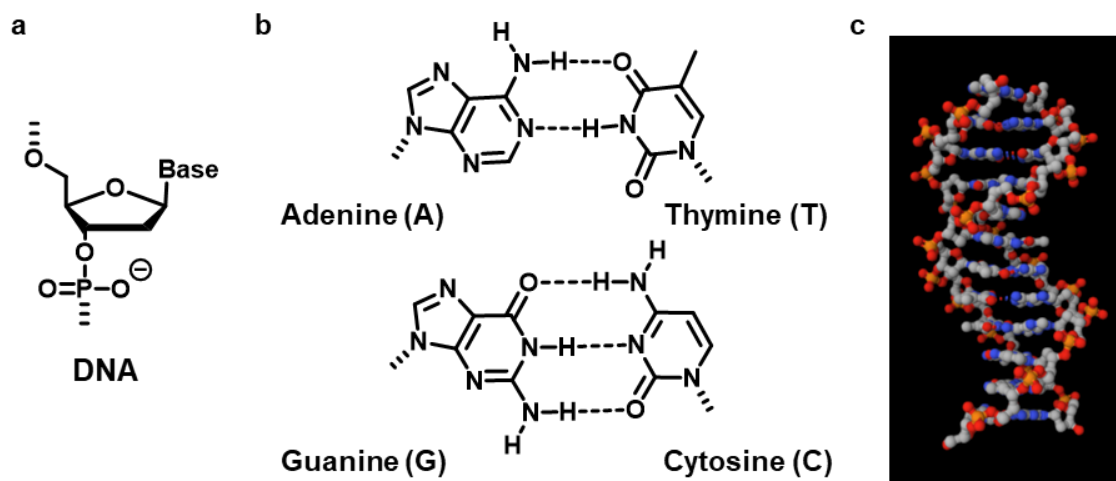


Figure 1-1. (a) Chemical structure of deoxyribonucleic acid (DNA). (b) Watson-Crick base pairs of A-T and G-C. (c) The structure of DNA double helix (created from PDB ID65³).

1-2. Nucleic acid nanotechnology

As described in chapter 1-1, DNA has great predictable and programable interactions based on the Watson-Crick base pairing rule. These features enable researchers to build various DNA nanostructures. In the 1980s, Seeman *et al.* have reported 2D DNA lattices by connecting sticky ends in branched junctions⁴, and 3D cube-like structure with the connection of three arm junctions⁵ (Figure 1-2).

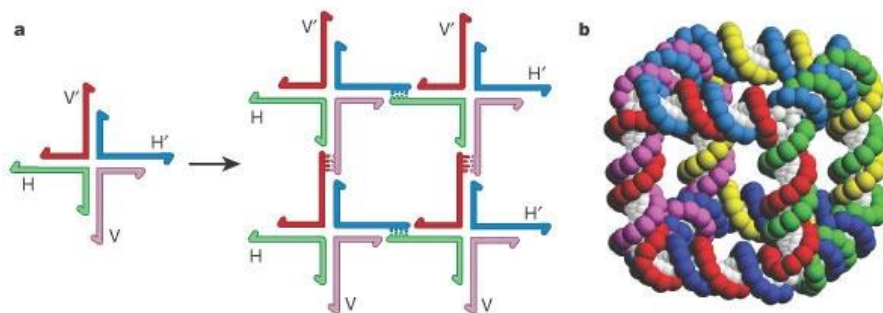


Figure 1-2. (a) 2D DNA lattices by branched junctions through Watson-Crick base pairing. (b) The 3D cube consists of six cyclic strands. Reprinted from Ref. 5.

DNA origami⁶ is one of the central technologies in the field of DNA nanotechnology, based on the folding a long DNA strand into arbitrary structures in the presence of short synthetic oligomers⁷ (Figure 1-3). This DNA origami is a versatile and simple method for folding over 7-kilobase single-strand DNA into a desired shape structure, such as a star, smiley, and triangle as shown in Figure 1-3b. Researchers have extended the DNA origami into three-dimensional DNA

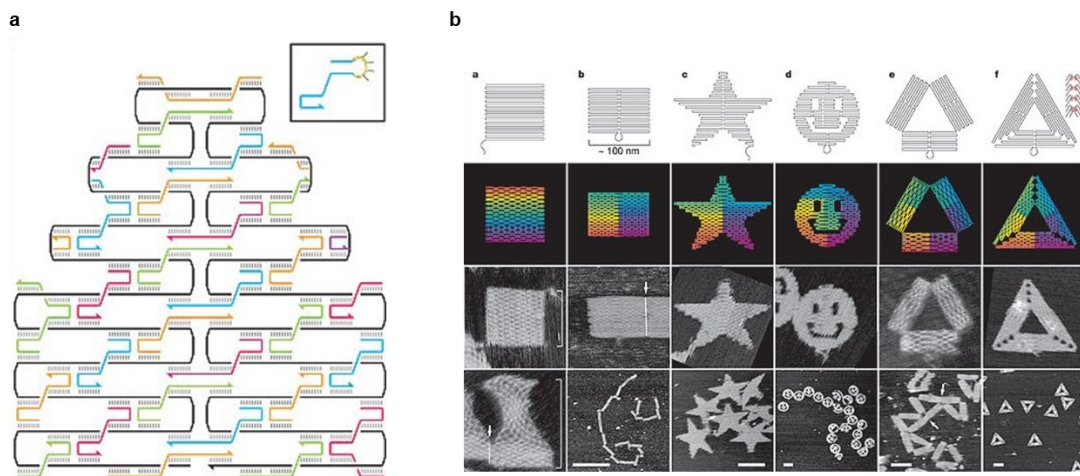


Figure 1-3. (a) Schematic illustration of DNA origami construction (b) Atomic force microscopy (AFM) images of DNA origami. Reprinted from Ref. 6.

nanostructures⁸⁻¹¹ (Figure 1-4). As described above, DNA can form arbitrary 2D and 3D structures using many reported approaches. In addition to that, DNA nanostructures provide functionalized nanodevices with responding to single biomolecules¹² or cells¹³. The rational designability of DNA origami also enables to construct a DNA nanorobot for cancer therapy¹⁴ and multiple fluorescent labeling methods^{15 16}. Therefore, DNA has a lot of potentials to create nanostructures as scaffolds and develop a functional nanodevice for biological research.

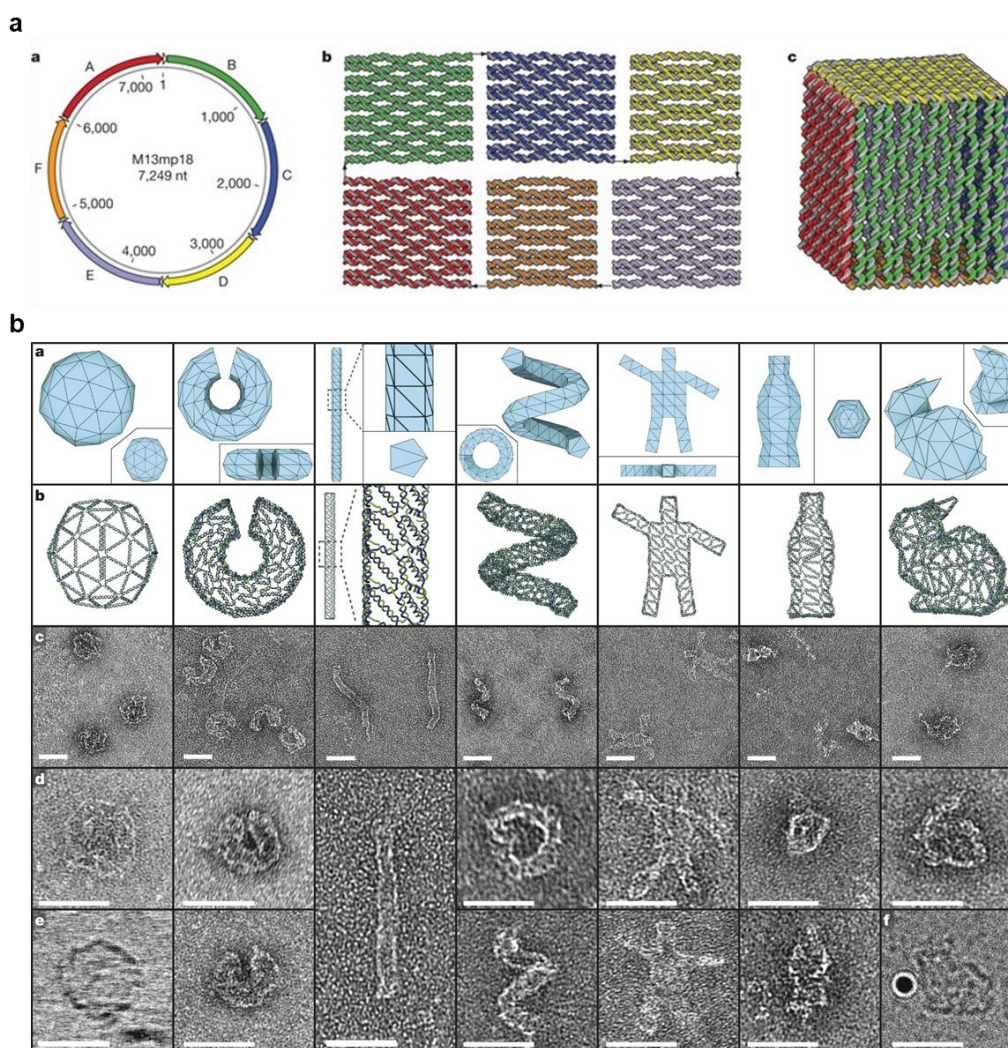


Figure 1-4. (a) Design of a 3D DNA origami hollow box. (b) DNA origami structures of polyhedral digital meshes. Panel a is reprinted from Ref. 8. Panel b is reprinted from Ref. 11.

1-3. Strand displacement reaction

DNA strand displacement reaction is another one of the important DNA nanotechnologies. The concept of DNA strand displacement reaction was proposed by Yurke *et. al.* as a DNA tweezer, and the reaction became an important role in dynamic DNA machines ¹⁷ (Figure 1-5a). This DNA tweezer transforms its structure which can be closed by the addition of a DNA fuel strand or opened by the addition of a complementary strand to the fuel strand. This reaction is initiated by hybridization in the toehold region, followed by branch migration for reassembling the DNA duplex allows removing the initial hybridized strand because more stable duplexes formed.

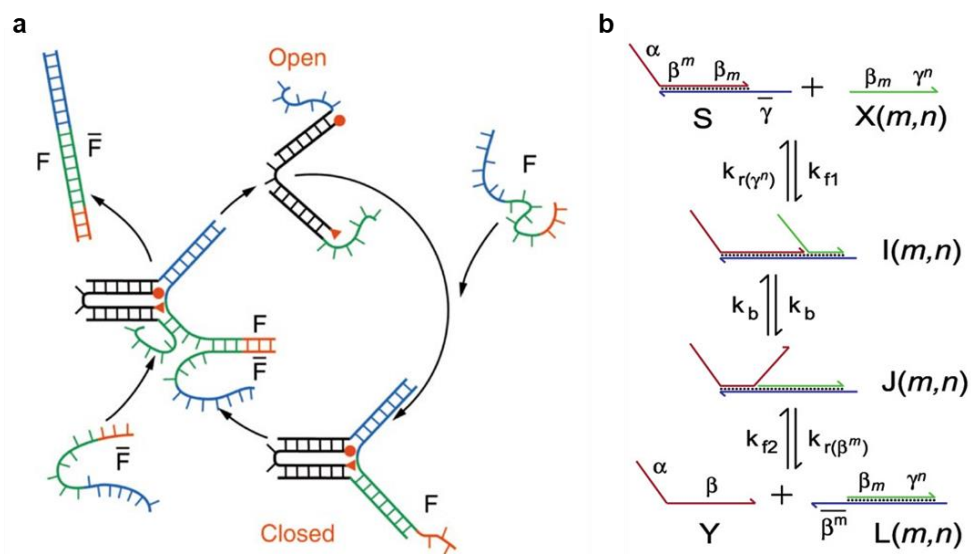


Figure 1-5. (a) DNA tweezer (b) Schematic illustration of DNA toehold mediated strand displacement (exchange) reaction. Panel a is reprinted from Ref. 17. Panel b is reprinted from Ref. 29.

Isothermal strand displacement reaction is also used to enable switching a DNA tile conformation ¹⁸⁻¹⁹. Moreover, DNA machines where conformation change gives some functions have been reported such as the DNA walker method in which DNA units can walk along a pre-designed DNA track ^{20 21}. Using DNA walking technology, a DNA robot that walks autonomously on the cell membrane and activates signal pathways has developed ²².

In a different concept within strand displacement reaction, hybridization chain reaction (HCR) is a remarkable method²³, in which two DNA hairpins hybridize in a cascade only when an input DNA strand is added. The combination of the HCR method and *in situ* hybridization method allows amplified fluorescent signals for sensing target mRNAs²⁴⁻²⁵. This kind of Strand displacement reaction, which can turn fluorescence ON/OFF, is highly compatible with DNA/RNA detection, and promote researchers to develop detection systems²⁶. Toehold switches method, reported by Peng Yin *et al.*, achieves gene expression activation by changing RNA loops into duplexes through toehold-mediated strand displacement reaction²⁷. In addition, the combination of the CRISPR system and the programmability of strand displacement reaction in gRNA allows for the detection of mRNA and regulation of transcriptions²⁸. Notably, strand displacement reaction has been used in a wide range of fields from material science to biological research.

The fundamental kinetics of the DNA strand displacement reaction is well understood, including the effects of the toehold length²⁹. In addition, the authors also proposed an effective design for the reduction of the leak reaction³⁰. These studies are very useful for rational DNA circuit designs.

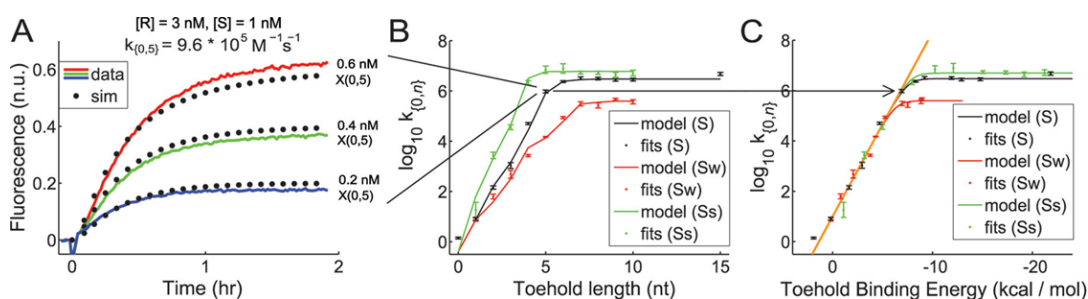


Figure 1-6. Kinetics of DNA toehold-mediated strand displacement reaction. Summary of reaction rate plotted against the invading toehold length or binding energy of the toehold. Reprinted from Ref. 29.

1-4. Artificial nucleic acids for strand displacement reaction

As mentioned above, DNA is not only a biopolymer with genetic information but a versatile nanomaterial for constructing nanostructures or nanorobots. However, the properties of DNA, such as moderate thermal stability, low nuclease resistance, and reactivity with natural DNA or RNA have limited its further applications to functional materials. In this context, researchers have synthesized various types of artificial nucleic acids to improve their abilities³¹⁻³⁴.

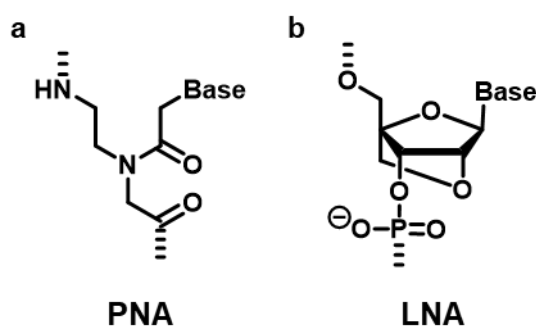


Figure 1-7. Chemical structure of (a) PNA^{35 36} and (b) LNA (BNA)^{37-38 39}.

A few artificial nucleic acids have been combined with strand displacement reactions for exploring new functions. For example, peptide nucleic acid (PNA) is one of the unique nucleic acids in which monomers were connected by no charged peptide bonds (Figure 1-7a)^{35 36}. PNA forms highly stable duplex and triplex due to the reduction of electron repulsion. The different backbone from DNA is not recognized by enzymes and has digestive resistance by nuclease or protease. PNA is a unique analog that has an achiral backbone and hybridizes with D-DNA or L-DNA regardless of chirality⁴⁰. A heterochiral DNA system in which PNA mediates the strand displacement reaction between D-DNA and L-DNA has been proposed (Figure 1-8a)⁴¹⁻⁴². Locked nucleic acid (LNA)³⁷ which is also known as bridged nucleic acid (BNA)^{38 39} is widely used due to its improved affinity in base pairing (Figure 1-7b). Kinetics of strand displacement reaction with oligonucleotides incorporating LNA were investigated for leakage suppression (Figure 1-8b)⁴³.

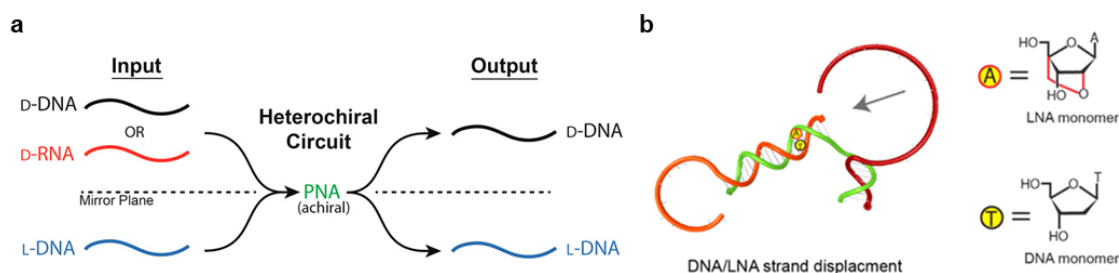


Figure 1-8. (a) Heterochiral DNA strand displacement reaction with PNA interface. (b) Hybrid DNA/LNA strand displacement reaction system. Panel a is reprinted from Ref. 41. Panel b is reprinted from Ref. 43.

Artificial nucleic acids used in strand displacement reactions promise to improve thermal and biological stability and to express novel chemical and structural functions. Although many types of nucleic acid analogs have been developed, only a few have been applied to strand displacement reactions, much less elucidated the reaction kinetics. The understanding of strand displacement reaction using artificial nucleic acids will contribute to the advancement of DNA nanotechnology research and the understanding of DNA itself.

1-5. Acyclic nucleic acids: D-*a*TNA, SNA, L-*a*TNA

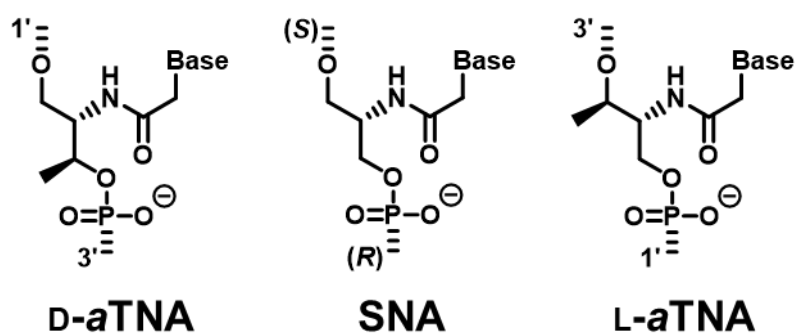


Figure 1-9. Chemical structure of D-*a*TNA⁴⁴, SNA⁴⁵, and L-*a*TNA⁴⁶ developed in our group.

Our group has also developed three types of acyclic artificial nucleic acids, acyclic D-threoninol nucleic acid (D-*a*TNA)⁴⁴, serinol nucleic acid (SNA)⁴⁵, and L-threoninol nucleic acid (L-*a*TNA)⁴⁶ (Figure 1-9). In the beginning, D-threoninol was used as a scaffold to introduce a dye into the DNA duplex for easy incorporation⁴⁷. After that D-*a*TNA oligomers composed of nucleobase

confirmed the very stable homo-duplexes, but no formation with natural nucleic acids was observed. Next, SNA in which the methyl group was removed from D-threosinol backbone was reported. SNA forms a stable homo-duplex and forms a hetero-duplex with DNA and RNA unlike D-*a*TNA, whereas SNA also hybridizes with D-*a*TNA. This remarkable hybridizing ability with any nucleic acids results from the achiral backbone of the SNA monomer. Interestingly, SNA oligomer with a symmetrical sequence is achiral, which is possible to develop a helical amplification system^{48 49}. L-*a*TNA, an enantiomer of D-*a*TNA, was reported as a novel artificial nucleic acid that forms a more stable duplex with DNA and RNA than SNA. Notably, D-*a*TNA forms a left-handed duplex depending on the methyl group position in the backbone, resulting in no formation with DNA and RNA. In contrast, L-*a*TNA forms a right-handed duplex and hetero-duplex with natural nucleic acids due to the same helicity as DNA and RNA. SNA forms a duplex with D-*a*TNA and L-*a*TNA even though they are each in opposite helicity because SNA has a low helical preference and can form both right-handed and left-handed helix³⁴. The resistance to enzymatic digestion of artificial nucleic acids is an important property for intracellular applications, these developed nucleic acids are highly resistant to nuclease and protease due to their very different backbone⁵⁰.

As described above, D-*a*TNA, SNA, and L-*a*TNA have excellent abilities such as high thermal stability, biological stability, and hetero-chiral duplex formation. Our group has reported some applications including systems using strand displacement reaction^{51 52}.

1-6. Purpose of this study

This study aims to apply these promising acyclic artificial nucleic acids to strand displacement reactions and develop a multiple imaging method. This new method, we call Color-Changing Fluorescent Barcode (CCFB), uses D-*a*TNA that forms very stable duplex and has orthogonal to intracellular conditions. In the CCFB method, the strand displacement reaction allows fluorescence color changes in the pre-determined order. These color changes provide color sequences for multiple labeling.

Another aim of this study is to systematically clarify the kinetics of strand displacement reactions using acyclic nucleic acids, SNA, L-*a*TNA, and D-*a*TNA. As mentioned in chapter 1-5,

we have developed some techniques using strand displacement reaction with these nucleic acids. However, the kinetics of the reaction remain unraveled. Herein, we mainly study the effects of toehold length in the kinetics of strand displacement reaction using acyclic artificial nucleic acids. Our results will promote the applications using SNA, L-*a*TNA, and *a*TNA, and developments of highly functional technologies that are available in biological conditions.

1-7. References

1. Watson, J. D.; Crick, F. H. C., Genetical Implications of the Structure of Deoxyribonucleic Acid. *Nature* **1953**, *171* (4361), 964-967.
2. Beaucage, S. L.; Caruthers, M. H., Deoxynucleoside phosphoramidites—A new class of key intermediates for deoxypolynucleotide synthesis. *Tetrahedron Lett.* **1981**, *22* (20), 1859-1862.
3. Edwards, K. J.; Brown, D. G.; Spink, N.; Skelly, J. V.; Neidle, S., Molecular structure of the B-DNA dodecamer d(CGCAAATTTGCG)₂ An examination of propeller twist and minor-groove water structure at 2·2Å resolution. *JMBio* **1992**, *226* (4), 1161-1173.
4. Seeman, N. C., Nucleic acid junctions and lattices. *JTBio* **1982**, *99* (2), 237-247.
5. Chen, J.; Seeman, N. C., Synthesis from DNA of a molecule with the connectivity of a cube. *Nature* **1991**, *350* (6319), 631-633.
6. Rothmund, P. W. K., Folding DNA to create nanoscale shapes and patterns. *Nature* **2006**, *440* (7082), 297-302.
7. Shih, W. M.; Quispe, J. D.; Joyce, G. F., A 1.7-kilobase single-stranded DNA that folds into a nanoscale octahedron. *Nature* **2004**, *427* (6975), 618-621.
8. Andersen, E. S.; Dong, M.; Nielsen, M. M.; Jahn, K.; Subramani, R.; Mamdouh, W.; Golas, M. M.; Sander, B.; Stark, H.; Oliveira, C. L. P.; Pedersen, J. S.; Birkedal, V.; Besenbacher, F.; Gothelf, K. V.; Kjems, J., Self-assembly of a nanoscale DNA box with a controllable lid. *Nature* **2009**, *459* (7243), 73-76.
9. Douglas, S. M.; Dietz, H.; Liedl, T.; Högberg, B.; Graf, F.; Shih, W. M., Self-assembly of DNA into nanoscale three-dimensional shapes. *Nature* **2009**, *459* (7245), 414-418.
10. Ke, Y.; Sharma, J.; Liu, M.; Jahn, K.; Liu, Y.; Yan, H., Scaffolded DNA Origami of a DNA Tetrahedron Molecular Container. *Nano Lett.* **2009**, *9* (6), 2445-2447.
11. Benson, E.; Mohammed, A.; Gardell, J.; Masich, S.; Czeizler, E.; Orponen, P.; Högberg, B., DNA rendering of polyhedral meshes at the nanoscale. *Nature* **2015**, *523* (7561), 441-444.
12. Kuzuya, A.; Sakai, Y.; Yamazaki, T.; Xu, Y.; Komiyama, M., Nanomechanical DNA origami 'single-molecule beacons' directly imaged by atomic force microscopy. *Nat. Commun.* **2011**, *2* (1), 449.
13. Douglas, S. M.; Bachelet, I.; Church, G. M., A Logic-Gated Nanorobot for Targeted Transport of Molecular Payloads. *Science* **2012**, *335* (6070), 831-834.
14. Liu, S.; Jiang, Q.; Zhao, X.; Zhao, R.; Wang, Y.; Wang, Y.; Liu, J.; Shang, Y.; Zhao, S.; Wu, T.; Zhang, Y.; Nie, G.; Ding, B., A DNA nanodevice-based vaccine for cancer immunotherapy. *Nature Materials* **2021**, *20* (3), 421-430.
15. Lin, C.; Jungmann, R.; Leifer, A. M.; Li, C.; Levner, D.; Church, G. M.; Shih, W. M.; Yin, P., Submicrometre geometrically encoded fluorescent barcodes self-assembled from DNA. *Nat. Chem.* **2012**, *4* (10), 832-839.

16. Woehrstein, J. B.; Strauss, M. T.; Ong, L. L.; Wei, B.; Zhang, D. Y.; Jungmann, R.; Yin, P., Sub-100-nm metafluorophores with digitally tunable optical properties self-assembled from DNA. *Science Advances* **2017**, *3* (6), e1602128.
17. Yurke, B.; Turberfield, A. J.; Mills, A. P.; Simmel, F. C.; Neumann, J. L., A DNA-fuelled molecular machine made of DNA. *Nature* **2000**, *406* (6796), 605-608.
18. Yan, H.; Zhang, X.; Shen, Z.; Seeman, N. C., A robust DNA mechanical device controlled by hybridization topology. *Nature* **2002**, *415* (6867), 62-65.
19. Feng, L.; Park, S. H.; Reif, J. H.; Yan, H., A Two-State DNA Lattice Switched by DNA Nanoactuator. *Angew. Chem. Int. Ed.* **2003**, *42* (36), 4342-4346.
20. Shin, J.-S.; Pierce, N. A., A Synthetic DNA Walker for Molecular Transport. *J. Am. Chem. Soc.* **2004**, *126* (35), 10834-10835.
21. Omabegho, T.; Sha, R.; Seeman, N. C., A Bipedal DNA Brownian Motor with Coordinated Legs. *Science* **2009**, *324* (5923), 67-71.
22. Li, H.; Gao, J.; Cao, L.; Xie, X.; Fan, J.; Wang, H.; Wang, H.-H.; Nie, Z., A DNA Molecular Robot that Autonomously Walks on the Cell Membrane to Drive Cell Motility. *Angew. Chem. Int. Ed.* **2021**, *60* (50), 26087-26095.
23. Dirks, R. M.; Pierce, N. A., Triggered amplification by hybridization chain reaction. *Proceedings of the National Academy of Sciences* **2004**, *101* (43), 15275-15278.
24. Choi, H. M. T.; Chang, J. Y.; Trinh, L. A.; Padilla, J. E.; Fraser, S. E.; Pierce, N. A., Programmable in situ amplification for multiplexed imaging of mRNA expression. *Nat. Biotechnol.* **2010**, *28* (11), 1208-1212.
25. Choi, H. M. T.; Beck, V. A.; Pierce, N. A., Next-Generation in Situ Hybridization Chain Reaction: Higher Gain, Lower Cost, Greater Durability. *ACS Nano* **2014**, *8* (5), 4284-4294.
26. Mohammadniaei, M.; Zhang, M.; Ashley, J.; Christensen, U. B.; Friis-Hansen, L. J.; Gregersen, R.; Lisby, J. G.; Benfield, T. L.; Nielsen, F. E.; Henning Rasmussen, J.; Pedersen, E. B.; Olinger, A. C. R.; Kolding, L. T.; Naseri, M.; Zheng, T.; Wang, W.; Gorodkin, J.; Sun, Y., A non-enzymatic, isothermal strand displacement and amplification assay for rapid detection of SARS-CoV-2 RNA. *Nat. Commun.* **2021**, *12* (1), 5089.
27. Green, Alexander A.; Silver, Pamela A.; Collins, James J.; Yin, P., Toehold Switches: De-Novo-Designed Regulators of Gene Expression. *Cell* **2014**, *159* (4), 925-939.
28. Oesinghaus, L.; Simmel, F. C., Switching the activity of Cas12a using guide RNA strand displacement circuits. *Nat. Commun.* **2019**, *10* (1), 2092.
29. Zhang, D. Y.; Winfree, E., Control of DNA Strand Displacement Kinetics Using Toehold Exchange. *J. Am. Chem. Soc.* **2009**, *131* (47), 17303-17314.

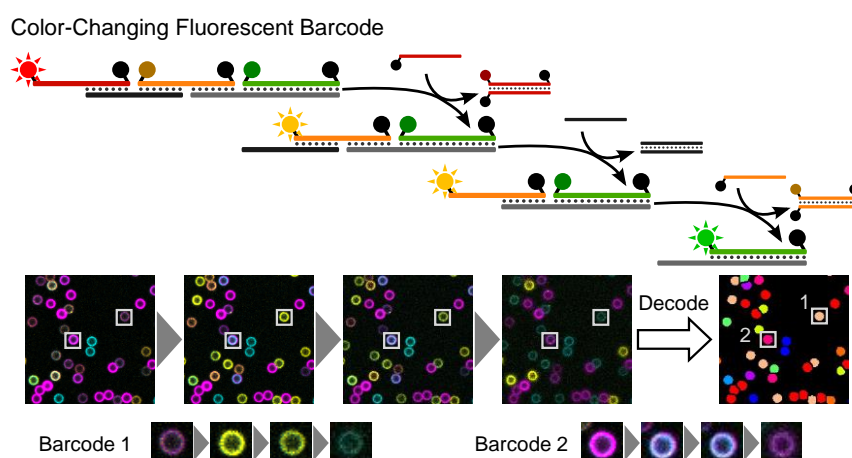
30. Wang, B.; Thachuk, C.; Ellington, A. D.; Winfree, E.; Soloveichik, D., Effective design principles for leakless strand displacement systems. *Proceedings of the National Academy of Sciences* **2018**, *115* (52), E12182-E12191.
31. Hirao, I.; Kimoto, M.; Yamashige, R., Natural versus Artificial Creation of Base Pairs in DNA: Origin of Nucleobases from the Perspectives of Unnatural Base Pair Studies. *Acc. Chem. Res.* **2012**, *45* (12), 2055-2065.
32. McKenzie, L. K.; El-Khoury, R.; Thorpe, J. D.; Damha, M. J.; Hollenstein, M., Recent progress in non-native nucleic acid modifications. *ChSRv* **2021**, *50* (8), 5126-5164.
33. Morihira, K.; Kasahara, Y.; Obika, S., Biological applications of xeno nucleic acids. *Mol. Biosyst.* **2017**, *13* (2), 235-245.
34. Murayama, K.; Asanuma, H., Design and Hybridization Properties of Acyclic Xeno Nucleic Acid Oligomers. *ChemBioChem* **2021**, *22* (15), 2507-2515.
35. Nielsen, P. E.; Egholm, M.; Berg, R. H.; Buchardt, O., Sequence-Selective Recognition of DNA by Strand Displacement with a Thymine-Substituted Polyamide. *Science* **1991**, *254* (5037), 1497-1500.
36. Wittung, P.; Nielsen, P. E.; Buchardt, O.; Egholm, M.; Norde'n, B., DNA-like double helix formed by peptide nucleic acid. *Nature* **1994**, *368* (6471), 561-563.
37. K. Singh, S.; A. Koshkin, A.; Wengel, J.; Nielsen, P., LNA (locked nucleic acids): synthesis and high-affinity nucleic acid recognition. *Chem. Commun.* **1998**, (4), 455-456.
38. Obika, S.; Nanbu, D.; Hari, Y.; Morio, K.-i.; In, Y.; Ishida, T.; Imanishi, T., Synthesis of 2' - O,4' -C-methyleneuridine and -cytidine. Novel bicyclic nucleosides having a fixed C3, -endo sugar pucker. *Tetrahedron Lett.* **1997**, *38* (50), 8735-8738.
39. Obika, S.; Nanbu, D.; Hari, Y.; Andoh, J.-i.; Morio, K.-i.; Doi, T.; Imanishi, T., Stability and structural features of the duplexes containing nucleoside analogues with a fixed N-type conformation, 2' -O,4' -C-methylenribonucleosides. *Tetrahedron Lett.* **1998**, *39* (30), 5401-5404.
40. Froeyen, M.; Morvan, F.; Vasseur, J.-J.; Nielsen, P.; Van Aerschot, A.; Rosemeyer, H.; Herdewijn, P., Conformational and Chiral Selection of Oligonucleotides. *Chem. Biodivers.* **2007**, *4* (4), 803-817.
41. Kabza, A. M.; Young, B. E.; Sczepanski, J. T., Heterochiral DNA Strand-Displacement Circuits. *J. Am. Chem. Soc.* **2017**, *139* (49), 17715-17718.
42. Kundu, N.; Young, B. E.; Sczepanski, J. T., Kinetics of heterochiral strand displacement from PNA-DNA heteroduplexes. *Nucleic Acids Res.* **2021**, *49* (11), 6114-6127.
43. Olson, X.; Kotani, S.; Yurke, B.; Graugnard, E.; Hughes, W. L., Kinetics of DNA Strand Displacement Systems with Locked Nucleic Acids. *The Journal of Physical Chemistry B* **2017**, *121* (12), 2594-2602.
44. Asanuma, H.; Toda, T.; Murayama, K.; Liang, X.; Kashida, H., Unexpectedly Stable Artificial Duplex from Flexible Acyclic Threoninol. *J. Am. Chem. Soc.* **2010**, *132* (42), 14702-14703.

45. Kashida, H.; Murayama, K.; Toda, T.; Asanuma, H., Control of the Chirality and Helicity of Oligomers of Serinol Nucleic Acid (SNA) by Sequence Design. *Angew. Chem. Int. Ed.* **2011**, *50* (6), 1285-1288.
46. Murayama, K.; Kashida, H.; Asanuma, H., Acyclic l-threoninol nucleic acid (l-aTNA) with suitable structural rigidity cross-pairs with DNA and RNA. *Chem. Commun.* **2015**, *51* (30), 6500-6503.
47. Asanuma, H.; Takarada, T.; Yoshida, T.; Tamaru, D.; Liang, X.; Komiyama, M., Enantioselective Incorporation of Azobenzenes into Oligodeoxyribonucleotide for Effective Photoregulation of Duplex Formation. *Angew. Chem. Int. Ed.* **2001**, *40* (14), 2671-2673.
48. Kashida, H.; Nishikawa, K.; Shi, W.; Miyagawa, T.; Yamashita, H.; Abe, M.; Asanuma, H., A helical amplification system composed of artificial nucleic acids. *Chemical Science* **2021**, *12* (5), 1656-1660.
49. Kashida, H.; Nishikawa, K.; Ito, Y.; Murayama, K.; Hayashi, I.; Kakuta, T.; Ogoshi, T.; Asanuma, H., A Pyrene-Modified Serinol Nucleic Acid Nanostructure Converts the Chirality of Threoninol Nucleic Acids into Circularly Polarized Luminescence Signals. *Chemistry – A European Journal* **2021**, *27* (59), 14582-14585.
50. Kamiya, Y.; Donoshita, Y.; Kamimoto, H.; Murayama, K.; Ariyoshi, J.; Asanuma, H., Introduction of 2,6-Diaminopurines into Serinol Nucleic Acid Improves Anti-miRNA Performance. *ChemBioChem* **2017**, *18* (19), 1917-1922.
51. Murayama, K.; Nagao, R.; Asanuma, H., D-aTNA Circuit Orthogonal to DNA Can Be Operated by RNA Input via SNA. *ChemistrySelect* **2017**, *2* (20), 5624-5627.
52. Chen, Y.; Nagao, R.; Murayama, K.; Asanuma, H., Orthogonal Amplification Circuits Composed of Acyclic Nucleic Acids Enable RNA Detection. *J. Am. Chem. Soc.* **2022**, *144* (13), 5887-5892.

Chapter 2. Development of Color-Changing Fluorescent Barcode (CCFB) Using Strand Displacement Reaction

2-1. Abstract

Fluorescent labeling is an essential technology to detect intracellular proteins and nucleic acids because of its high sensitivity and versatility. However, spectral overlaps between the excitation and emission wavelengths limit the detectable targets to usually five. This limitation restricts the application of fluorescence imaging to a comprehensive analysis of biomolecules in cells. Here, we developed a new multiple-labeling methodology where multiple molecules can be detected by barcode labeling of fluorescent color sequences. First, we designed a color-changing fluorescent barcode (CCFB) method using a sequential strand displacement reaction of nucleic acid nanotechnology. Second, we confirmed the capability to change fluorescent color by adding nucleic acid oligomer which induces a toehold-mediated strand displacement reaction, resulting in fluorescent colors successfully changing in the pre-determined order. In addition, nine types of fluorescent barcodes with only three types of fluorophores are discriminated in fluorescent barcode conjugated beads. Finally, we applied CCFB to multiple proteins imaging using barcode antibody conjugates. We demonstrated that four proteins in HeLa cells are detected by CCFB with only three types of fluorophores. Taken together, we have developed CCFB that labels multiple targets beyond the fluorescence limitation.



2-2. Introduction

Fluorescent imaging is a powerful tool for understanding several biological phenomena. However, spectral overlapping of fluorescent molecules restricts the number of detectable targets to about five. This limitation prevents our understanding of complex biological functions involving many biomolecules, DNA, RNA, protein, and any other molecules. Several imaging techniques based on the photophysical approach have been reported for multiple labeling such as vibrational imaging¹⁻² and spectral imaging³⁻⁴. Sequential immunostaining methodologies by using fluorophore-labeled antibodies have also been developed to enable multiplexed protein imaging⁵⁻¹⁰. Although these methods allow multiple protein imaging, complex operation and a long time are required.

As mentioned in chapter 1, the programmability of DNA nanotechnology based on Watson-Crick base pairing also implements multiple labeling methodologies. For example, DNA-barcoding methods using DNA hybridization and dehybridization repeats on DNA-conjugated antibody¹¹⁻¹³. Moreover, Peng Yin *et al.* developed DNA-PAINT technique¹⁴⁻¹⁷ inspired by the PAINT (Points Accumulation In Nanoscale Topography) technique¹⁸. DNA-PAINT technique enables not only multiplexed protein imaging but also high-resolution imaging¹⁹⁻²⁰. They have also reported Immuno-SABER which achieves highly multiplexed and signal-amplifying imaging through DNA-barcoded antibodies²¹. Another group developed a highly multiplexed imaging technique, called co-detection by indexing (CODEX) by using DNA polymerase with fluorescent dNTP analogs²². In addition, multiplexed mRNA imaging such as seqFISH²³⁻²⁴ and MERFISH²⁵ enable transcriptomics analysis by sequential hybridization with readout probes. The multiple imaging methods where targets were labeled by using DNA architecture²⁶⁻²⁷ or nanotechnology²⁸ have also been reported. DNA origami²⁹ and 3D DNA nanorods¹⁵ barcoded by fluorophore-conjugated oligonucleotides allowed discrimination by fluorescent colors but also fluorescence intensity and geometry. However, these DNA architectures cannot be used in the intracellular environment because of the large size complex and low formation efficiency. Moreover, DNA architectures can be disassembled by endogenous DNA and RNA and can be digested by nucleases in an intracellular condition. Therefore, DNA nanotechnology is very useful for developing new multiple methodologies, but there are several issues to create a versatile multiplexed imaging technique.

Herein, we describe the development of a multiplexed imaging methodology that uses a simple linear nucleic acid complex, termed the color-changing fluorescent barcode (CCFB) method (Figure 2-1).

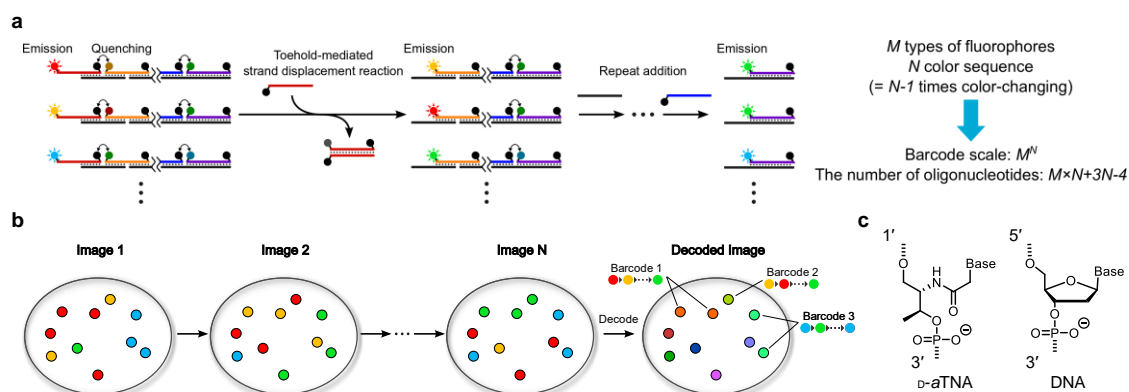


Figure 2-1. The principle of color-changing fluorescent barcode (CCFB) method. (a) Schematic illustration of CCFB complexes composed of oligomers with a fluorophore and a quencher at both ends. In the initial state, only a fluorophore at the end can emit fluorescence, and the other fluorophores are quenched by a neighboring quencher. Subsequently, the addition of a complementary quencher strand induces a toehold-mediated strand displacement reaction and removes the oligomer at the terminal. The first fluorophore is quenched, and the second fluorophore emits fluorescence due to the absence of the neighboring quencher. Reiteration of similar strand displacement reaction changes fluorescence colors in the pre-determined orders. (b) Schematic illustration of CCFB labeling and decoding. The fluorescence colors of each spot are visualized via a fluorescence microscope. Multiple target spots can be identified by decoding the fluorescence color sequence. (c) Chemical structures of D- α TNA and DNA.

2-3. Design of color-changing fluorescent barcode (CCFB)

We developed a method to change the fluorescence color for multiple labeling beyond the fluorescence limitation. In general fluorescent labeling, a single target is labeled by a single fluorophore. However, we devised a strategy that the fluorescence color sequence according to the predetermined order allows us to discriminate multiple targets over five. For example, a fluorescent barcode whose color changes from red to yellow to green to blue is distinguishable from one from yellow to red to green to blue (Figure 2-1b). In this design, the number of distinguishable molecules can be increased exponentially by extending the CCFB design. When CCFB consists of M types of fluorophores and $N-1$ times fluorescence color change, M^N types of discriminable barcodes can be prepared. Moreover, one of the advantages of CCFB is very simple

its structure, thus many probes and complicated oligomer designs are not required. $M \times N$ dye-conjugated oligomers, $N-1$ connecting oligomers, and $2N-3$ complementary oligomers to initiate strand displacement reaction are required, resulting in a total of $M \times N + 3N - 4$ oligomers (Figure 2-1a). When CCFB consists of three types of fluorophores and two times fluorescence color change, $27 = 3^3$ types of barcodes can be prepared with $14 = 3 \times 3 + 3 \times 3 - 4$ oligomers, not 27 probe strands. An additional advantage of CCFB is that washing procedures are not necessary because fluorescence in the removed oligomer is quenched by a complementary oligomer.

We employed artificial nucleic acid D-*a*TNA, as mentioned in chapter 1, as components of CCFB (Figure 2-1c). This D-*a*TNA can form a very stable duplex, but it cannot form a heteroduplex with DNA or RNA. Moreover, D-*a*TNA has a resistance against enzymatic digestion. Therefore, we expected that fluorescent barcodes using D-*a*TNA can avoid unintended interactions with biomolecules: RNA, DNA, and nuclease in cells. Furthermore, our group has reported that the fluorescent probes composed of acyclic nucleic acid have high quenching efficiency and S/B ratio than probes of DNA³⁰.

We synthesized the D-*a*TNA oligomers as a previously reported procedure³¹⁻³² for a fluorescent barcode that has three types of fluorophores and changes emission color twice. Cy5, Cy3, and FAM were used as distinguishable fluorophores, whose spectra are shown in Figure S2-1, and dabcyI was used as a quencher. We first designed CCFB fluorophore strands (F1~F5) that form a 7-mer overlapping duplex, and three quencher strands (Q1~Q3) that are fully complementary to F strands (Figure 2-2). The fluorescence color sequence depends on the fluorophores at F1, F3, and F5 strands, and can be decoded by the same Q strands (Figure S2-2). The addition of Q strands to barcode complexes induced a toehold-mediated strand displacement reaction, and then fluorescence colors change. The oligomer sequences in this experience are listed in Table S2-1.

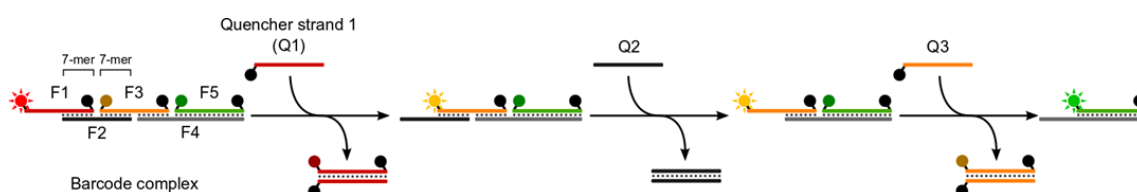


Figure 2-2. Schematic illustration of a CCFB method in this report. F strands with a fluorophore and a quencher are complementary to each other, resulting in forming a 7-mer overlapping linear duplex. The addition of quencher strands (Q1, Q2, and Q3) causes a toehold-mediated strand displacement reaction, and then fluorescent color changes.

2-4. Results and discussions

2-4-1. Fluorescent color changes of CCFB

We first confirmed the color-changing ability by measuring the fluorescence of the barcode complex upon adding Q strands. Q1, Q2, and Q3 were added at 20 °C at 10 min intervals to the barcode complex with a barcode in the order of Cy5→Cy3→FAM, which consisted of Cy5F1, F2, Cy3F3, F4, and FAMF5 (Figure 2-3). In the initial state, Cy5 emission was observed and Cy3 and FAM were quenched, indicating that the F strands can form a desired linear duplex. When Q1 was added, Cy5 was immediately quenched and Cy3 emission was observed due to the displacement of the F1 strand from the barcode complex. Then, the addition of Q2, which has no quencher, changed the fluorescence intensity of Cy3 because the surrounding microenvironment of Cy3 was changed by removing the F2 oligomer (Figure S2-3). On the other hand, When Q3 was added, quenched FAM emission was observed. This result shows that the consecutive strand displacement reaction can change fluorescence color in the pre-designed order of Cy5→Cy3→FAM. We also performed fluorescent measurements for a longer reaction time to confirm the rough reaction rate and the steady-state fluorescence (Figure S2-4). The reaction rates were estimated in the order of Q1 > Q3 > Q2 addition, and the fluorescence intensity of Cy3 was reduced by about half in the steady state when the Q2 added. Notably, the accumulation of Q strands addition would not influence the reaction rates. In addition, the differences in reaction

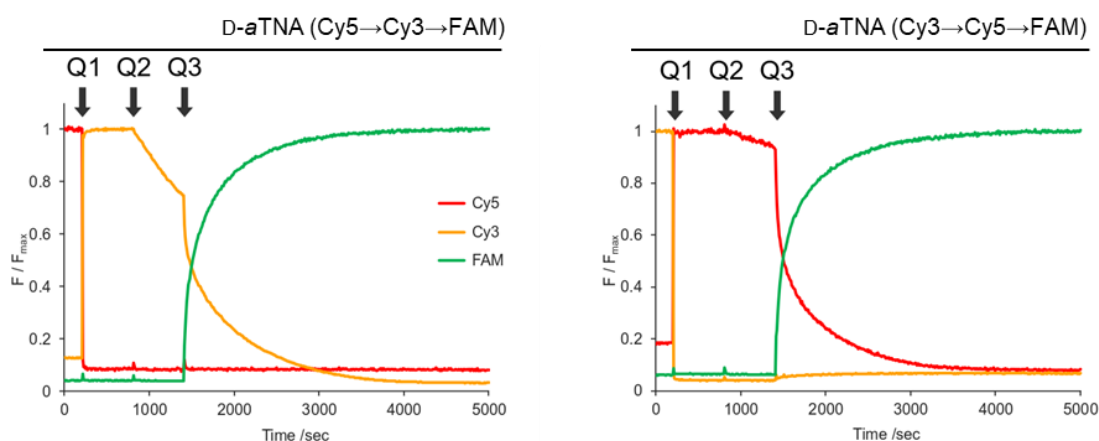


Figure 2-3. The fluorescence color changes upon the addition of Q1, Q2, and Q3 were observed in the order of Cy5→Cy3→FAM (left) and Cy3→Cy5→FAM (right). Q strands were added at the time points indicated by arrows. Fluorescence intensities were normalized by the maximum intensity (F_{max}) of each fluorophore. Conditions: 0.2 μ M barcode complex, 0.4 μ M Q strands, 100 mM NaCl, 10 mM phosphate buffer (pH 7.0), 20°C.

rates would depend on the nucleobase sequence, in which a study about DNA hybridization reported that the repeated nucleobase sequence can increase the hybridization rate³³. Furthermore, no fluorescence changes were observed upon the addition of Q2 or Q3 without Q1 (Figure S2-5). This result implies the high specificity of the strand displacement reaction in this system. Subsequently, to confirm the ability of fluorescence color changes in a different order of barcode, we performed the fluorescence measurement of the barcode complex of Cy3→Cy5→FAM in the same procedure. We synthesized the D-*a*TNA oligomers tethering different fluorophores with the same base sequence, Cy3F1 and Cy5F3 as shown in Table S2-1. The sequential addition of three Q strands to the barcode complex of Cy3→Cy5→FAM, which were composed of Cy3F1, F2, Cy5F3, F4, and FAMF5, caused fluorescence color changes in the desired order (Figure 2-3b).

We next investigated the effects of the length of the D-*a*TNA barcode complex and synthesized D-*a*TNA oligomer for forming 10-mer overlapping complex barcoded Cy5→Cy3→FAM (Figure S2-6 and Table S2-2). When Q1 was added to the barcode complex in the same conditions at 20 °C, quenching of Cy5 and Cy3 emission were observed (Figure S2-6b). However, when Q3 was added, quenching of Cy3 and FAM emission were not observed. This unintended result suggested that the 10-mer overlapping design reduced the reaction rate due to the stabilization of the complex and was insufficient to complete the reaction. The melting temperature T_m of the 10-mer D-*a*TNA complex was about 70 °C, while the T_m of 7-mer D-*a*TNA was about 60 °C (Figure S2-7). At a higher temperature 40 °C, the strand displacement reaction induced the pre-determined fluorescence color change, indicating that a 10-mer overlapping design also worked (Figure S2-6c). Therefore, we concluded that a 7-mer overlapping design is more suitable because this is available at room temperature.

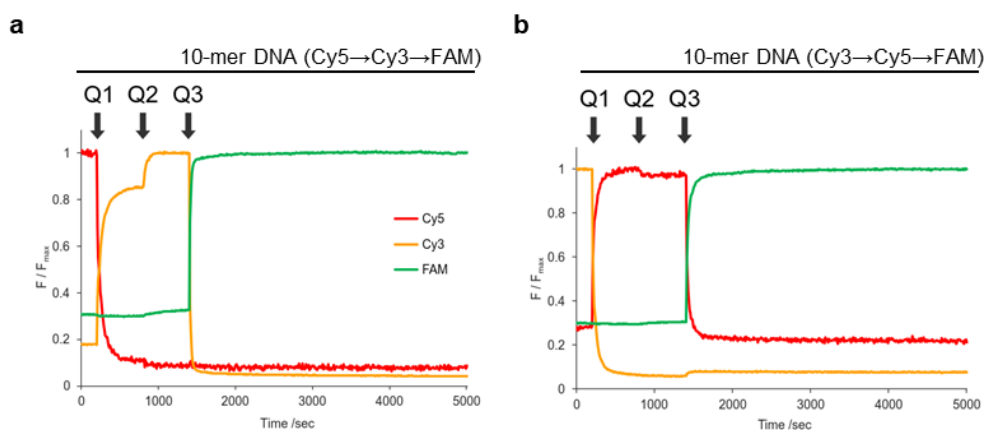


Figure 2-4. The fluorescence color changes upon the addition of Q1, Q2, and Q3 were observed in the order of Cy5→Cy3→FAM (left) and Cy3→Cy5→FAM (right) with 10-mer overlapping DNA CCFB. Q strands were added at the time points indicated by arrows. Fluorescence intensities were normalized by the maximum intensity (F_{max}) of each fluorophore. Conditions: 0.2 μ M barcode complex, 0.4 μ M Q strands, 100 mM NaCl, 10 mM phosphate buffer (pH 7.0), 20 $^{\circ}$ C.

Next, for comparison, we performed a similar experience with a DNA CCFB, which was designed to form a 10-mer overlapping linear duplex (Figure 2-4 and Table S2-3). The results of fluorescence color changes in the intended order indicated that a DNA CCFB also worked like a D-*a*TNA CCFB. However, strong background emissions from the fluorophores that should be quenched were observed. For example, the signal-to-background (S/B) ratio of Cy3 and FAM on DNA were 5.6 and 3.2 respectively, whereas the S/B ratio of Cy3 and FAM on D-*a*TNA were 21.6 and 15.2 (Table S2-4). D-*a*TNA has a quenching efficiency of more than three times higher than that of DNA. This result is consistent with our previous reports that acyclic nucleic acids have higher quenching efficiency than DNA³⁰. This may be because acyclic nucleic acids have strong base pairing and suppress the breathing of barcode duplex. It is also noteworthy that the melting temperature T_m of the 10-mer DNA barcode complex was about 40 $^{\circ}$ C, which was lower than the T_m of the 7-mer D-*a*TNA barcode complex, about 55 $^{\circ}$ C (Figure S2-5). Therefore, the construction of CCFB with D-*a*TNA oligomer shortens the barcode complex and reduces the background emissions. Based on the above, we adopted a 7-mer D-*a*TNA design for the CCFB system.

We also confirmed that CCFB in the other color sequences, a total 27-barcode set, worked from the result of fluorescence color changes as shown in Figures 2-3 and S2-8. Notably, to prepare 27 different barcodes, only 14 D-*a*TNA oligomers were required, which indicates the high simplicity of CCFB.

2-4-2. *In vitro* multiplexed CCFB imaging on beads

To demonstrate the ability of the CCFB approach to detect multiple targets, we conducted fluorescent microscopy imaging of polystyrene beads conjugated barcode complexes. D-*a*TNA oligomers that were modified with biotin at the terminal enabled immobilization on streptavidin-coated beads (Figure 2-5a). Cy5→Cy3→FAM sequence barcoded beads were prepared by mixing appropriate F strands. Fluorescence microscopy images of barcode complex conjugated beads on the glass bottom plate were acquired before and after each addition of Q strands, Q1, Q2, and Q3

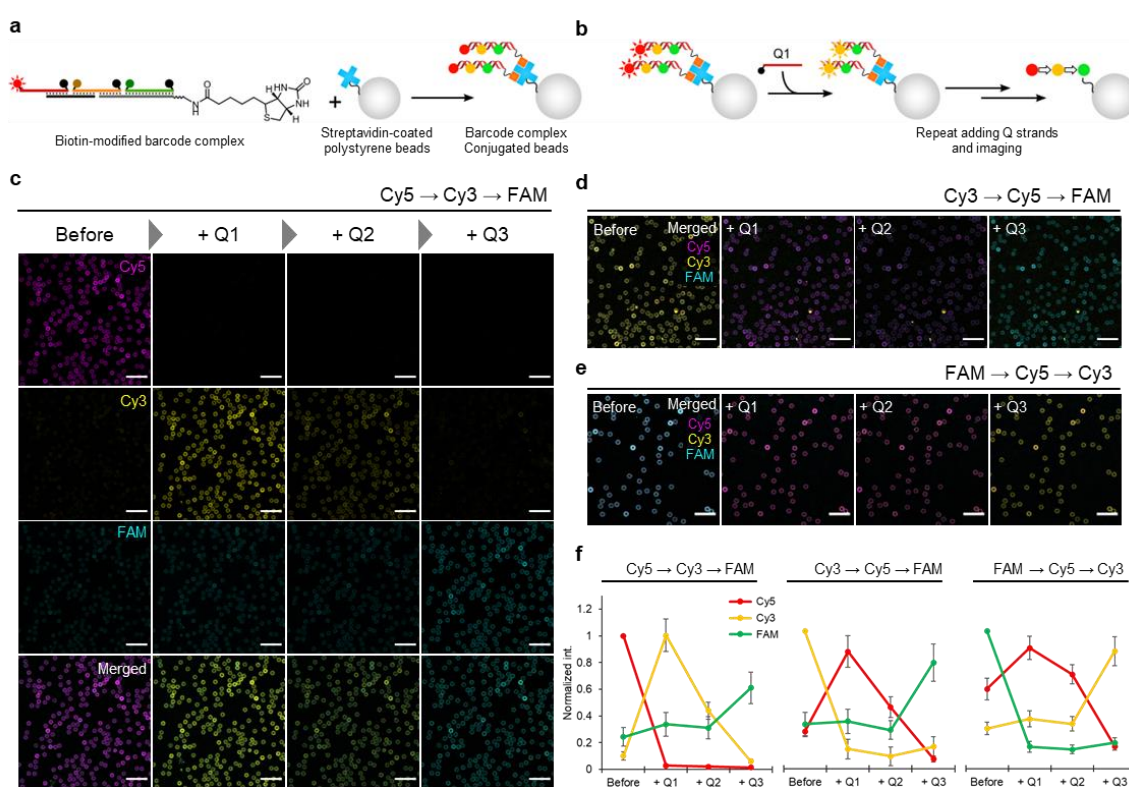


Figure 2-5. Fluorescence microscopy imaging of barcode complex conjugated beads in a CCFB approach. (a) Schematic illustration of the preparation of barcode complex conjugated beads, in which biotin-modified F strand oligomer (F4) immobilized to streptavidin-coated polystyrene beads. (b) Schematic illustration of decoding procedure in which Q strands were sequentially added to barcoded beads. (c) Fluorescent colors on the beads barcoded in the order of Cy5→Cy3→FAM were changed by adding Q strands. Fluorescent images were acquired before and 30 min after the addition of indicated Q strands (Q1, 30 pmol; Q2, 60 pmol; Q3, 90 pmol) in PBS at room temperature in order from top to bottom Cy5, Cy3, FAM channel, and merged images. Scale bars = 20 μ m. (d, e) Merged fluorescence images of beads barcoded in the order of (d) Cy3→Cy5→FAM and (e) FAM→Cy5→Cy3. Scale bars = 20 μ m. (f) Fluorescence intensities of each bead in panels c (left), d (middle), and e (right) were normalized for each bead to the intensity of the first dye at the initial state. Data are mean \pm SD.

(Figure 2-5b). Before the addition of Q strands, only Cy5 emission was observed (Figure 2-5c). The addition of Q1 allowed to quench of Cy5 emissions and emit Cy3 fluorescence, and the addition of Q3 allowed to quench of Cy3 and emit FAM. Similarly, fluorescence color changes in the desired order of Cy3→Cy5→FAM and FAM→Cy5→Cy3 were observed (Figure 2-5d, e). Quantitative fluorescence analysis of each bead also showed that fluorescent barcodes worked on the beads (Figure 2-5f). Kinetics of the strand displacement reaction on beads after adding Q strands indicated that fluorescence changes were almost completed within 3 min (Figure S2-9). The quenching efficiency of the barcode complex on the beads seems to be a little lower than that in the solution (Figure 2-5b). This difference between the beads and the solution might be caused by incomplete hybridization, electrostatic interaction, and steric effects on beads. Notably, efficient strand displacement reaction can occur even when the barcode complex was immobilized on beads.

Next, to confirm the multiplexed detection ability of the CCFB method, we performed simultaneous detections of nine different barcode-conjugated beads (Figure 2-6). Fluorescence color changes of a mixture of beads conjugated with any one of nine different barcodes were observed upon the addition of Q strands (Figure 2-6a, b). All barcode complexes have the same base sequence oligomers, thus the completion of strand displacement reaction of the barcode even with no color change (e.g., barcode 1: Cy5→Cy5→Cy5) can be judged because the other barcode changed its fluorescence. Representative example of nine different fluorescence color changes in Figure 2-6c were obtained from the results in Figure 2-6b. We can decode the nine different barcodes by monitoring color changes as shown in Figure 2-6c and unambiguously assign all nine barcodes (Figure 2-6d). Quantitative analyses of the nine different barcoded beads supported the discrimination of barcodes (Figure S2-10). From these results, we concluded that the CCFB methodology can be used to detect multiplexed targets simultaneously. Notably, multiple targets can be detected by CCFB, although we employed only three fluorophores. Moreover, only three Q strands were used, no washing operations were required, and all operations are in about 1.5 h in total. Therefore, the CCFB approach allows more rapid multiple imaging with a simpler protocol than conventional multiplexed fluorescence methods.

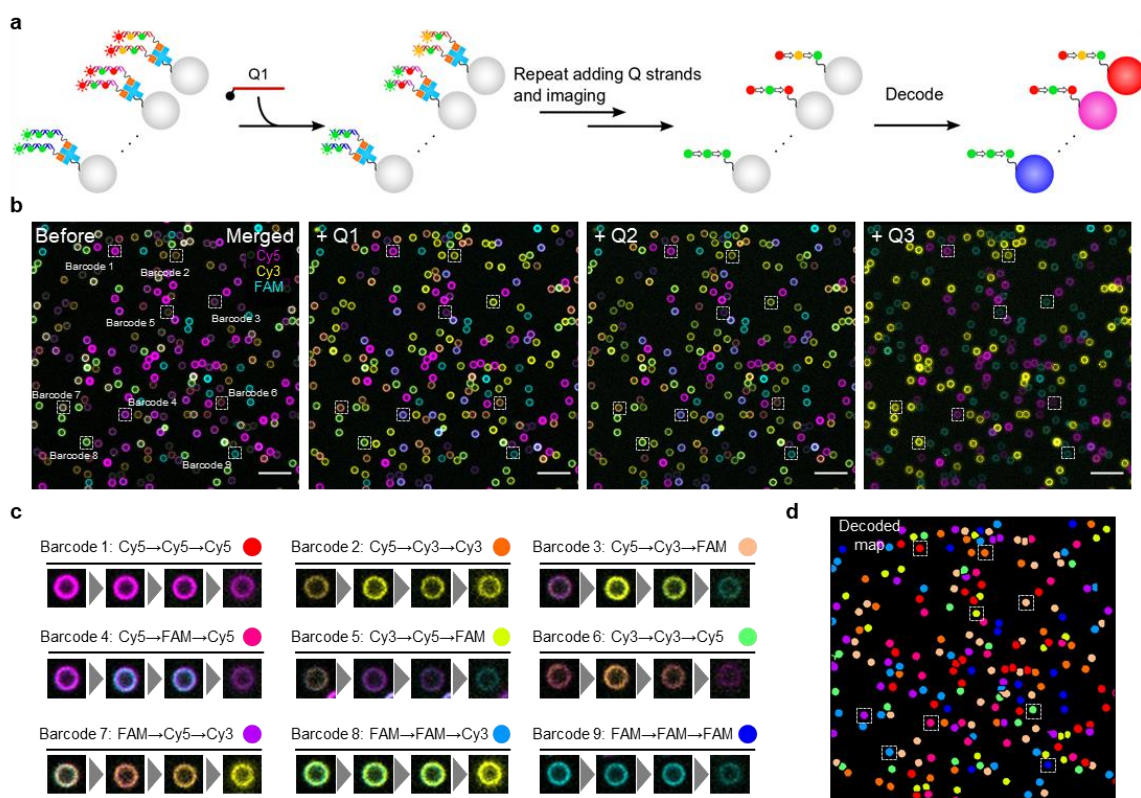


Figure 2-6. Multiplexed labeling of beads with nine different fluorescent barcodes. (a) Schematic illustration of a scheme to decode the multiple barcode complex conjugated beads at the same time. (b) Merged fluorescent images of nine different barcodes conjugated beads before and after the addition of Q strands (Cy5, magenta; Cy3, yellow; FAM, cyan). Scale bars = 20 μm . (c) Representative fluorescence color changes of nine different barcode beads in the highlighted areas from panel b. (d) Decoded map based on fluorescence color changes as shown in panels b and c. Each barcode was assigned with colors as designed in panel c.

2-4-3. *In situ* Protein imaging with CCFB

Next, we applied CCFB to label proteins in cells to demonstrate the capability of biomolecule imaging. We first used phalloidin³⁴ which is a bicyclic peptide that binds to F-actin specifically as proof of concept. Thiol-modified D-*a*TNA oligomer was conjugated to amino-modified phalloidin by using heterobifunctional cross-linker succinimidyl-[(N-maleimidopropionamido)-diethylene glycol] ester (SM(PEG)₂) (Figure 2-7a). Oligonucleotide-conjugated phalloidin was purified with RP-HPLC and was characterized by MALDI-TOF mass spectrometry (Figure S2-11). Subsequently, oligonucleotide-conjugated phalloidin hybridized with appropriate D-*a*TNA

oligomers for Cy5→Cy3→FAM barcode to obtain phalloidin-barcode conjugates. F-actin in the paraformaldehyde-fixed HeLa cells was stained by conjugates and then repetitive adding of Q strands changed fluorescence colors on the stained targets (Figure 2-7b). Fluorescence images were acquired before and 30 min after each addition of indicated Q strands (Figure 2-7c and Figure S2-12). As a result, the fluorescence colors were changed at a filamentous structure in the intended order of Cy5→Cy3→FAM (Figure 2-7c). The fluorescence intensity profile on the line in Figure 2-7c also showed the color changes stained by phalloidin barcode conjugates (Figure 2-7d). Therefore, we successfully labeled proteins in cells by a CCFB method.

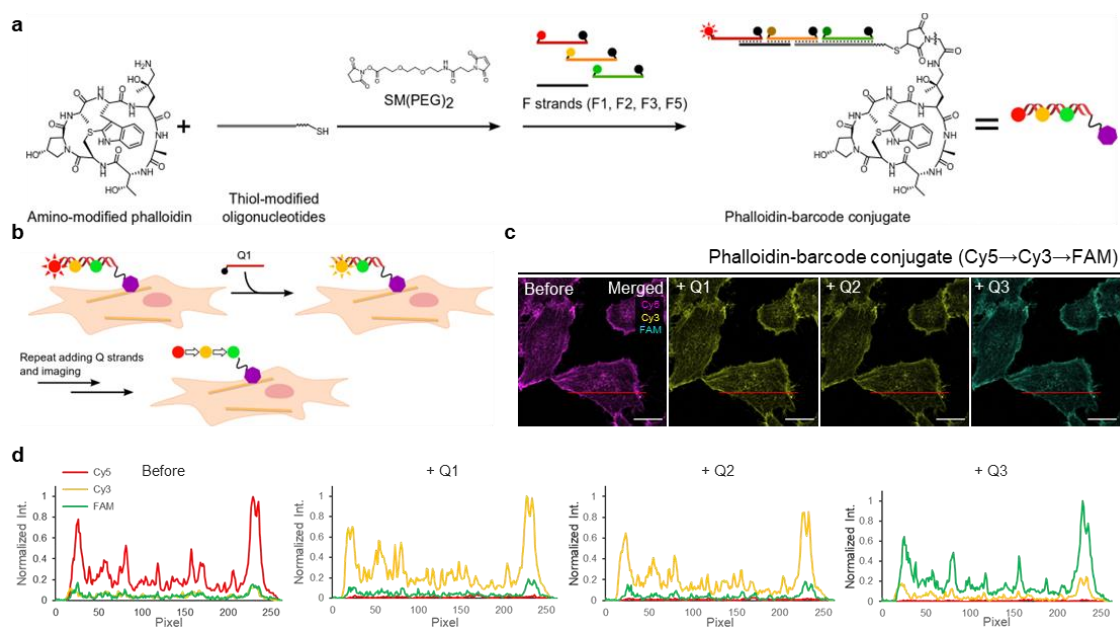


Figure 2-7. F-actin imaging utilizing phalloidin-barcode conjugate with the CCFM method. (a) Synthetic scheme for preparing the phalloidin-barcode conjugate by crosslinking between amino-modified phalloidin and thiol-modified oligomer. (b) Schematic illustration of CCFB imaging consisting of phalloidin staining and Q strands addition. Fixed HeLa cells were incubated with 200 nM phalloidin-barcode conjugate for 30 min, and then Q strands (Q1, 30 pmol; Q2, 60 pmol; Q3, 90 pmol) were added to change fluorescence color. (c) Fluorescent images of the barcode of Cy5→Cy3→FAM were obtained before and after Q strands addition. (Cy5, magenta; Cy3, yellow; FAM, cyan). Scale bars = 20 μm. (d) Line intensity profiles of red lines in panel c. Fluorescence intensities were normalized to the maximum intensity.

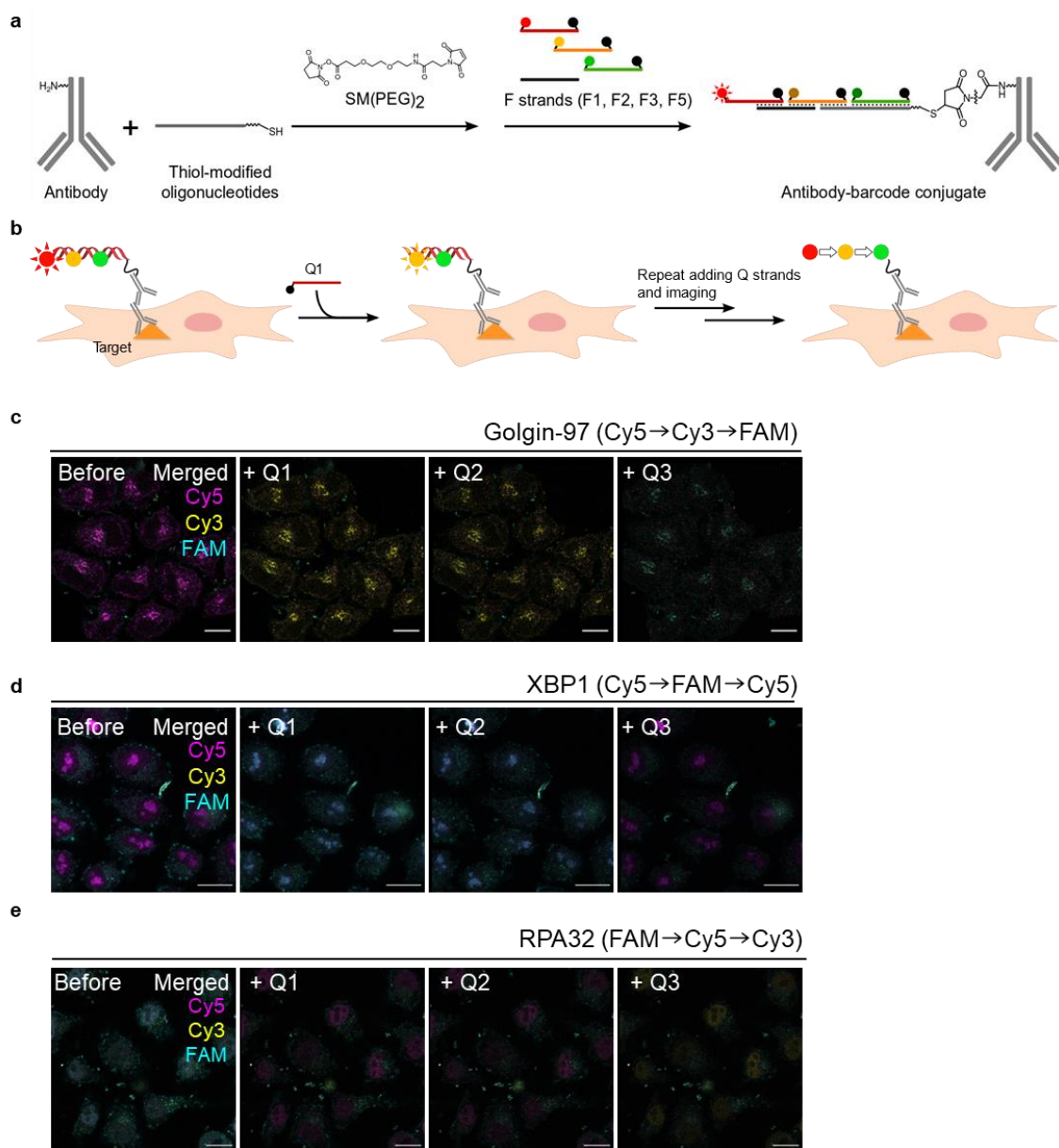


Figure 2-8. CCFB imaging with antibody-barcode conjugate enables imaging of proteins in cells. (a) Synthetic scheme for antibody-barcode conjugates. (b) Schematic illustration of immunostaining by antibody-barcode conjugates and repeat Q strands addition. Fixed HeLa cells were immunostained with standard primary antibody and then with barcode-conjugated secondary antibody. Fluorescent images were acquired each adding Q strands (Q1, 30 pmol; Q2, 60 pmol; Q3, 90 pmol). (c-e) Fluorescent images with CCFB system for (c) Golgin-97 (Cy5 \rightarrow Cy3 \rightarrow FAM), (d) XBP1 (Cy5 \rightarrow FAM \rightarrow Cy5), and (e) RPA32 (FAM \rightarrow Cy5 \rightarrow Cy3).

Moreover, we applied the CCFB method to immunostaining using an antibody to label various proteins generally (Figure 2-8). Thiol-modified D-*a*TNA oligomers were coupled to amino groups of an antibody via a method like that of phalloidin conjugation. We here used secondary antibodies as a proof-of-concept in this experiment, whereas primary antibodies can be also used. The conjugation between thiol-modified oligomers and antibodies and the formation of barcode complex on antibodies were confirmed via SDS-PAGE (Figure S2-13). Appropriate D-*a*TNA oligomers forming the barcode complex with Cy5→Cy3→FAM were hybridized to oligomers conjugated antibodies (Figure 2-8a). To verify the capability of protein imaging with antibodies in the CCFB system, we first selected Golgin-97 as a target protein localized in the Golgi apparatus. Fixed-HeLa cells were immunostained by the prepared anti-mouse secondary antibody-barcode conjugates. Subsequently, we repeated adding Q strands and imaging (Figure 2-8b). As a result, the fluorescence changes were observed in the Golgi apparatus in the intended order (Figure 2-8c and Figure S2-14a). To demonstrate the generality of protein imaging, we also visualized other proteins in organelles by a CCFB method. When XBP1 was stained by using anti-rabbit secondary antibodies conjugated with a barcode of Cy5→FAM→Cy5, fluorescence change was observed at nucleoli in the intended order (Figure 2-8d and Figure S2-14b). Similarly, RPA32 which localized in the nucleus was observed by using an anti-rat antibody with barcode FAM→Cy5→Cy3 (Figure 2-8e and Figure S2-14c). The fluorescence imaging results of proteins present in each of these organelles were consistent with those of standard immunofluorescence assays using dye-conjugated secondary antibodies (Figure S2-14d). These experiments confirmed that a CCFB method successfully detects target proteins and demonstrated that the barcode complex conjugated antibodies can bind to targets with no binding interference.

Finally, we tried multiple protein imaging with antibody-barcode conjugates used above. Fixed-HeLa cells were immunostained by the three conjugates which have different fluorescence color barcodes simultaneously, and then we repeated adding Q strand and acquired images (Figure 2-9a). As a result, different fluorescence color changes were observed in each organelle; Cy5→Cy3→FAM in Golgin-97, Cy5→FAM→Cy5 in XBP1, and FAM→Cy5→Cy3 in RPA32 (Figure 2-9b and Figure S2-15). The same color-changing pattern between single and multiplexed imaging supported the target-specific detection (compare Figure 2-9b with Figure 2-8c-e).

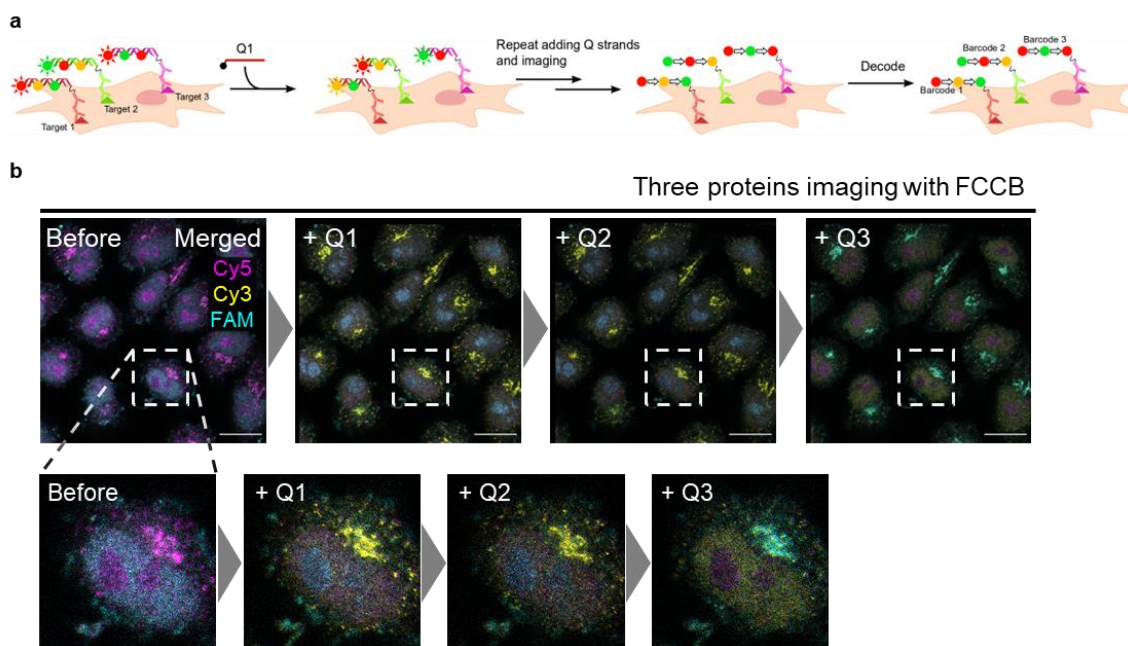


Figure 2-9. CCFB multiple protein imaging with three antibody-barcode conjugates. (a) Schematic illustration of immunostaining by antibody-barcode conjugates and repeat Q strands addition. Fixed HeLa cells were immunostained with barcode-conjugated secondary antibodies simultaneously. Fluorescent images were acquired each adding Q strands (Q1, 30 pmol; Q2, 60 pmol; Q3, 90 pmol). (b) Fluorescent images with CCFB system for detection of Golgin-97 (Cy5→Cy3→FAM), XBP1 (Cy5→FAM→Cy5), and RPA32 (FAM→Cy5→Cy3). Scale bars = 20 μ m.

We also demonstrated that a CCFB method enables to detect four target proteins using three antibody-barcode conjugates and one phalloidin-barcode conjugate (Figure 2-10 and Figure S2-16). As a result, four different fluorescence color changes were observed correctly in each organelle: Cy5→Cy3→FAM in Golgin-97, Cy5→FAM→Cy5 in XBP1, FAM→Cy5→Cy3 in RPA32, and Cy3→Cy5→FAM in F-actin. Therefore, a CCFB method identified four proteins even with only three fluorophores. We believe that the CCFB method can detect more than 5 proteins. Although secondary antibodies were used as a proof-of-concept in this experiment, it limited the number of detectable targets due to the crosstalk among secondary antibodies. In contrast, if we use primary antibody-barcode conjugates, there are no limitations of animal species, which means CCFB is possible to detect a large number of target molecules in cells to overcome the limitation of the number of detectable molecules in the fluorescence method.

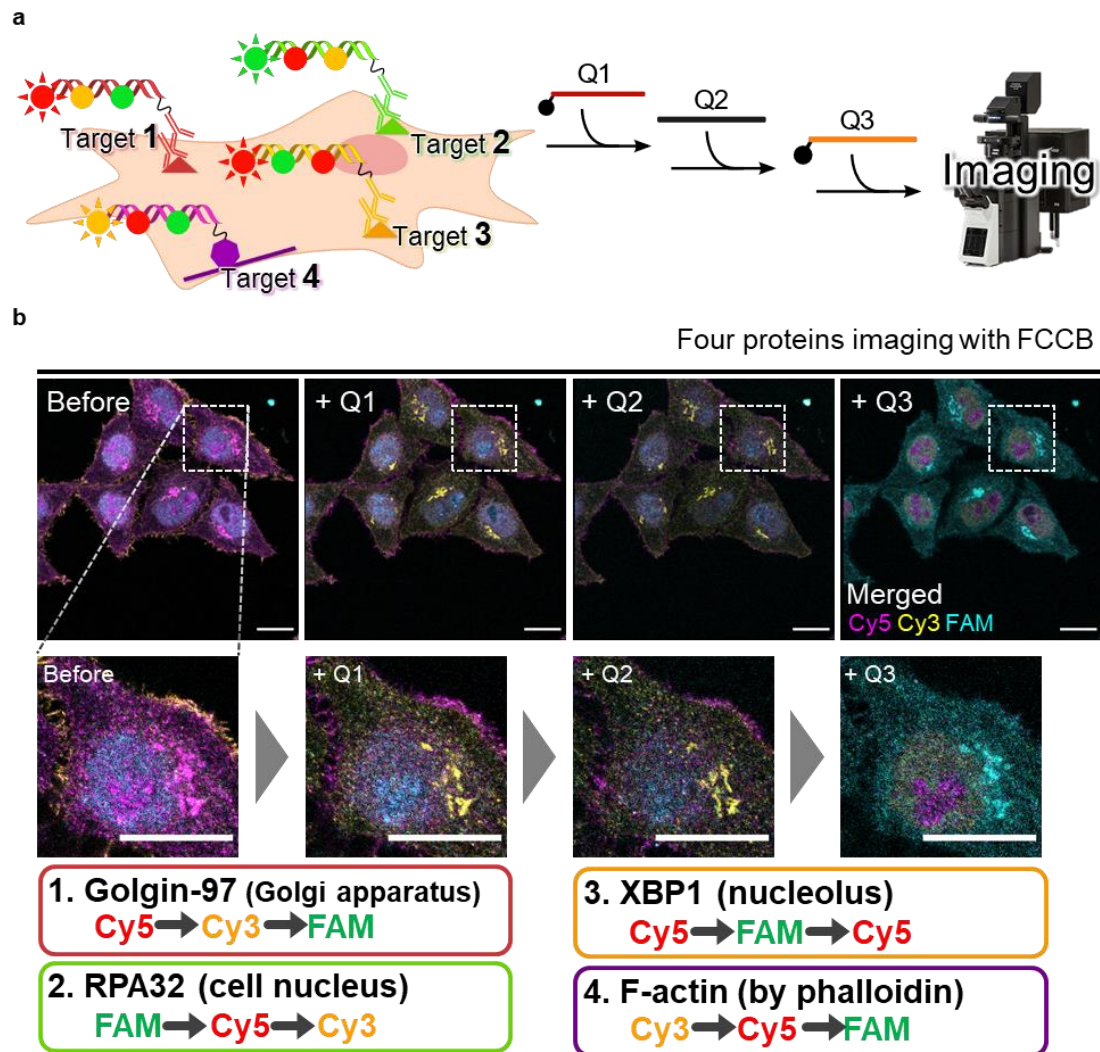


Figure 2-10. CCFB multiple protein imaging with three antibody-barcode conjugates and phalloidin-barcode conjugates. (a) Schematic illustration of immunostaining by four conjugates and repeat Q strands addition. Fixed HeLa cells were immunostained with barcode-conjugated secondary antibodies and phalloidin-barcode conjugate simultaneously. Fluorescent images were acquired each adding Q strands (Q1, 30 pmol; Q2, 60 pmol; Q3, 90 pmol). (b) Fluorescent images with CCFB system for detection of Golgin-97 (Cy5→Cy3→FAM), XBP1 (Cy5→FAM→Cy5), RPA32 (FAM→Cy5→Cy3), and F-actin (Cy3→Cy5→FAM). Fluorescent changes by staining with phalloidin-barcode conjugate were observed mainly in the cell membrane. Scale bars = 20 μ m.

2-4-4. The design for sequential fluorescence color changes with CCFB

As described above, we have developed the CCFB method in which the addition of Q strands three times causes a strand displacement reaction at each exposed toehold of the barcode complex, resulting in fluorescence color changes (Figure 2-11a). To simplify this operation, we newly devised the CCFB method, in which one step addition of three Q strands induces sequential time-course fluorescence color changes (Figure 2-11b). This cascade system is realized by the sequential appearances of exposed toeholds as reaction points as the reaction proceeds.

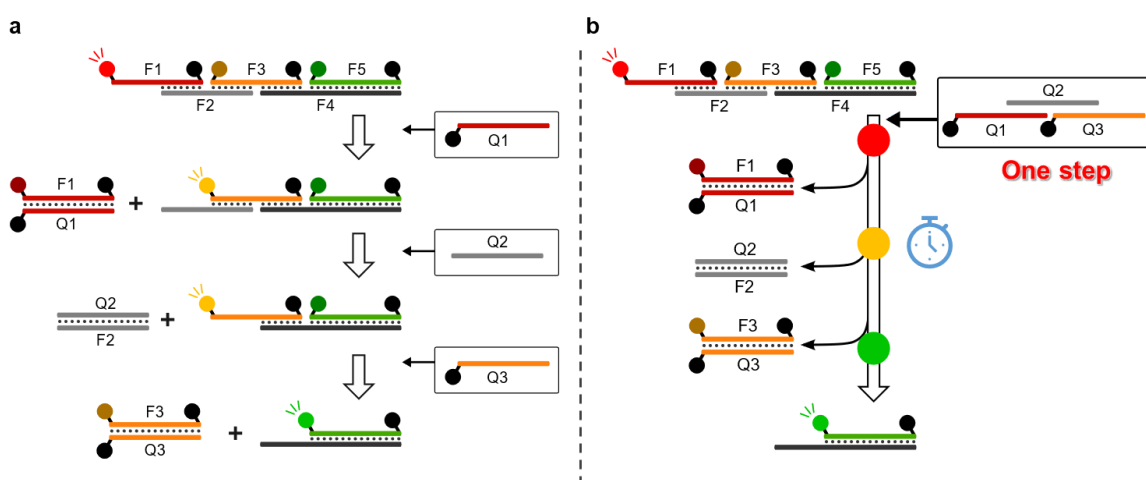


Figure 2-11. Schematic illustrations of two types of CCFB systems. (a) Fluorescence colors can be changed after every three additions of Q strands. (b) Fluorescence colors can be sequentially changed over time after the addition of three Q strands at once.

We first employed the 7-mer D-*a*TNA design used in the previous chapters. The mixed three types of Q strands (Q1, Q2, and Q3) solution was added to the barcode complex of Cy5→Cy3→FAM, subsequently, the quenching of Cy5 was observed. However, other fluorescence changes such as the fluorescence emission of Cy3 and FAM were not observed (Figure S2-17a). No fluorescence change suggested that the intended strand displacement reaction was not observed over time. This may be because Q strands also form linear complexes due to the complementary F strands forming linear complexes. The only observation of Cy5 quenching seems to indicate that the Q strand complex hybridized with the F strand barcode complex in the first toehold, and the reaction stopped because the strands between the two complexes could not be replaced (Figure S2-17b).

The expected sequential color changes were not observed, requiring the redesign of Q strands. The two requirements to achieve a sequential color change are a decrease in the stability of the Q strand duplex and minimal inhibition of the strand displacement reaction. From these requirements, we shorten both ends of all 7-mer overlapping Q strands by 1-mer, named short Q strands, sQ1, sQ2, and sQ3 (Figure 2-12a). Short Q strands are only 5-mer complementary to each other, making it unstable to form a duplex (Figure S2-18), whereas the toehold length between F and sQ strands is 6-mer, which would be long enough for strand displacement reaction (Figure S2-19). The mixed three sQ strands solution was added to the barcode complex of Cy5→Cy3→FAM. As a result, the quenching of Cy5 was observed and the fluorescence of Cy3 increased and subsequently decreased, and FAM gradually emitted fluorescence (Figure 2-12b and Figure S2-20). Therefore, the intended time course fluorescence color change was successfully observed.

In summary, the simple redesign of Q strands allowed to construct a sequential fluorescence color change system. CCFB with only one addition of sQ strands will become a very convenient multiplexed imaging technique.

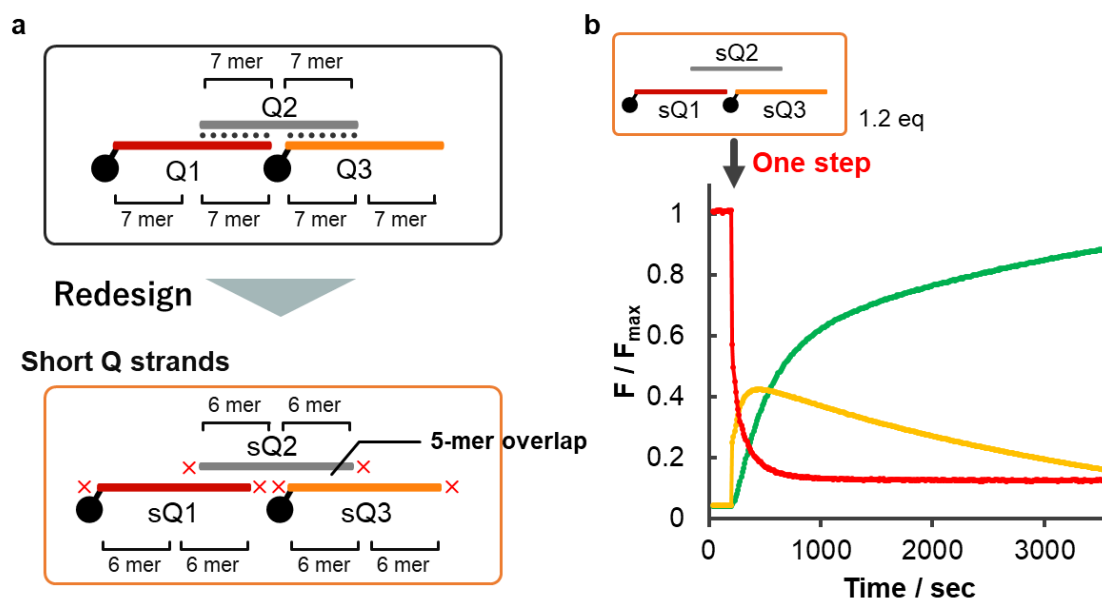


Figure 2-12. (a) The design of a short Q strand. (b) Fluorescence monitoring upon the addition of the mixed three types of short Q strands (sQ1, sQ2, and sQ3) to the barcode complex of Cy5→Cy3→FAM. Fluorescence intensities were normalized by the maximum intensity (F_{\max}) of each fluorophore when Q strands were added one by one. Conditions: 0.2 μM barcode complex, 0.24 μM Q strands, 100 mM NaCl, 10 mM phosphate buffer (pH 7.0), 25°C.

2-5. Conclusion

This report describes the development and validation of a CCFB approach which is a new multiple-labeling method for comprehensive biomolecule imaging. The compactness of this CCFB approach is one of the advantages, which is a total length of 42 bp and less than 30 kDa. In comparison with this, other fluorescent barcoded labeling methods using DNA nanostructure reach more than a megadalton^{15, 27, 29}. One other advantage of this approach is that a preparation of 27 different barcode sets needs only 14 D-*a*TNA oligomers. The high scalability of a CCFB system is also another advantage, the number of barcodes increases exponentially by an extension of the CCFB probe design. For example, $4^4 = 256$ different barcodes in a CCFB system required a design that consists of four fluorophores and changes fluorescence colors three times, whereas only 24 oligomers are sufficient. This simplicity of a CCFB approach dramatically reduces the synthetic cost of probe oligomers. Moreover, when the color changes four times with four fluorophores, $4^5 = 1,024$ molecules are detectable. When the color changes six times, the number of barcodes exceeds more than ten thousand. We also demonstrated that multiple proteins in fixed HeLa cells were detected simultaneously by a few times additions of Q strands to an interested sample on conventional fluorescence microscopy. Notably, no special instruments and no complicated operation such as washing, harsh condition inactivation of fluorophores, and restaining with antibodies are required. These complicated multi-step operations are one of the major issues in conventional multiple protein imaging methodologies. Acyclic artificial nucleic acid D-*a*TNA is used in our CCFB system because this oligomer forms an extremely stable duplex and reduces background fluorescence. In addition, its nuclease resistance and its orthogonality to DNA and RNA make the barcode complex stable even in an intracellular condition.

Furthermore, CCFB has the potential to label biomolecules other than proteins, for example, our method can be used for multiple RNA imaging by using a complementary oligomer to target RNAs. The CCFB system may be available to detect protein-protein and protein-RNA interactions by the introduction of proximity spatial imaging methods³⁵⁻³⁶. Moreover, the unique ability of sequential fluorescence color changes may be applicable to DNA-based technologies such as DNA cryptography³⁷, in which additions of complementary Q strands decode information encrypted with fluorescence color sequences. In summary, this CCFB method is a versatile labeling approach that will be practically useful in biotechnologies and DNA nanotechnologies.

2-6. Experimental section

Preparation of D-*a*TNA oligomers

T, G, A, C, and Dabcyl D-*a*TNA monomers were synthesized according to the reported procedures^{31, 32, 38}. The D-*a*TNA oligomers were synthesized on an automated DNA synthesizer (H-8-SE, Gene World or ABI-3400 DNA synthesizer, Applied Biosystem) by using synthesized phosphoramidite D-*a*TNA monomers and standard reagents. Amino lcaa CPG (Controlled Pore Glass) 500-Å support (ChemGenes) tethering D-*a*TNA monomers was used as a solid support. The coupling efficiency of D-*a*TNA monomers was as high as that of the conventional monomers, as judged by the coloration of the released trityl cation. After the recommended work-up, oligomers were purified by RP-HPLC and were characterized by MALDI-TOFMS (Autoflex, Bruker Daltonics). All D-*a*TNA and DNA oligomers used in this report are listed in Table S2-1 to 3 and Table S2-7).

Fluorescence measurements

The fluorescence measurements were performed on a JASCO model FP-6500. Dried oligomers for barcode complex (F1-F5) were dissolved to each oligomer concentration of 0.2 μM in 100 mM NaCl, 10 mM phosphate buffer (pH 7.0). Sample solutions containing barcode complex in a tube were heated at 80°C for 5 min, then cooled down to 20 °C over about 1 h. Fluorescence at the initial state was measured, and then 0.4 μM Q strands (Q1, Q2, and Q3) were sequentially added at intervals of 10 min. The fluorescence of each fluorophore was recorded at 10 s intervals. Excitation and emission wavelengths were as follows: Cy5: Ex. = 620 nm, Em. = 660 nm; Cy3: Ex. = 530 nm, Em. = 561 nm; FAM: Ex. = 495 nm, Em. = 515 nm.

Preparation of barcode complex conjugated beads

D-*a*TNA F strand oligomers (50 pmol) including biotin-modified oligomers (F4B) were mixed with 10 μ L of 4.0 μ m streptavidin-coated polystyrene beads suspension solution (micromod Partikeltechnologie GmbH, 01-19-403) and incubated overnight at 4 °C. After addition of 200 μ L buffer (100 mM NaCl, 10 mM phosphate buffer, 0.02% NaN₃), the beads suspension was centrifuged for 5 min at 15,000 \times g, and about 200 μ L of the supernatant was removed. This washing procedure was repeated three times. This barcode-conjugated bead was stored at 4 °C.

Fluorescent imaging of barcode-conjugated beads

Biotin-BSA (1.0 mg/mL; Sigma-Aldrich, A8549) in buffer (100 mM NaCl, 10 mM phosphate buffer, 0.02% NaN₃) was incubated in wells of a 96-well glass-bottom plate for 30 min at 4 °C and then washed with 100 μ L of PBS. One or nine barcode-conjugated beads were prepared at about 1.5 μ L of a total 25 mg/mL bead suspension in 100 μ L of PBS. The bead suspension was added to the biotin-BSA incubated plates and incubated for 2 h at 4 °C. After washing twice with 100 μ L of PBS, PBS was added in well. After an initial fluorescence image was acquired, Q strands (Q1: 30 pmol, Q2: 60 pmol, Q3: 90 pmol) in PBS were added sequentially. Samples were incubated for 30 min at room temperature after each Q strand addition prior to image acquisition. Fluorescence images were taken with an FV-3000 confocal laser microscopy (Olympus) using a 60 \times oil immersion objective lens. Barcode-conjugated beads were visualized using the following excitation and emission wavelengths: Cy5: Ex = 640 nm, Em = 650 - 700 nm; Cy3: Ex = 561 nm, Em = 570 - 610 nm; FAM: Ex = 488 nm, Em = 500 - 550 nm. The fluorescent images were processed and analyzed with the FIJI package of ImageJ.

Synthesis of oligonucleotide conjugated phalloidin

Excess maleimide-PEG₂-NHS ester crosslinker (TCI, M3079) and 20 nmol triethylamine (KISHIDA CHEMICAL Co., Ltd.) were added to 4 nmol phalloidin amine (Santa Cruz Biotechnology, sc-397330) in DMF and reacted for 3 h at room temperature. The product was purified by RP-HPLC (Mightysil RP-18GP II column, KANTO CHEMICAL CO., INC.). In

parallel, 6 nmol thiol-modified oligomers (F4S) protected by the disulfide were reduced using 30 μ L of 10 mM TCEP (tris(2-carboxyethyl)phosphine) in 50 mM HEPES buffer with 2 mM EDTA for 2 h at room temperature. The reduced oligomers were purified by RP-HPLC and characterized by MALDI-TOFMS. The maleimide-activated phalloidin was mixed with reduced oligomers in PBS. The reaction proceeded at room temperature overnight, and the resulting product was purified by RP-HPLC, and identity was confirmed by MALDI-TOFMS.

Preparation of oligonucleotide conjugated antibodies

In the case of including sodium azide in the buffer solution for the preservation of antibodies, secondary antibodies were purified using 0.5 mL 50 kDa Amicon Ultra Filter (Merck Millipore, UFC505024). Next, 100 μ g antibody in PBS was reacted with about 7.0 eq maleimide-PEG₂-NHS ester crosslinker (Thermo Scientific, A35397) in DMF for 2 h at 4 °C. Excess crosslinker was removed using Zeba spin columns (7000 MWCO, Thermo Scientific, 89882). In parallel, 6 nmol D-*a*TNA thiol-modified oligomers (F4S) were reduced using 40 μ L of 10 mM TCEP (tris(2-carboxyethyl)phosphine) in 50 mM HEPES buffer with 2 mM EDTA for 2 h at room temperature. The reduced oligonucleotides were purified by RP-HPLC. The maleimide-activated antibodies were incubated with reduced oligonucleotides in PBS overnight at 4 °C. The conjugated antibodies were purified using 0.5 mL 50 kDa Amicon Ultra Filter to remove excess oligomers. Conjugation was verified with SDS-PAGE (Figure S2-10). Barcode-conjugated antibodies were prepared by adding excess F strands.

Cell culture

HeLa cells were cultured in a Dulbecco's Modified Eagle Medium (DMEM) supplemented with 10% fetal bovine serum, 80 μ g/mL penicillin, and 90 μ g/mL streptomycin. The cells were cultured with 5% CO₂ in humidified air at 37 °C.

Fluorescent imaging using phalloidin-barcode conjugate

HeLa cells (100 μ L of 70,000 cells/mL) were added to wells of a 96-well glass-bottom plate and cultured overnight, then fixed with 4% paraformaldehyde (PFA) phosphate buffer solution (FUJIFILM Wako Pure Chemical Corporation) for 10 min at room temperature and washed with PBS. Cells were permeabilized with 0.5 % Triton-X100 in PBS for 5 min at room temperature. Cells were then blocked with 1% BSA in PBS for 1 h at room temperature and washed with PBS. Next, 200 nM phalloidin-barcode conjugates in PBS were incubated for 30 min at room temperature in the dark and then washed with PBS. Images were acquired at the initial state in PBS. Subsequently, 30 pmol Q1 in PBS was added and incubated for 30 min at room temperature on the microscope stage, and another image was taken. These steps were repeated with 60 pmol Q2 and then 90 pmol Q3. The stained HeLa cells were visualized using an FV-3000 confocal laser microscope (Olympus) using a 60 \times oil immersion objective lens. The fluorescent signals were recorded using the following excitation and emission wavelengths: Cy5: Ex. = 640 nm, Em. = 650 - 750 nm; Cy3: Ex. = 514 nm, Em. = 565 - 630 nm; FAM: Ex. = 488 nm, Em. = 500 - 540 nm.

Fluorescent immunostaining with barcode-conjugated secondary antibodies

HeLa cells (100 μ L of 70,000 cells/mL) were added to each well of a 96-well glass-bottom plate and cultured overnight. HeLa cells were fixed with 4% PFA phosphate buffer solution for 10 min at room temperature and washed with PBS. Cells were permeabilized with 0.1 % Triton-X100 in PBS for 5 min at room temperature. Cells were then blocked with 2% BSA with 0.1% Triton-X100 in PBS for 1 h at room temperature. The sample was incubated with the primary antibodies diluted at an appropriate concentration in 2% BSA with 0.1% Triton-X100 in PBS overnight at 4 $^{\circ}$ C and washed with 0.1% Triton-X100 and 2% BSA in PBS twice. Barcode-conjugated secondary antibodies diluted in antibody blocking buffer (0.1% Triton-X100, 2% BSA, 0.2 mg/mL deoxyribonucleic acid sodium salt, 4 mM EDTA, 0.1% dextran sulfate in PBS) were incubated at room temperature or 4 $^{\circ}$ C (for three protein imaging) for 1 h. Samples were washed and post-fixed using 1% PFA in PBS for 10 min at room temperature and then washed with PBS. An image was acquired at the initial state in PBS. Subsequently, 30 pmol Q1 in PBS was added and an image was taken after incubation for 10 or 30 min at room temperature on the microscope stage. These steps were repeated with 60 pmol Q2 and 90 pmol Q3. The stained HeLa cells were

visualized using an FV-3000 confocal laser microscope (Olympus) using a 60× oil immersion objective lens. The fluorescent signals were recorded using the following excitation and emission wavelengths: Cy5: Ex. = 640 nm, Em. = 650 - 750 nm; Cy3: Ex. = 514 nm, Em. = 565 - 630 nm; FAM: Ex. = 488 nm, Em. = 500 - 540 nm.

Fluorescent immunostaining with barcode-conjugated secondary antibodies and phalloidin

HeLa cells (100 μ L of 70,000 cells/mL) were added to each well of a 96-well glass-bottom plate and cultured overnight. HeLa cells were fixed with 4% PFA phosphate buffer solution for 10 min at room temperature and washed with PBS. Cells were permeabilized with 0.1 % Triton-X100 in PBS for 5 min at room temperature. Cells were then blocked with 2% BSA with 0.1% Triton-X100 in PBS for 1 h at room temperature. The sample was incubated with the primary antibodies diluted at an appropriate concentration in 2% BSA with 0.1% Triton-X100 in PBS overnight at 4 °C and washed with 0.1% Triton-X100 and 2% BSA in PBS twice. Barcode-conjugated secondary antibodies diluted in antibody blocking buffer (0.1% Triton-X100, 2% BSA, 0.2 mg/mL deoxyribonucleic acid sodium salt, 4 mM EDTA, 0.1% dextran sulfate in PBS) were incubated at 4 °C for 1 h in the dark. Samples were washed and post-fixed using 1% PFA in PBS for 10 min at room temperature and then washed with PBS twice. Next, 10 nM phalloidin-barcode conjugate in antibody blocking buffer was incubated for 45 min at 4 °C in the dark and then washed with PBS. An image was acquired at the initial state in PBS. Subsequently, 30 pmol Q1 in PBS was added and an image was taken after incubation for 20 min at room temperature on the microscope stage. These steps were repeated with 60 pmol Q2 and 90 pmol Q3. The stained HeLa cells were visualized using an FV-3000 confocal laser microscope (Olympus) using a 60× oil immersion objective lens. The fluorescent signals were recorded using the following excitation and emission wavelengths: Cy5: Ex. = 640 nm, Em. = 650 - 750 nm; Cy3: Ex. = 561 nm, Em. = 565 - 630 nm; FAM: Ex. = 488 nm, Em. = 500 - 540 nm.

2-7. Reference

1. Hu, F.; Zeng, C.; Long, R.; Miao, Y.; Wei, L.; Xu, Q.; Min, W., Supermultiplexed optical imaging and barcoding with engineered polyynes. *Nat. Methods* **2018**, *15* (3), 194-200.
2. Wei, L.; Chen, Z.; Shi, L.; Long, R.; Anzalone, A. V.; Zhang, L.; Hu, F.; Yuste, R.; Cornish, V. W.; Min, W., Super-multiplex vibrational imaging. *Nature* **2017**, *544* (7651), 465-470.
3. Garini, Y.; Young, I. T.; McNamara, G., Spectral imaging: Principles and applications. *Cytometry Part A* **2006**, *69A* (8), 735-747.
4. Valm, A. M.; Cohen, S.; Legant, W. R.; Melunis, J.; Hershberg, U.; Wait, E.; Cohen, A. R.; Davidson, M. W.; Betzig, E.; Lippincott-Schwartz, J., Applying systems-level spectral imaging and analysis to reveal the organelle interactome. *Nature* **2017**, *546* (7656), 162-167.
5. Wählby, C.; Erlandsson, F.; Bengtsson, E.; Zetterberg, A., Sequential immunofluorescence staining and image analysis for detection of large numbers of antigens in individual cell nuclei. *Cytometry* **2002**, *47* (1), 32-41.
6. Schubert, W.; Bonnekoh, B.; Pommer, A. J.; Philipsen, L.; Böckelmann, R.; Malykh, Y.; Gollnick, H.; Friedenberger, M.; Bode, M.; Dress, A. W. M., Analyzing proteome topology and function by automated multidimensional fluorescence microscopy. *Nat. Biotechnol.* **2006**, *24* (10), 1270-1278.
7. Lin, J.-R.; Fallahi-Sichani, M.; Sorger, P. K., Highly multiplexed imaging of single cells using a high-throughput cyclic immunofluorescence method. *Nat. Commun.* **2015**, *6* (1), 8390.
8. Lin, J.-R.; Izar, B.; Wang, S.; Yapp, C.; Mei, S.; Shah, P. M.; Santagata, S.; Sorger, P. K., Highly multiplexed immunofluorescence imaging of human tissues and tumors using t-CyCIF and conventional optical microscopes. *eLife* **2018**, *7*, e31657.
9. Gerdes, M. J.; Sevinsky, C. J.; Sood, A.; Adak, S.; Bello, M. O.; Bordwell, A.; Can, A.; Corwin, A.; Dinn, S.; Filkins, R. J.; Hollman, D.; Kamath, V.; Kaanumalle, S.; Kenny, K.; Larsen, M.; Lazare, M.; Li, Q.; Lowes, C.; McCulloch, C. C.; McDonough, E.; Montalto, M. C.; Pang, Z.; Rittscher, J.; Santamaria-Pang, A.; Sarachan, B. D.; Seel, M. L.; Seppo, A.; Shaikh, K.; Sui, Y.; Zhang, J.; Ginty, F., Highly multiplexed single-cell analysis of formalin-fixed, paraffin-embedded cancer tissue. *Proc. Natl. Acad. Sci. U. S. A.* **2013**, *110* (29), 11982-7.
10. Ko, J.; Oh, J.; Ahmed, M. S.; Carlson, J. C. T.; Weissleder, R., Ultra-fast Cycling for Multiplexed Cellular Fluorescence Imaging. *Angew. Chem. Int. Ed.* **2020**, *59* (17), 6839-6846.
11. Schweller, R. M.; Zimak, J.; Duose, D. Y.; Qutub, A. A.; Hittelman, W. N.; Diehl, M. R., Multiplexed in situ immunofluorescence using dynamic DNA complexes. *Angew. Chem. Int. Ed. Engl.* **2012**, *51* (37), 9292-6.
12. Duose, D. Y.; Schweller, R. M.; Zimak, J.; Rogers, A. R.; Hittelman, W. N.; Diehl, M. R., Configuring robust DNA strand displacement reactions for in situ molecular analyses. *Nucleic Acids Res.* **2011**, *40* (7), 3289-3298.
13. Giedt, R. J.; Pathania, D.; Carlson, J. C. T.; McFarland, P. J.; del Castillo, A. F.; Juric, D.;

Weissleder, R., Single-cell barcode analysis provides a rapid readout of cellular signaling pathways in clinical specimens. *Nat. Commun.* **2018**, *9* (1), 4550.

14. Jungmann, R.; Steinhauer, C.; Scheible, M.; Kuzyk, A.; Tinnefeld, P.; Simmel, F. C., Single-Molecule Kinetics and Super-Resolution Microscopy by Fluorescence Imaging of Transient Binding on DNA Origami. *Nano Lett.* **2010**, *10* (11), 4756-4761.

15. Lin, C.; Jungmann, R.; Leifer, A. M.; Li, C.; Levner, D.; Church, G. M.; Shih, W. M.; Yin, P., Submicrometre geometrically encoded fluorescent barcodes self-assembled from DNA. *Nat. Chem.* **2012**, *4* (10), 832-839.

16. Jungmann, R.; Avendaño, M. S.; Dai, M.; Woehrstein, J. B.; Agasti, S. S.; Feiger, Z.; Rodal, A.; Yin, P., Quantitative super-resolution imaging with qPAINT. *Nat. Methods* **2016**, *13* (5), 439-442.

17. Dai, M.; Jungmann, R.; Yin, P., Optical imaging of individual biomolecules in densely packed clusters. *Nature Nanotechnology* **2016**, *11* (9), 798-807.

18. Sharonov, A.; Hochstrasser, R. M., Wide-field subdiffraction imaging by accumulated binding of diffusing probes. *Proceedings of the National Academy of Sciences* **2006**, *103* (50), 18911-18916.

19. Wang, Y.; Woehrstein, J. B.; Donoghue, N.; Dai, M.; Avendaño, M. S.; Schackmann, R. C. J.; Zoeller, J. J.; Wang, S. S. H.; Tillberg, P. W.; Park, D.; Lapan, S. W.; Boyden, E. S.; Brugge, J. S.; Kaeser, P. S.; Church, G. M.; Agasti, S. S.; Jungmann, R.; Yin, P., Rapid Sequential in Situ Multiplexing with DNA Exchange Imaging in Neuronal Cells and Tissues. *Nano Lett.* **2017**, *17* (10), 6131-6139.

20. Agasti, S. S.; Wang, Y.; Schueder, F.; Sukumar, A.; Jungmann, R.; Yin, P., DNA-barcoded labeling probes for highly multiplexed Exchange-PAINT imaging. *Chem. Sci.* **2017**, *8* (4), 3080-3091.

21. Saka, S. K.; Wang, Y.; Kishi, J. Y.; Zhu, A.; Zeng, Y.; Xie, W.; Kirli, K.; Yapp, C.; Cicconet, M.; Beliveau, B. J.; Lapan, S. W.; Yin, S.; Lin, M.; Boyden, E. S.; Kaeser, P. S.; Pihan, G.; Church, G. M.; Yin, P., Immuno-SABER enables highly multiplexed and amplified protein imaging in tissues. *Nat. Biotechnol.* **2019**, *37* (9), 1080-1090.

22. Goltsev, Y.; Samusik, N.; Kennedy-Darling, J.; Bhate, S.; Hale, M.; Vazquez, G.; Black, S.; Nolan, G. P., Deep Profiling of Mouse Splenic Architecture with CODEX Multiplexed Imaging. *Cell* **2018**, *174* (4), 968-981.e15.

23. Shah, S.; Lubeck, E.; Zhou, W.; Cai, L., In Situ Transcription Profiling of Single Cells Reveals Spatial Organization of Cells in the Mouse Hippocampus. *Neuron* **2016**, *92* (2), 342-357.

24. Eng, C.-H. L.; Lawson, M.; Zhu, Q.; Dries, R.; Koulina, N.; Takei, Y.; Yun, J.; Cronin, C.; Karp, C.; Yuan, G.-C.; Cai, L., Transcriptome-scale super-resolved imaging in tissues by RNA seqFISH+. *Nature* **2019**, *568* (7751), 235-239.

25. Chen, K. H.; Boettiger, A. N.; Moffitt, J. R.; Wang, S.; Zhuang, X., Spatially resolved, highly multiplexed RNA profiling in single cells. *Science* **2015**, *348* (6233), aaa6090.

26. Li, Y.; Cu, Y. T. H.; Luo, D., Multiplexed detection of pathogen DNA with DNA-based fluorescence nanobarcodes. *Nat. Biotechnol.* **2005**, *23* (7), 885-889.

27. Li, J.; Dai, J.; Jiang, S.; Xie, M.; Zhai, T.; Guo, L.; Cao, S.; Xing, S.; Qu, Z.; Zhao, Y.; Wang, F.; Yang, Y.; Liu, L.; Zuo, X.; Wang, L.; Yan, H.; Fan, C., Encoding quantized fluorescence states with fractal DNA frameworks. *Nat. Commun.* **2020**, *11* (1), 2185.
28. Deng, R.; Zhang, K.; Wang, L.; Ren, X.; Sun, Y.; Li, J., DNA-Sequence-Encoded Rolling Circle Amplicon for Single-Cell RNA Imaging. *Chem* **2018**, *4* (6), 1373-1386.
29. Woehrstein, J. B.; Strauss, M. T.; Ong, L. L.; Wei, B.; Zhang, D. Y.; Jungmann, R.; Yin, P., Sub-100-nm metafluorophores with digitally tunable optical properties self-assembled from DNA. *Science Advances* **2017**, *3* (6), e1602128.
30. Murayama, K.; Kamiya, Y.; Kashida, H.; Asanuma, H., Ultrasensitive Molecular Beacon Designed with Totally Serinol Nucleic Acid (SNA) for Monitoring mRNA in Cells. *ChemBioChem* **2015**, *16* (9), 1298-1301.
31. Asanuma, H.; Toda, T.; Murayama, K.; Liang, X.; Kashida, H., Unexpectedly Stable Artificial Duplex from Flexible Acyclic Threoninol. *J. Am. Chem. Soc.* **2010**, *132* (42), 14702-14703.
32. Makino, K.; Hattori, Y.; Kashida, H.; Asanuma, H., Preparation of Artificial Hexaplex Composed of Non-Natural Nucleic Acid. *Current Protocols* **2021**, *1* (4), e106.
33. Hertel, S.; Spinney, R. E.; Xu, S. Y.; Ouldridge, T. E.; Morris, Richard G.; Lee, Lawrence K., The stability and number of nucleating interactions determine DNA hybridization rates in the absence of secondary structure. *Nucleic Acids Res.* **2022**, *50* (14), 7829-7841.
34. Wulf, E.; Deboben, A.; Bautz, F. A.; Faulstich, H.; Wieland, T., Fluorescent phalloxin, a tool for the visualization of cellular actin. *Proc. Natl. Acad. Sci. U. S. A.* **1979**, *76* (9), 4498-502.
35. Schueder, F.; Lara-Gutiérrez, J.; Haas, D.; Beckwith, K. S.; Yin, P.; Ellenberg, J.; Jungmann, R., Super-Resolution Spatial Proximity Detection with Proximity-PAINT. *Angew. Chem. Int. Ed.* **2021**, *60* (2), 716-720.
36. Söderberg, O.; Gullberg, M.; Jarvius, M.; Ridderstråle, K.; Leuchowius, K.-J.; Jarvius, J.; Wester, K.; Hydbring, P.; Bahram, F.; Larsson, L.-G.; Landegren, U., Direct observation of individual endogenous protein complexes in situ by proximity ligation. *Nat. Methods* **2006**, *3* (12), 995-1000.
37. Zhang, Y.; Wang, F.; Chao, J.; Xie, M.; Liu, H.; Pan, M.; Kopperger, E.; Liu, X.; Li, Q.; Shi, J.; Wang, L.; Hu, J.; Wang, L.; Simmel, F. C.; Fan, C., DNA origami cryptography for secure communication. *Nat. Commun.* **2019**, *10* (1), 5469.
38. Asanuma, H.; Shirasuka, K.; Takarada, T.; Kashida, H.; Komiyama, M., DNA-Dye Conjugates for Controllable H* Aggregation. *J. Am. Chem. Soc.* **2003**, *125* (8), 2217-2223.

2-8. Appendixes

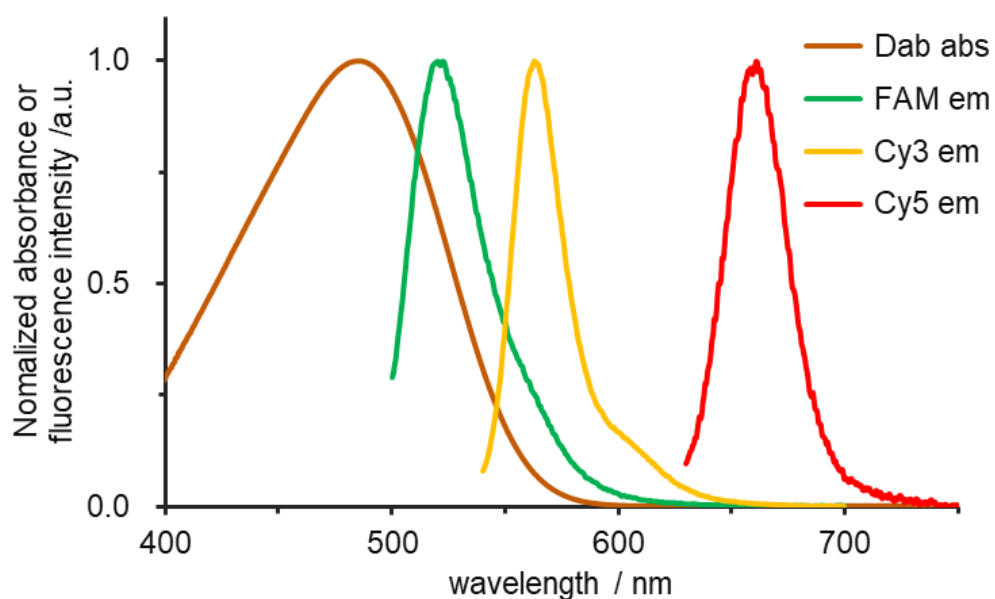


Figure S2-1. Normalized absorbance or fluorescence spectra of three fluorophores; FAM, Cy3, and Cy5, and a quencher Dabcyl. The emission spectra were obtained from the duplex of F4 and FAMF5, Cy3F5, or Cy5F5. Förster radii of FAM-dabcyl, Cy3-dabcyl were calculated as 5 and 2.8 nm, respectively. Energy transfer from Cy5 to dabcyl seems not to occur since there are almost no spectral overlap between Cy5 emission and dabcyl absorption. Conditions: 0.2 μ M oligomers, 100 mM NaCl, 10 mM phosphate buffer (pH 7.0), 20°C. Ex. wavelengths were 495 nm, 530 nm, and 620 nm, respectively.

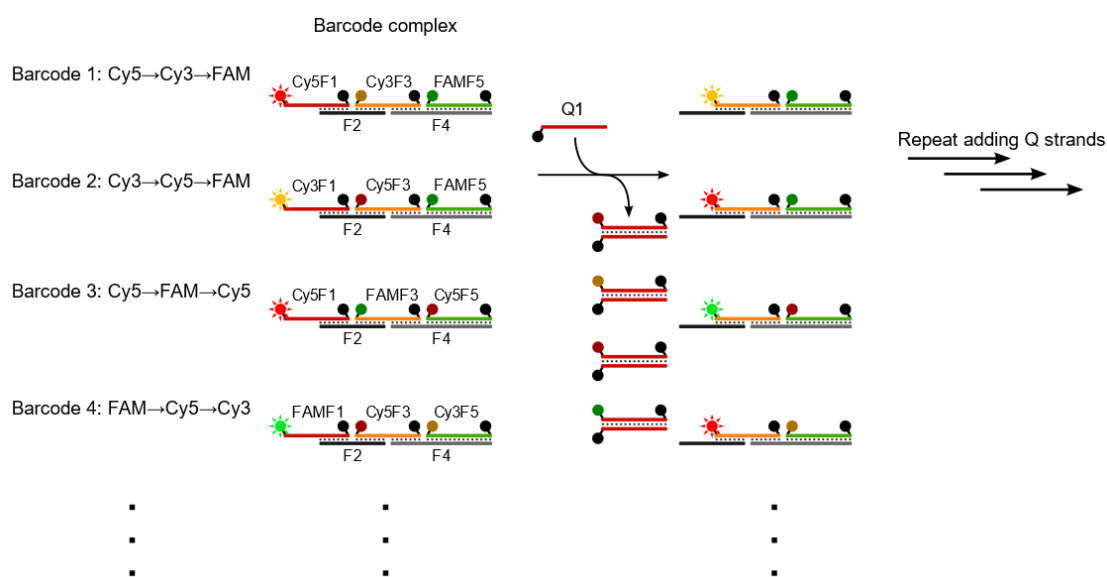


Figure S2-2. The Simple sequence design of CCFB makes preparation and operation easy. Three types of fluorophores; Cy5, Cy3, or FAM are introduced to oligomers with the same base sequence as shown in Table S2-1. For example, Cy5F1, Cy3F3, and FAMF5 were used to prepare the barcode Cy5→Cy3→FAM, and Cy3F1, Cy5F3, and FAMF5 were used to prepare barcode Cy3→Cy5→FAM. In other words, Cy5F1 and Cy3F3 have the same base sequence, but different fluorophores. Therefore, the same Q1 can react to displace F1 strands in all barcode complexes. Moreover, fluorophores on removed oligomers by Q strands are quenched, thus requiring no washing operation.

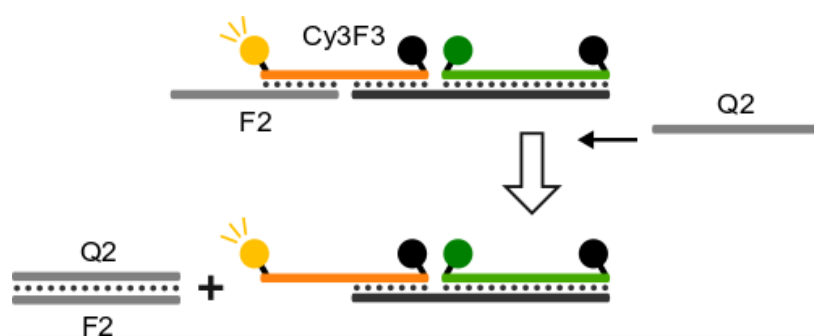


Figure S2-3. Schematic illustration of the Cy3 emission change upon the addition of Q2. Cy3 was located at the end of the duplex before adding Q2. In contrast, Cy3 is located at the end of a single strand after adding Q2. Therefore, Cy3 can become easier to approach an intramolecular quencher because the flexibility of the Cy3F3 strand is increased. That is why Cy3 emission is slightly quenched.

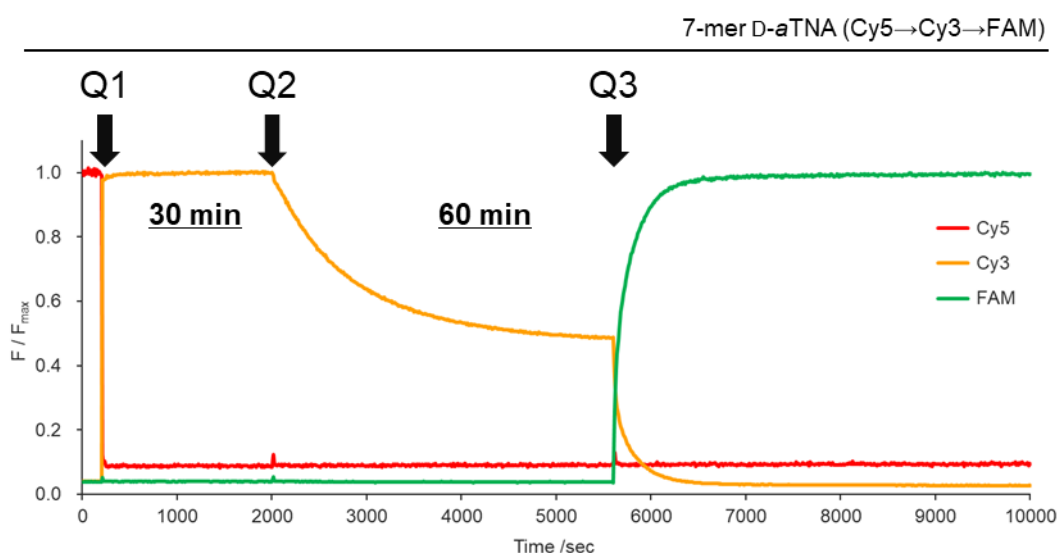


Figure S2-4. No fluorescence changes were observed when Q2 (left) or Q3 (right) was added without Q1 to the 7-mer D-aTNA CCFB with the barcode of Cy5→Cy3→FAM. Conditions: 0.2 μM barcode complex, 0.4 μM Q strand, 100 mM NaCl, 10 mM phosphate buffer (pH 7.0), 20 $^{\circ}\text{C}$. The reaction rates were estimated in the order of Q1 > Q2 > Q3 addition. The first toehold of the 7-mer F1 strand is 1'-CACAGCA-3' which has three "CA" repeat. The second toehold of the F2 strand is 3'-TAGCGGT-1' which has no repeat base sequence. The third toehold of the F3 strand is 1'-AGGCTCT-3' which has two "CT" repeat. In other words, the number of repeat base sequences is in the order of first > third > second toehold, thus the number of repeat base sequences may be related to the reaction rate, which is consistent with the study about DNA hybridization³³. Although this study is for DNA, it may apply to D-aTNA as well.

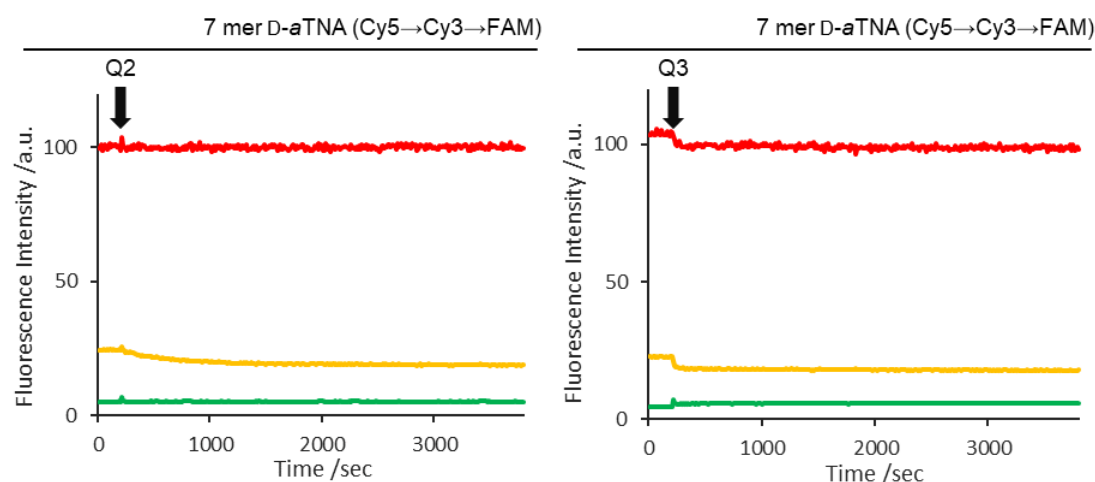


Figure S2-5. No fluorescence changes were observed when Q2 (left) or Q3 (right) was added without Q1 to the 7-mer D-aTNA CCFB with the barcode of Cy5→Cy3→FAM. Conditions: 0.2 μM barcode complex, 0.4 μM Q strand, 100 mM NaCl, 10 mM phosphate buffer (pH 7.0) 20 °C.

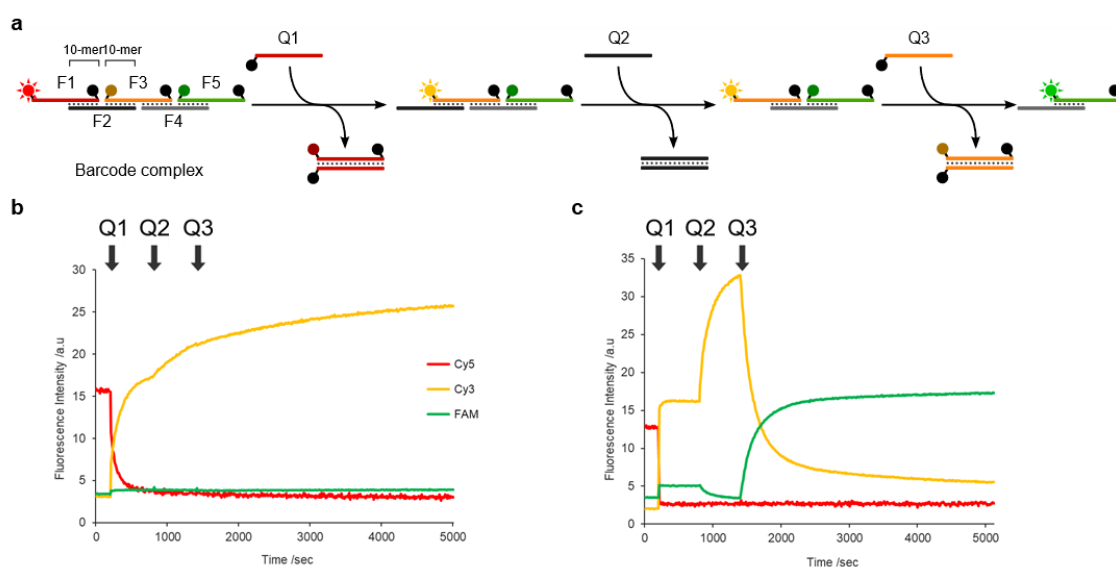
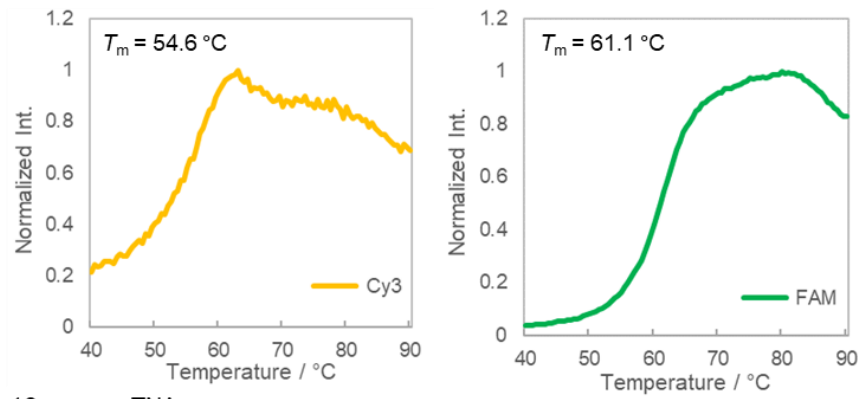
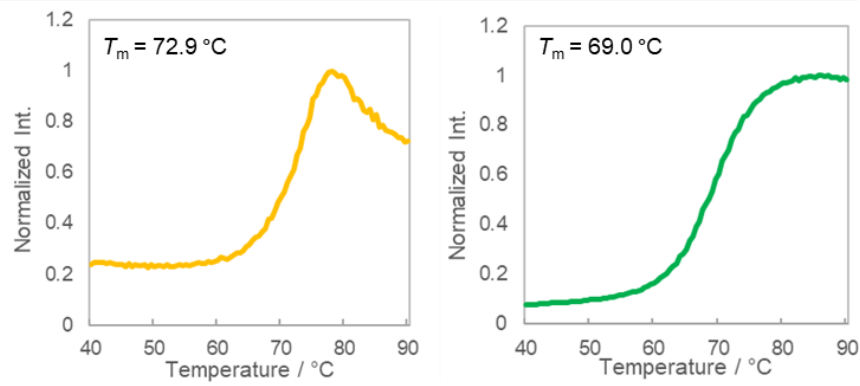


Figure S2-6. (a) Schematic illustration of a CCFB method with 10-mer overlapping D-aTNA design. (b, c) The fluorescence color changes upon the addition of Q1, Q2, and Q3 were observed in the order of Cy5→Cy3→FAM at (b) 20 °C and (c) 40 °C. Q strands were added at the time points indicated by arrows. Conditions: 0.2 μM barcode complex, 0.4 μM Q strands, 100 mM NaCl, 10 mM phosphate buffer (pH 7.0). We also checked the repeat base sequence in this 10-mer design. The first toehold of F1 is 1'-TTCAGCCGCA-3' which has two "CA" repeat and two "GC" repeat. The second toehold of F2 is 3'-TAGGAGCGGA-1' which has two "GGA" repeat. The third toehold of F3 is 1'-TCAGAGCTGG-3' which has two "AG" repeat. The reaction upon the addition of Q1 is faster than Q2 and Q3 could be related to the number of repeat base sequences.

a 7-mer D-aTNA



b 10-mer D-aTNA



c 10-mer DNA

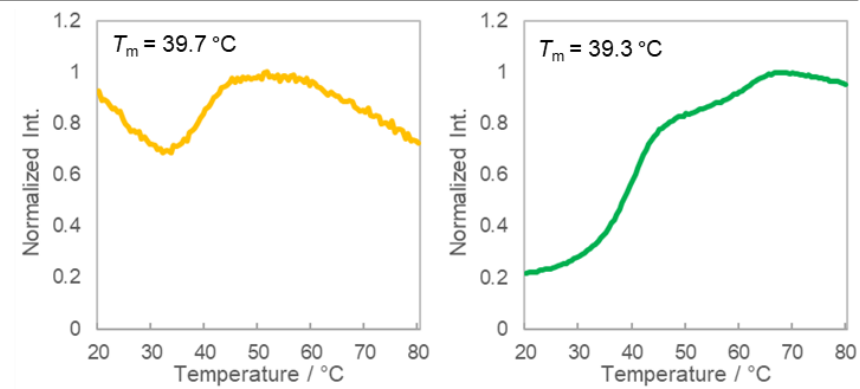
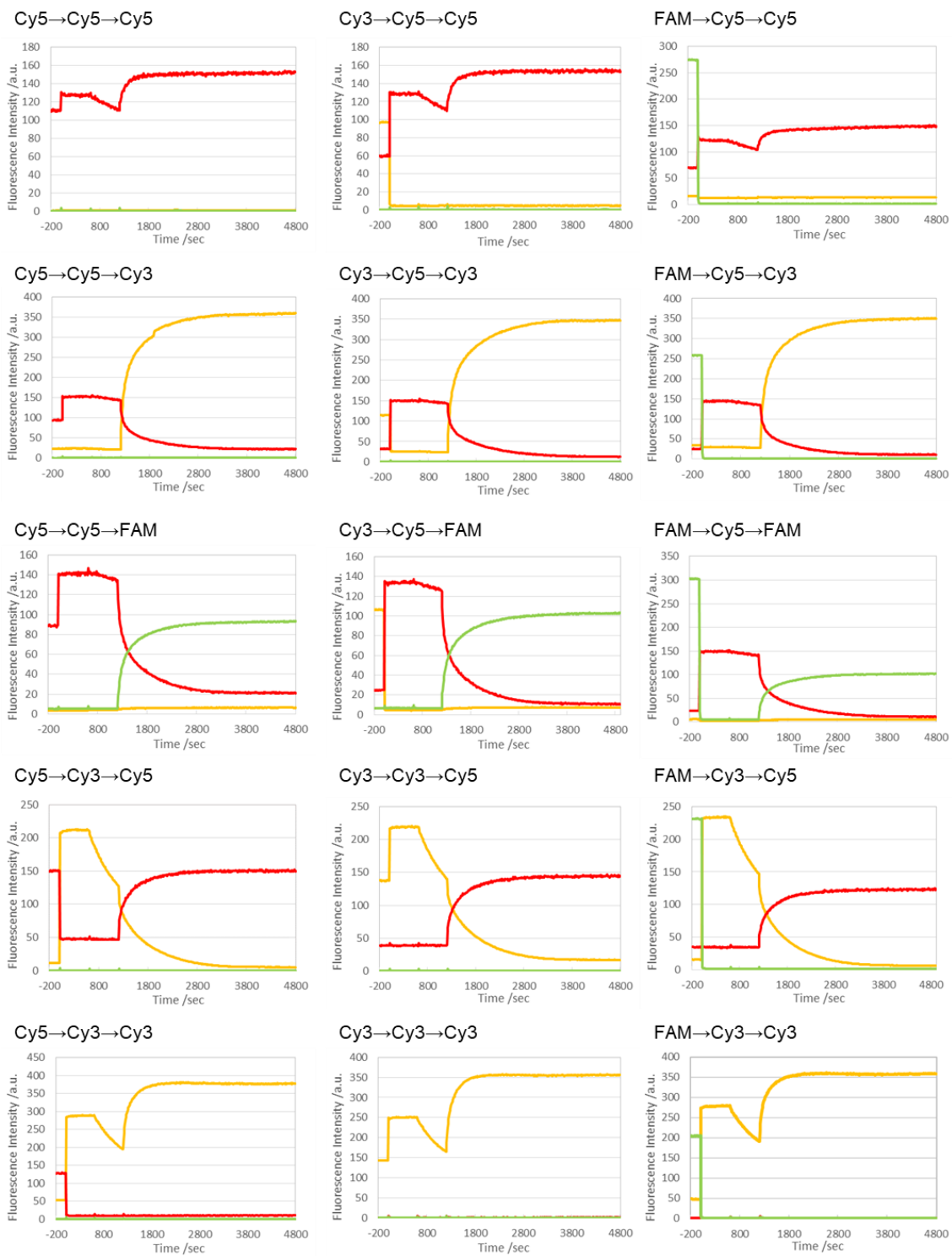


Figure S2-7. Fluorescence melting curves of barcode complex (a) 7-mer D-aTNA, (b) 10-mer D-aTNA, and (c) 10-mer DNA were obtained by monitoring Cy3 (left) and FAM (right). Conditions: 0.2 μM barcode complex, 100 mM NaCl, 10 mM phosphate buffer (pH 7.0).



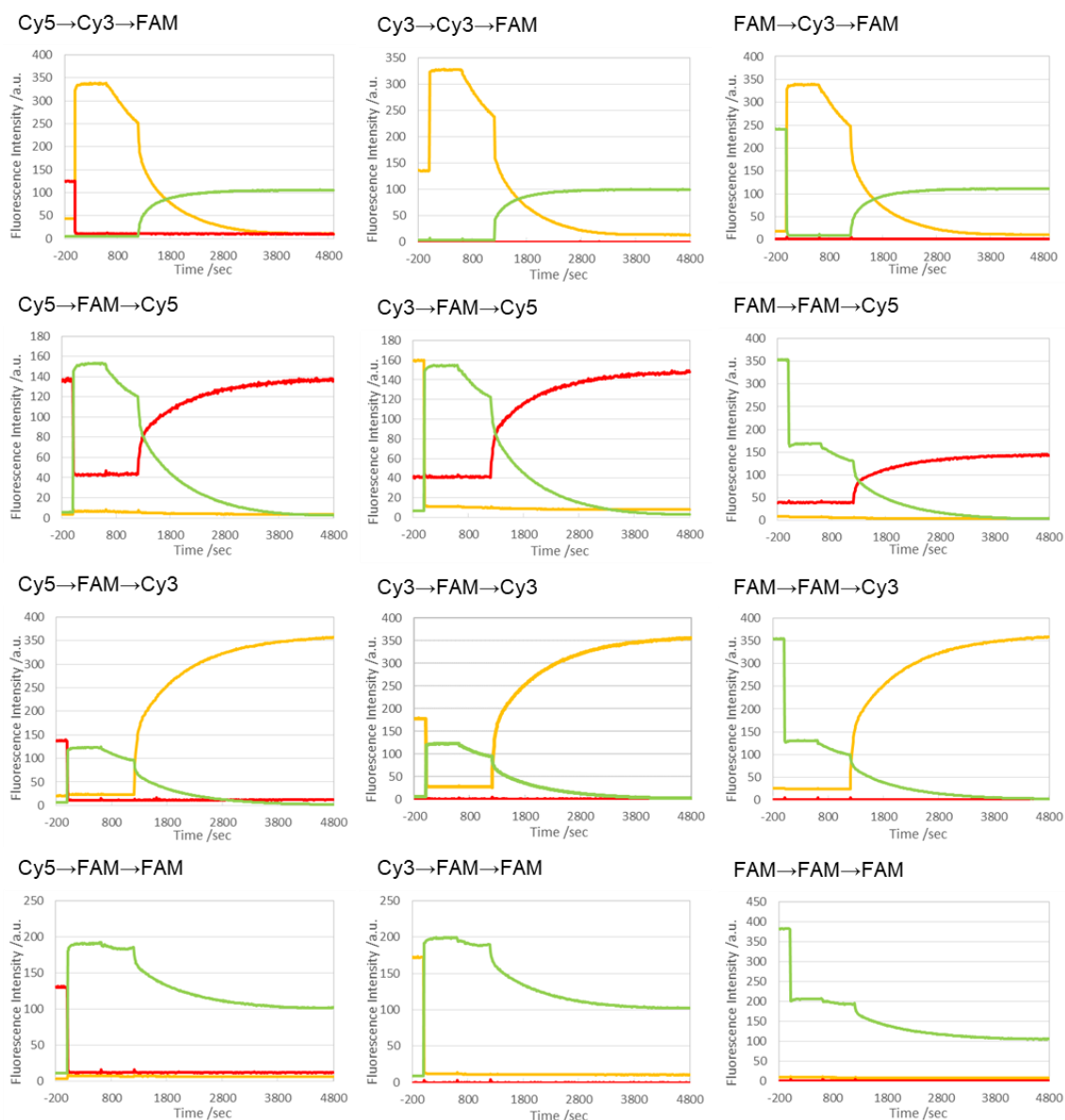


Figure S2-8. Fluorescence color changes of 27 different barcodes with 7-mer D-aTNA. Q strands were added to the barcode complex indicating the color sequence above the graph at an interval of 10 min. Conditions: 0.2 μM barcode complex, 0.4 μM Q strand, 100 mM NaCl, 10 mM phosphate buffer (pH 7.0) 20 $^{\circ}\text{C}$.

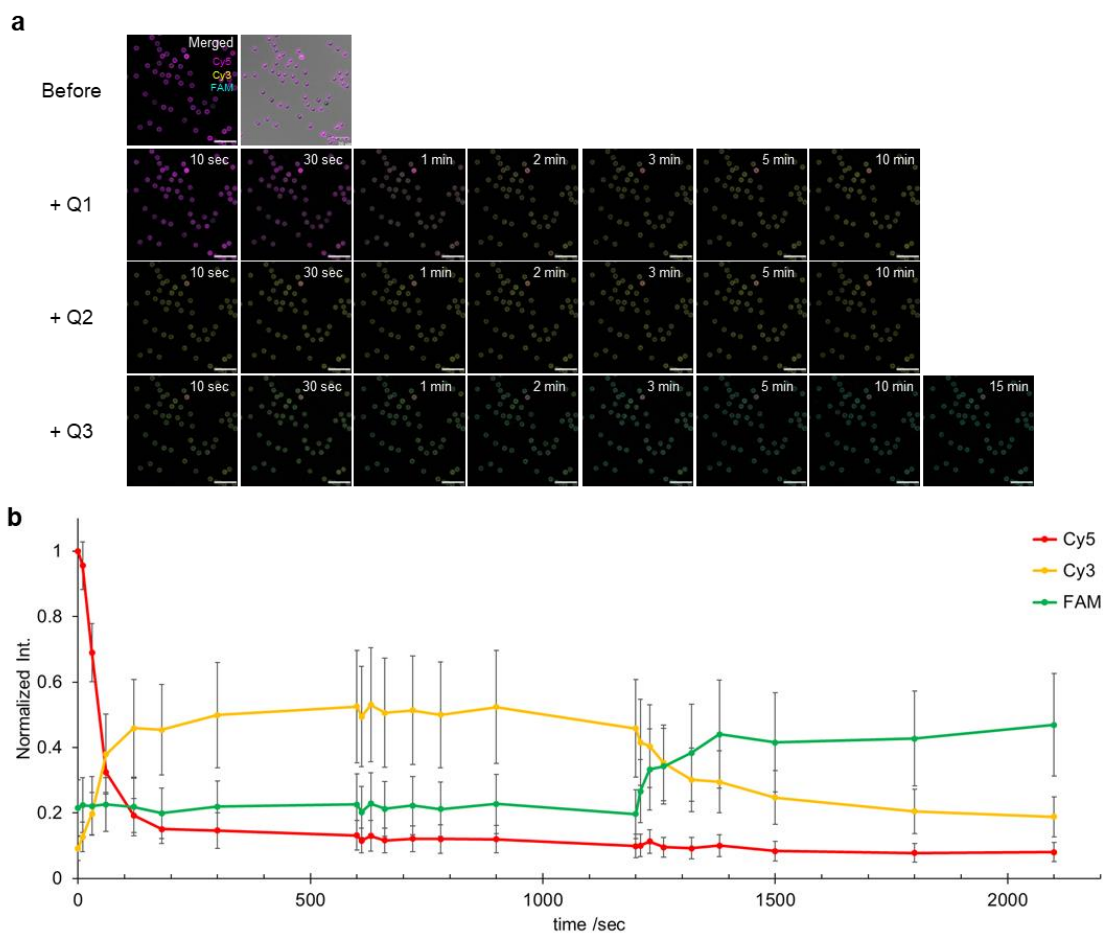


Figure S2-9. Kinetics of strand displacement reaction on beads barcoded Cy5→Cy3→FAM as monitored by fluorescence changes. (a) Fluorescent microscopy images were acquired at indicated times after the addition of Q strands (Q1, 30 pmol; Q2, 60 pmol; Q3, 90 pmol) in PBS at room temperature. Scale bars = 20 μm . (b) Fluorescence intensities of each bead were normalized for each bead to the Cy5 intensity at the initial state. Data are mean \pm SD.

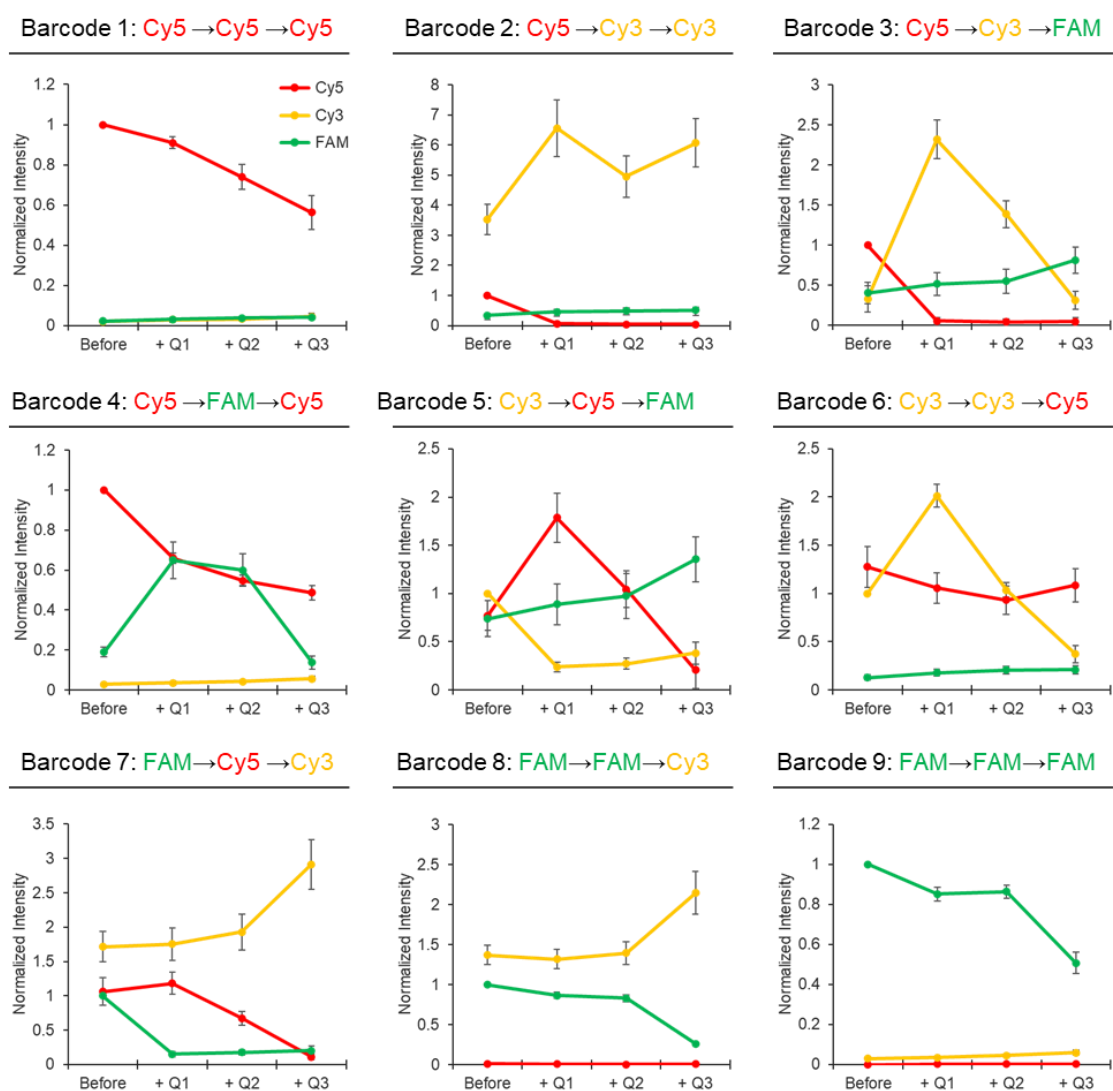


Figure S2-10. The fluorescence intensity profiles of each barcoded bead are shown in Figure 2-6b. The fluorescent intensity was normalized for each bead to the first fluorophore intensity at the initial state. Each bead was identified as one of the nine different barcodes from the fluorescence change when Q strands were added. Data are means \pm SD.

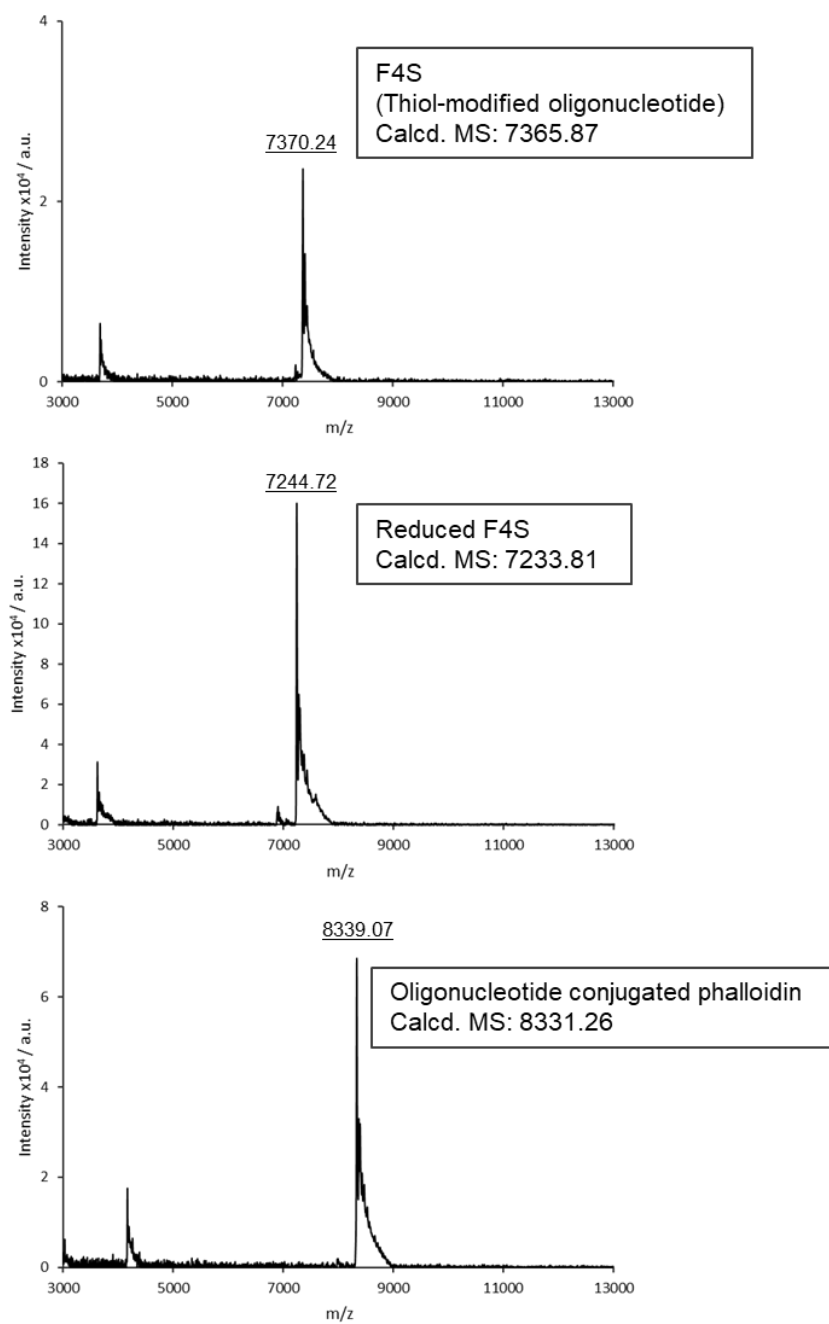


Figure S2-11. Characterization of oligonucleotide conjugated phalloidin by MALDI-TOFMS.

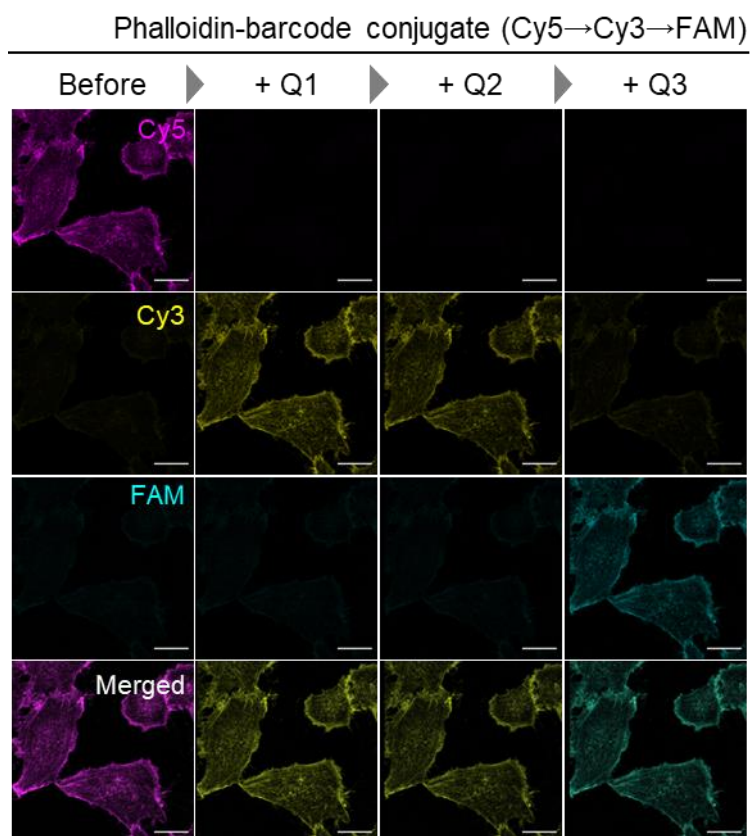


Figure S2-12. F-actin stained with phalloidin-barcode conjugate of the barcode Cy5→Cy3→FAM shown in Figure 2-7c. Scale bars = 20 μ m.

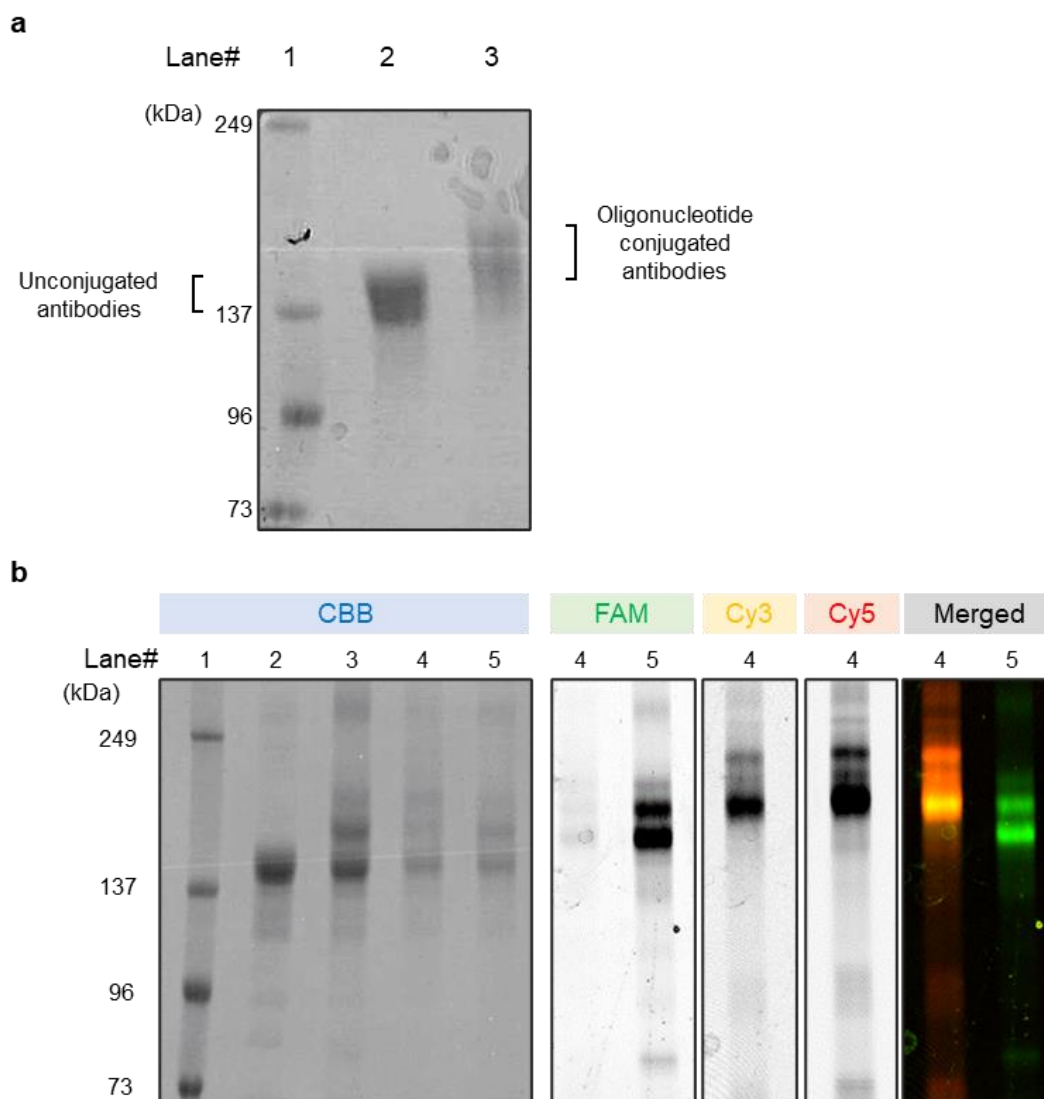


Figure S2-13. SDS-PAGE for confirming the conjugation between thiol-modified oligomers and antibodies. (a) The polyacrylamide gel was stained by Coomassie blue and acquired images. Lane #1 protein marker. Lane #2 unconjugated antibody (goat anti-mouse secondary antibody). Lane #3 oligonucleotide conjugated antibody. (b) SDS-PAGE to confirm the formation of barcode complexes on goat anti-rabbit secondary antibodies. The polyacrylamide gel was stained by Coomassie blue and imaged by using a Typhoon FLA 9500. Lane #1 protein marker. Lane #2 unconjugated antibodies. Lane #3 oligomers conjugated antibodies. Lane #4 antibodies conjugated with the barcode complex of Cy5→Cy3→FAM. Lane #5 oligomers conjugated antibodies were hybridized with only FAMF5. Merged images showing FAM (green), Cy3 (yellow), and Cy5 (red). The band shifted to the upper position when complementary F strands were added (Lane #4 and #5), thus the formation of an antibody-barcode complex was confirmed.

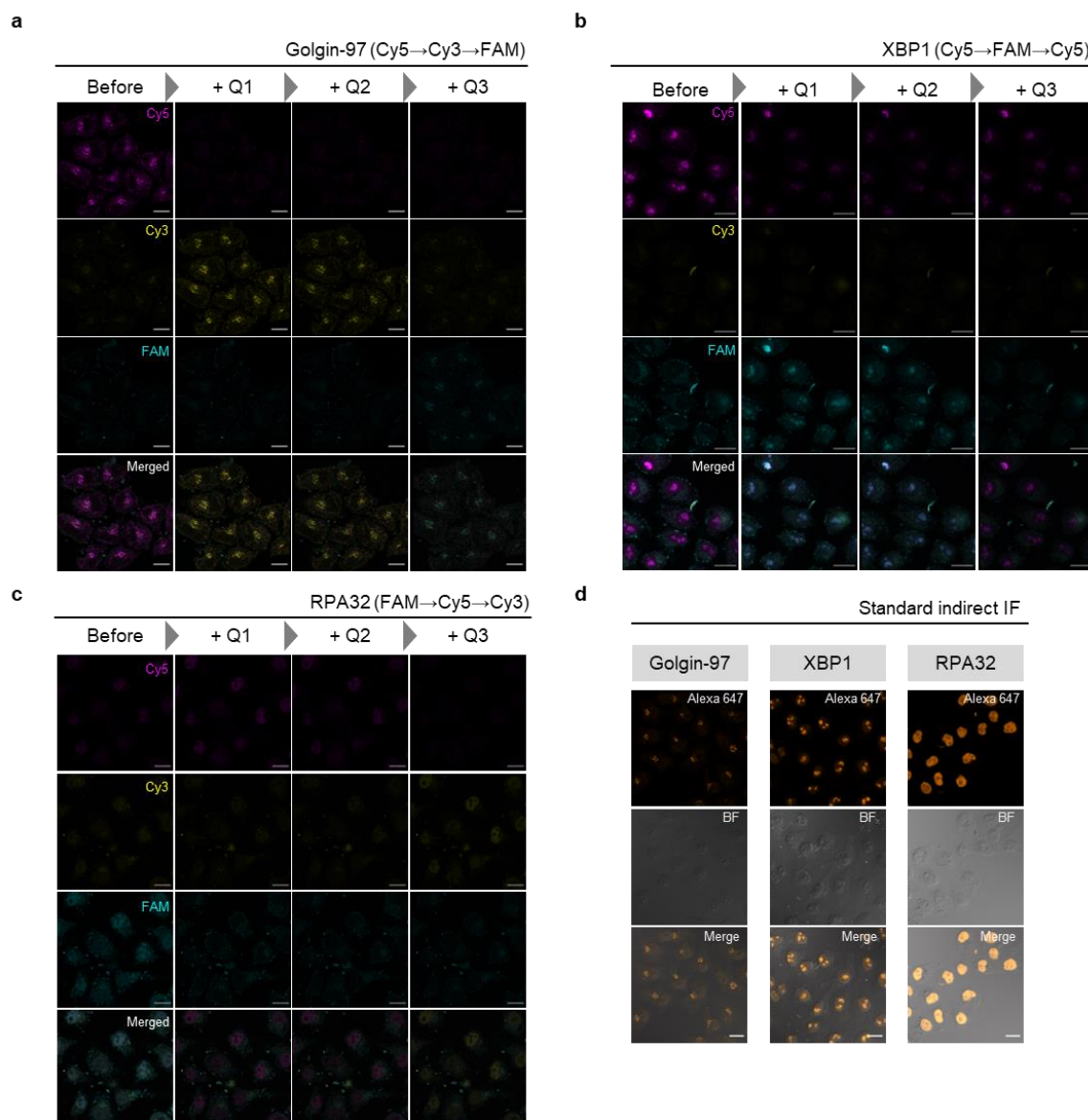


Figure S2-14. One protein imaging with antibody-barcode conjugates in the CCFB method. (a-c) Fluorescent microscopy images stained for (a) Golgin-97 with barcode of Cy5→Cy3→FAM shown in Figure 2-8c, (b) XBP1 with barcode of Cy5→FAM→Cy5 shown in Figure 2-8d, and (c) RPA32 with barcode of FAM→Cy5→Cy3 shown in Figure 2-8e. (d) Standard indirect immunofluorescence of fixed-HeLa cells stained for Golgin-97, XBP1, and RPA32 by using dye-conjugated secondary antibodies, which were goat anti-mouse Alexa 647 (Abcam, ab150119), goat anti-rabbit Alexa 647 (Abcam, ab150079), and goat anti-rat Alexa 647 (Abcam, ab150167). Scale bars = 20 μ m.

Three-protein imaging with FCCB

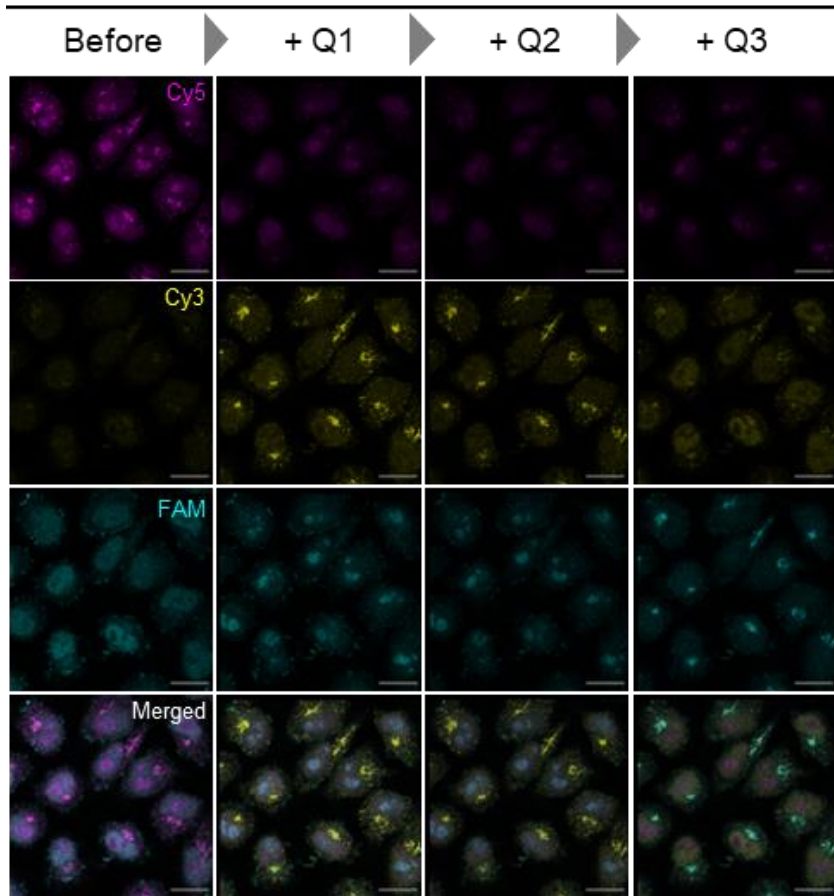


Figure S2-15. CCFB multiple protein imaging with three antibody-barcode conjugates. Fluorescent images with CCFB system for detection of Golgin-97 (Cy5→Cy3→FAM), XBP1 (Cy5→FAM→Cy5), and RPA32 (FAM→Cy5→Cy3). Scale bars = 20 μ m.

Four-protein imaging with FCCB

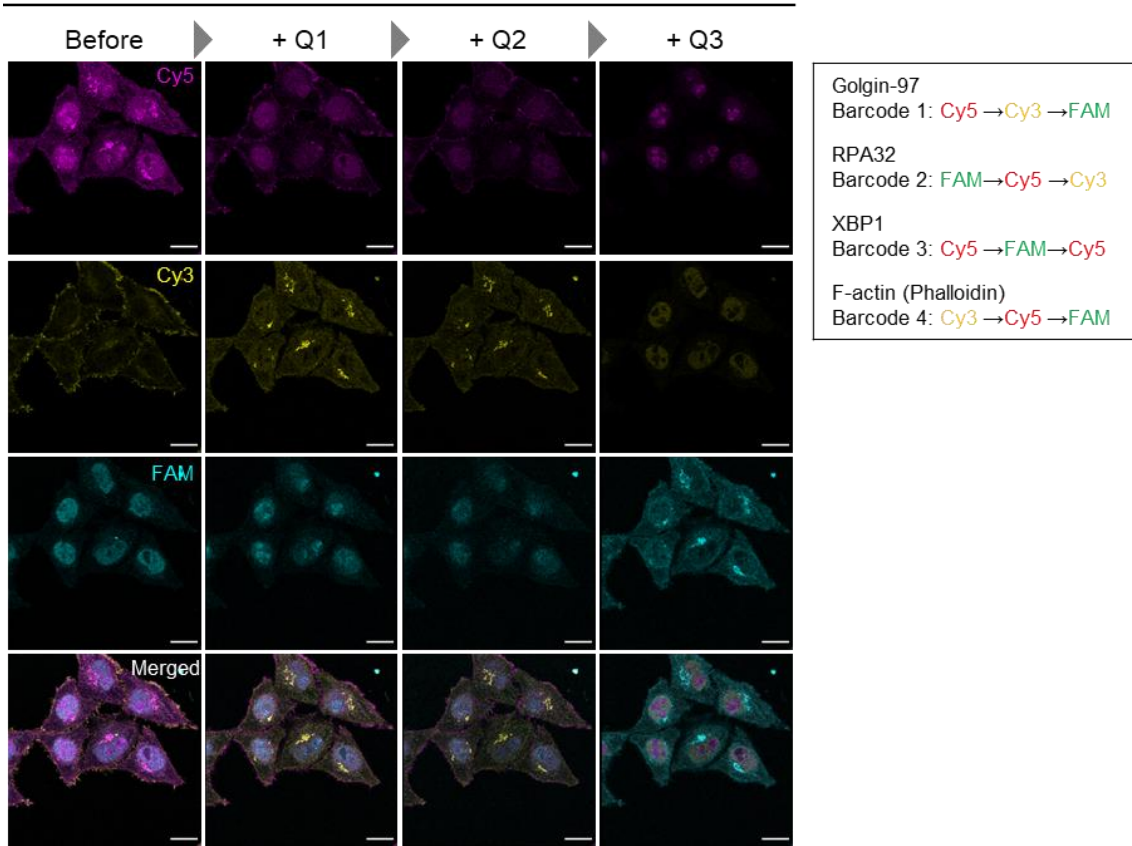


Figure S2-16. CCFB multiple protein imaging with three antibody-barcode conjugates and one phalloidin-barcode conjugate. Fluorescent images with CCFB system for detection of Golgin-97 (Cy5→Cy3→FAM), XBP1 (Cy5→FAM→Cy5), RPA32 (FAM→Cy5→Cy3), and F-actin (Cy3→Cy5→FAM). Scale bars = 20 μ m.

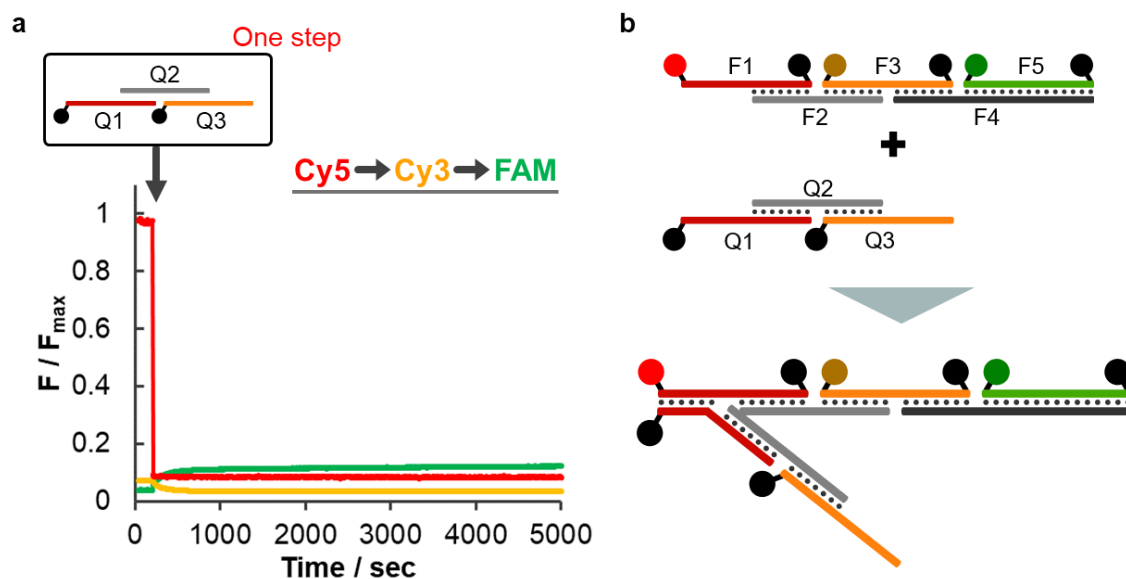


Figure S2-17. (a) Fluorescence monitoring upon the addition of the mixed three types of Q strands (Q1, Q2, and Q3) to the barcode complex of $Cy5 \rightarrow Cy3 \rightarrow FAM$. Fluorescence intensities were normalized by the maximum intensity (F_{max}) of each fluorophore when Q strands were added one by one. Conditions: $0.2 \mu M$ barcode complex, $0.4 \mu M$ Q strands, 100 mM NaCl , $10 \text{ mM phosphate buffer (pH 7.0)}$, $25^\circ C$. (b) Schematic illustration of the reaction between a barcode complex of an F strand and a Q strand complex. Two complexes form a larger structure hybridizing in the first toehold of F1 and Q1.

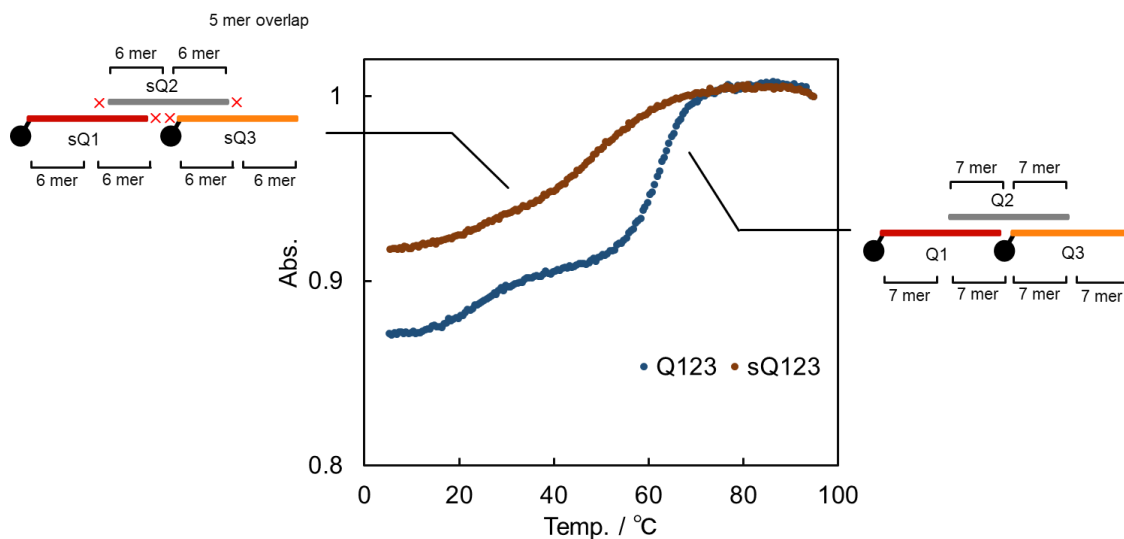


Figure S2-18. UV melting curves of the Q strand complex composed of Q1, Q2, and Q3 (blue) and the sQ complex composed of sQ1, sQ2, and sQ3 (red). Conditions: $2.0 \mu M$ barcode complex, TE/ Mg^{2+} buffer (12.5 mM MgCl_2 , $10 \text{ mM Tris-HCl (pH 8.0)}$, 1.0 mM EDTA). sQ strand complex is slightly more unstable than the Q strand complex.

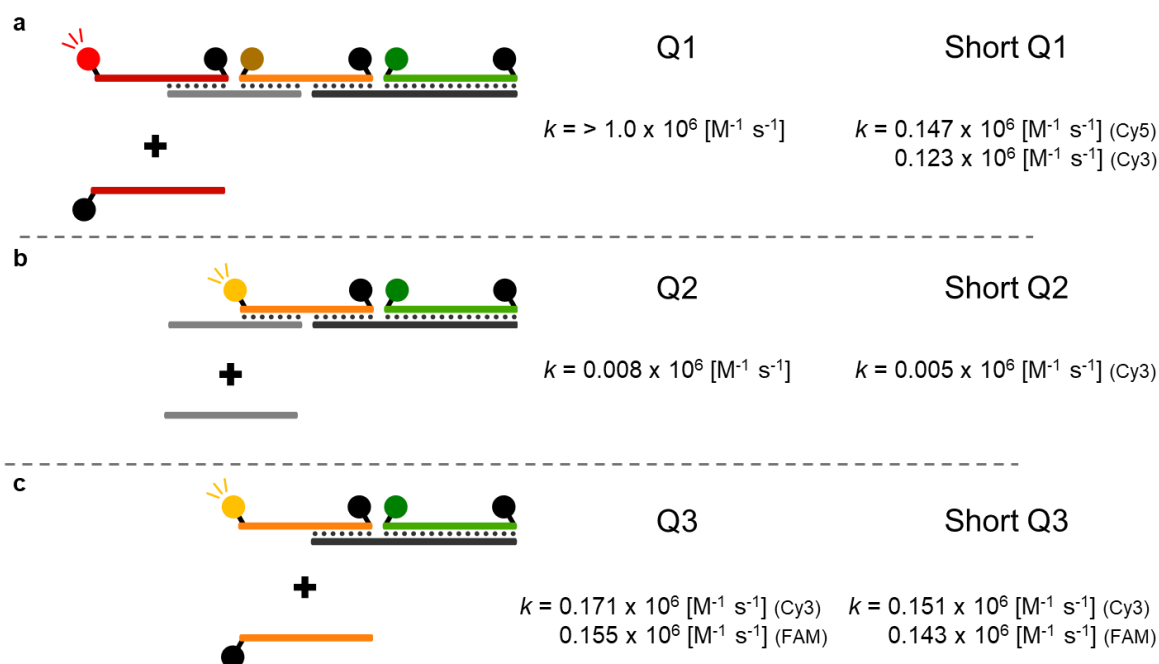


Figure S2-19. Schematic illustration and the reaction rate k of each step upon the addition of Q strands or short Q strands. (a) When Q1 reacted to the first toehold on the barcode complex, k is more than $1.0 \times 10^6 \text{ M}^{-1} \text{ s}^{-1}$. When sQ1 added, k is $0.147 \times 10^6 \text{ M}^{-1} \text{ s}^{-1}$ (monitoring Cy5) or $0.123 \times 10^6 \text{ M}^{-1} \text{ s}^{-1}$ (monitoring Cy3). (b) When Q2 was added k is $0.008 \times 10^6 \text{ M}^{-1} \text{ s}^{-1}$. When sQ2 was added k is $0.005 \times 10^6 \text{ M}^{-1} \text{ s}^{-1}$. (c) When Q3 was added, k is $0.0171 \times 10^6 \text{ M}^{-1} \text{ s}^{-1}$ (monitoring Cy3) or $0.155 \times 10^6 \text{ M}^{-1} \text{ s}^{-1}$ (monitoring FAM). When sQ3 was added, k is $0.151 \times 10^6 \text{ M}^{-1} \text{ s}^{-1}$ (monitoring Cy3) or $0.143 \times 10^6 \text{ M}^{-1} \text{ s}^{-1}$ (monitoring FAM). No significant difference in the reaction rate of Q2 vs sQ2 and Q3 vs sQ3 which means that short Q strands can be used similarly to Q strands. In contrast, the reaction upon the addition of sQ1 largely slowed down than that of Q1. We also checked the repeat base sequence in these short Q strands. The first 6-mer toehold Q1 is 1'-TGTCGT-3' which has two "GT" repeat, less than three repeats in 7-mer design. Therefore, it is suggested that the number of repeat base sequences is important for the reaction rate.

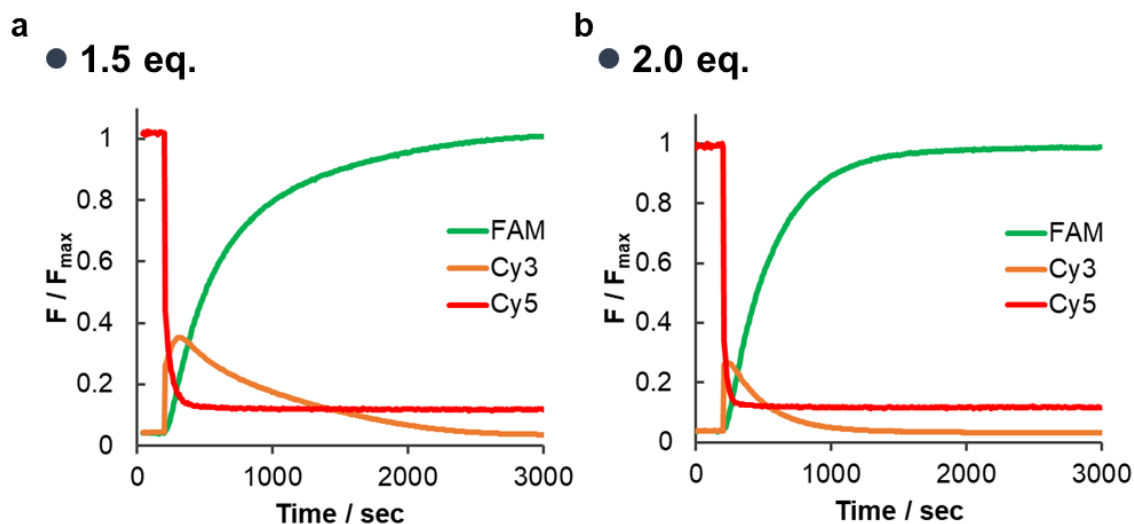


Figure S2-20. Fluorescence monitoring upon the addition of (a) 1.5 eq. or (b) 2.0 eq. mixed three types of sQ strands (sQ1, sQ2, and sQ3) to the barcode complex of Cy5→Cy3→FAM. Fluorescence intensities were normalized by the maximum intensity (F_{\max}) of each fluorophore when sQ strands were added one by one. The fluorescence of Cy3 was lower by the addition of 1.5 or 2.0 eq. sQ strands because sequential strand displacement reaction with sQ strands is fast. Conditions: 0.2 μM barcode complex, (a) 0.3 μM or (b) 0.4 μM Q strands, 100 mM NaCl, 10 mM phosphate buffer (pH 7.0), 25°C.

Table S2-1. 7-mer overlapping D-aTNA sequences and mass spectrometry data.

Name	Sequence	Obsd. MS	Calcd. MS
Cy5F1	1'-Cy5-CACAGCA ATCGCCA-Dab-3'	5555.52	5557.61
Cy3F1	1'-Cy3-CACAGCA ATCGCCA-Dab-3'	5530.02	5531.59
FAMF1	1'-FAM-CACAGCA ATCGCCA-Dab-3'	5561.10	5561.47
Cy5F3	1'-Cy5-AGGCTCT ACGGACA-Dab-3'	5631.74	5628.60
Cy3F3	1'-Cy3-AGGCTCT ACGGACA-Dab-3'	5607.05	5602.58
FAMF3	1'-FAM-AGGCTCT ACGGACA-Dab-3'	5633.66	5632.46
Cy5F5	1'-Cy5-TCCTGGA GTCGTCT-Dab-3'	5605.01	5601.57
Cy3F5	1'-Cy3-TCCTGGA GTCGTCT-Dab-3'	5577.01	5575.55
FAMF5	1'-FAM-TCCTGGA GTCGTCT-Dab-3'	5606.06	5605.43
F2	1'-AGAGCCT TGGCGAT-3'	4710.08	4708.19
F4	1'-AGACGAC TCCAGGA TGTCGGT-3'	7037.03	7037.77
F4B	1'-Biotin-AGACGAC TCCAGGA TGTCGGT-3'	7449.02	7442.92
F4S	1'-Thiol- AGACGAC TCCAGGA TGTCGGT-3'	7370.24	7365.87
Q1	1'-TGGCGAT TGCTGTG-Dab-3'	5146.88	5148.31
Q2	1'-ATCGCCA AGGCTCT-3'	4628.50	4628.19
Q3	1'-TGTCCGT AGAGCCT-Dab-3'	5078.55	5077.32

Biotin was incorporated with 5' biotin phosphoramidite (Glen Research, 10-5950).

Thiol modification was incorporated with Thiol-Modifier C6 S-S (Glen Research, 10-1936).

Cy5 was incorporated with Cyanine 5 Phosphoramidite (Glen Research, 10-5915).

Cy3 was incorporated with Cyanine 3 Phosphoramidite (Glen Research, 10-5913).

FAM was incorporated with 5'-Fluorescein Phosphoramidite (Glen Research, 10-5901).

Table S2-2: 10-mer overlapping D-aTNA sequences and mass spectrometry data.

Name	Sequence	Obsd. MS	Calcd. MS
Cy5F1	1'-Cy5-TTCAGCCGCA ATCCTCGCCT-Dab-3'	7517.52	7518.07
Cy3F3	1'-Cy3-TCAGAGCTGG ACGACAATGA-Dab-3'	7673.07	7678.09
FAMF5	1'-FAM-AAGACTCGTG CTCACCGAAT-Dab-3'	7618.98	7618.96
F2	1'-CCAGCTCTGA AGGCGAGGAT-3'	6747.78	6744.69
F4	1'-CACGAGTCTT TCATTGTCGT-3'	6650.06	6651.67
Q1	1'-AGGCGAGGAT TGC GGCTGAA-Dab-3'	7244.52	7242.83
Q2	1'-ATCCTCGCCT TCAGAGCTGG-3'	6648.17	6646.67
Q3	1'-TCATTGTCGT CCAGCTCTGA-Dab-3'	7055.18	7054.81

Cy5 was incorporated with Cyanine 5 Phosphoramidite (Glen Research, 10-5915).

Cy3 was incorporated with Cyanine 3 Phosphoramidite (Glen Research, 10-5913).

FAM was incorporated with 5'-Fluorescein Phosphoramidite (Glen Research, 10-5901).

Table S2-3. 10-mer overlapping DNA sequences.

Name	Sequence
Cy5F1	5'-Cy5-TTCAGCCGCA ATCCTCGCCT-Dab-3'
Cy3F1	5'-Cy3-TTCAGCCGCA ATCCTCGCCT-Dab-3'
Cy3F3	5'-Cy3-TCAGAGCTGG ACGACAATGA-Dab-3'
Cy5F3	5'-Cy5-TCAGAGCTGG ACGACAATGA-Dab-3'
FAMF5	5'-FAM-AAGACTCGTG CTCACCGAAT-3'
F2	5'-CCAGCTCTGA AGGCGAGGAT-3'
F4	5'-ATTCGGTGAGCACGAGTCTTTCATTGTCGT-3'
Q1	5'-AGGCGAGGAT TGC GGCTGAA-Dab-3'
Q2	5'-ATCCTCGCCT TCAGAGCTGG-3'
Q3	5'-TCATTGTCGTCCAGCTCTGA-Dab-3'

Oligonucleotides were purchased from Integrated DNA Technologies or Tsukuba Oligo Service Co., Ltd.

Dab is 3' Dabcyl modification.

Table S2-4. Signal-to-background (S/B) ratio for barcode complex with a color sequence of Cy5→Cy3→FAM.

	7-mer D- <i>a</i> TNA (20 °C)	10-mer D- <i>a</i> TNA (40 °C)	10-mer DNA (20 °C)
Cy5	-	-	-
Cy3	21.6	16.1	5.59
FAM	15.2	4.91	3.19

The ratios are maximum intensity after strand displacement reaction to minimum intensity in the initial state.

Table S2-5. Primary antibodies used in CCFB imaging.

Target	Source	Species
Golgin-97	Invitrogen (#A21270)	Mouse
XBP1	Abcam (#ab109221)	Rabbit
RPA32	CST (#2208S)	Rat

Table S2-6. Secondary antibodies used in CCFB imaging.

Target	Source	Host
Mouse	AffiniPure Goat Anti-Mouse IgG (H+L) (min X Hu, Bov, Hrs, Rb, Rat Sr Prot) Jackson ImmunoResearch Laboratories, #115-005-166	Goat
Rabbit	Goat anti-Rabbit IgG (H+L) Superclonal Secondary -Ab ThermoFisher, #A27033	Goat
Rat	AffiniPure Goat Anti-Rat IgG (H+L) (min X Hu, Bov, Hrs, Ms, Rb Sr Prot) Jackson ImmunoResearch Laboratories, #112-005-167	Goat

Table S2-7. Sequences of short Q strands in 7-mer D-*a*TNA design and mass spectrometry data.

Name	Sequence	Obsd. MS	Calcd. MS
sQ1	1'-GGCGAT TGCTGT-Dab-3'	4461.11	4457.15
sQ2	1'-TCGCCA AGGCTC-3'	3956.46	3953.02
sQ3	1'-GTCCGT AGAGCC-Dab-3'	4416.68	4411.16

Chapter 3. Kinetics of Strand Displacement Reaction with Acyclic Artificial Nucleic Acids

3-1. Abstract

Artificial nucleic acids, which give functions to natural nucleic acids, will provide a new application of DNA nanotechnology. Our group has developed artificial acyclic nucleic acids, SNA, L-*a*TNA, and D-*a*TNA, which have the potential for biological applications due to their strong hybridization capability and avoidance ability to enzyme recognition. Artificial nucleic acids provide solutions to the problems of natural nucleic acids, such as low stability in biological conditions and low yield of structural formation due to low thermal stability. The developed acyclic nucleic acids will be useful in strand displacement reaction, one of the key DNA nanotechnologies, to realize DNA computing systems even in a biological environment. However, the kinetics of strand displacement reaction with these nucleic acids remain undefined, as with most other artificial nucleic acids. Herein, we systematically analyzed the kinetics of strand displacement reaction using SNA, L-*a*TNA, and D-*a*TNA. The kinetics of these nucleic acids were partially similar to the DNA kinetics, where the reaction rate increased depending on the toehold length and saturated at a certain length. A different property of *a*TNAs from DNA is that the reaction rate of *a*TNAs increased with increasing temperature. These results will contribute to the expansion of nucleic acids nanotechnology using artificial acyclic nucleic acids.

3-2. Introduction

DNA is a unique material that hybridized with a complementary strand specifically based on the Watson-Crick base pairing rule. Toehold-mediated strand displacement reaction which was developed by using DNA programmability is one of the key technologies in DNA nanotechnology. As mentioned in chapter 1, This technique is essential to construct not only DNA machines such as DNA tweezer¹ and DNA walker² but also highly sensitive quantitation of small amounts of RNA such as HCR³. In recent years, Toehold-mediated strand displacement reaction was implemented in the prokaryotes, *E. coli* to regulate biological systems⁴⁻⁶, and will be applied to eukaryotes and *in vivo* in the near future. In considering the biological application of DNA,

however, resistance to enzymatic digestion and structural stability are important properties. In this context, to improve biological and thermal stability, and add functionality, various artificial nucleic acids have been developed⁷⁻⁸. For example, the rational design of introducing locked nucleic acid (LNA)⁹ to DNA has been proposed for the reduction of leakage strand displacement reaction¹⁰. In addition, peptide nucleic acid (PNA)¹¹⁻¹² which hybridize to both D-DNA and L-DNA have been used to develop heterochiral strand displacement reaction circuits¹³⁻¹⁴. In this heterochiral reaction, the D-DNA input strand hybridizes to the toehold of PNA which forms the L-DNA/PNA hetero-duplex and then allows to displace L-DNA output. Therefore, PNA can exchange the information from the D-input to L-output. Interestingly, this heterochiral reaction would be slower than the homochiral reaction in which D-DNA input releases D-DNA via the PNA interface. However, there are very few applications if strand displacement reaction using artificial nucleic acids.

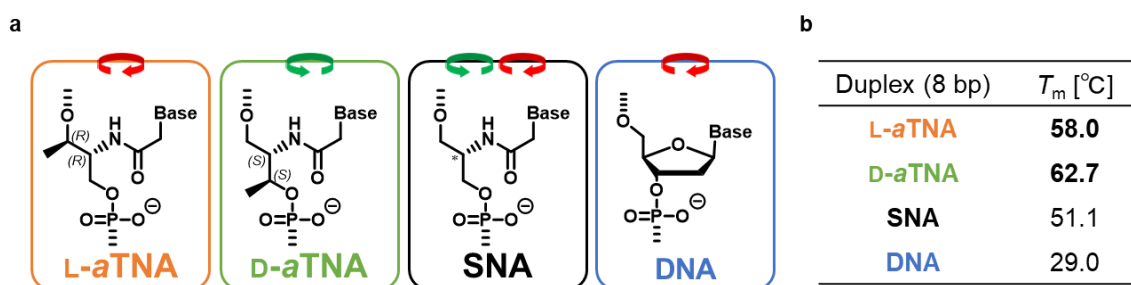


Figure 3-1. (a) Chemical structure and helicity of L-aTNA, D-aTNA, SNA, and DNA. (b) Melting temperature T_m of homo-duplex in same base sequence. Conditions: [ONs] = 2.0 μ M, 100 mM NaCl, 10 mM phosphate buffer. Referred from Ref. 15-17.

Our group has developed acyclic artificial nucleic acids, SNA¹⁵, L-aTNA¹⁶, and D-aTNA¹⁷ (Figure 3-1). These nucleic acids form a very stable duplex whose melting temperatures T_m are more than 20 °C higher than that of DNA and have resistant to enzymes. L-aTNA forms a right-handed double helix and D-aTNA forms a left-handed double helix, whereas SNA forms either of right-handed and left-handed double helix depending on the base sequence or the helicity of complementary strand because the SNA monomer is an achiral backbone. Thus, SNA is a unique oligomer that hybridizes with L-aTNA and D-aTNA similar to PNA. Using these acyclic artificial nucleic acids, our group has developed a D-aTNA orthogonal see-saw gate amplification system¹⁸ and an orthogonal HCR composed of L-/D-aTNA to detect RNA¹⁹ (Figure 3-2).

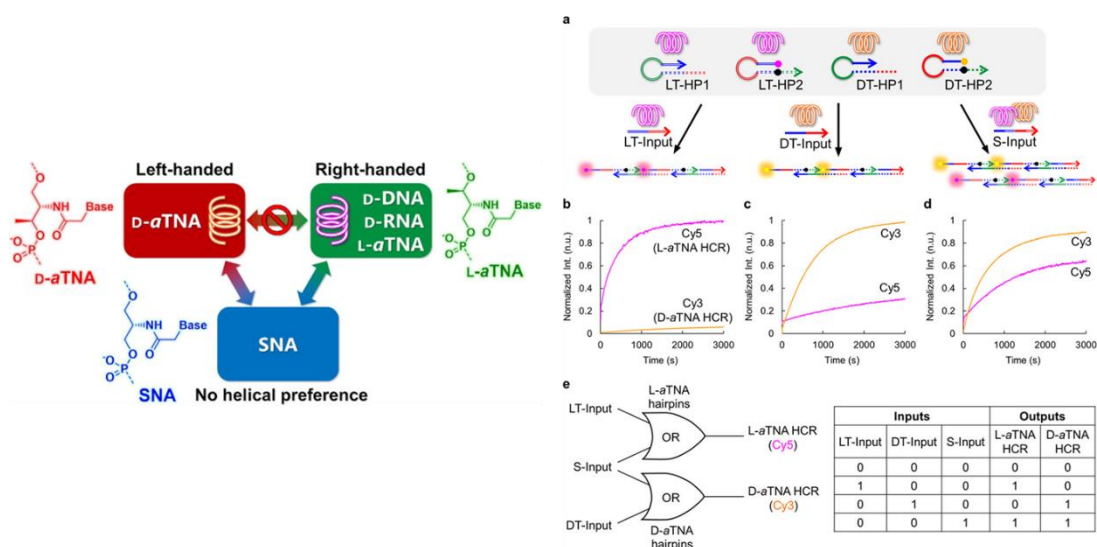


Figure 3-2. Orthogonal amplification circuits system exploited a helicity difference among L-aTNA, SNA, D-aTNA, and natural nucleic acids. Reprinted from Ref. 19.

These acyclic artificial nucleic acids will be useful for the development of nucleic acid circuit systems in biological environments because of the advantages of thermal and biological stability. Moreover, we devised that SNA can be used to control kinetics by heterochiral strand displacement system as well as PNA. In the DNA strand exchange system, the kinetics of the reaction has been well studied and leakless designs have been also proposed²⁰⁻²¹, whereas the kinetics of strand displacement reaction with artificial nucleic acids are unexplored. The kinetics with SNA, L-aTNA, and D-aTNA are also lacking in understanding, which prevents their applications.

Herein, this study aimed to unravel the kinetics of strand displacement reaction with artificial nucleic acids for the application of nucleic acid nanotechnology, we systematically analyzed the reaction rate. In particular, we investigated the possibility of a heterochiral strand displacement system with an SNA interface, systematical kinetics analysis of homochiral strand displacement reaction compared to DNA, effects of the reaction temperature, and orthogonality between L-aTNA and D-aTNA. The results of this study will provide important basic research for extending nucleic acid nanotechnology with artificial nucleic acids.

3-3. Design to study kinetics of strand displacement reaction

We designed a one-step strand displacement reaction system to monitor the progress of the reaction. This system consists of input strand (In) and reporter complex (R), where fluorophore strand (F) tethered a fluorophore was quenched by a complementary strand tethered a quencher in the initial state (Figure 3-3a). The input strands hybridize to the toehold domain reporter complex, and fluorophore strands are displaced and then emit fluorescence. Monitoring the fluorescence enables to obtain the reaction rate of strand displacement reaction. The oligomers with SNA, L-*a*TNA, D-*a*TNA, and DNA were prepared to study the effects of different backbones (Figure 3-3b). The directions of oligomer arrows were defined to hybridize in anti-parallel as shown in Figure 3-3b, and the list of oligomer sequences is shown in Table 3-1 and S3-1. To investigate the effects of the toehold length, which corresponds to the length of domain 2, some different lengths (2-15 nt) of the input strands were prepared. The length of domain 1 is 10 nt which is sufficient length to form a duplex with acyclic nucleic acids.

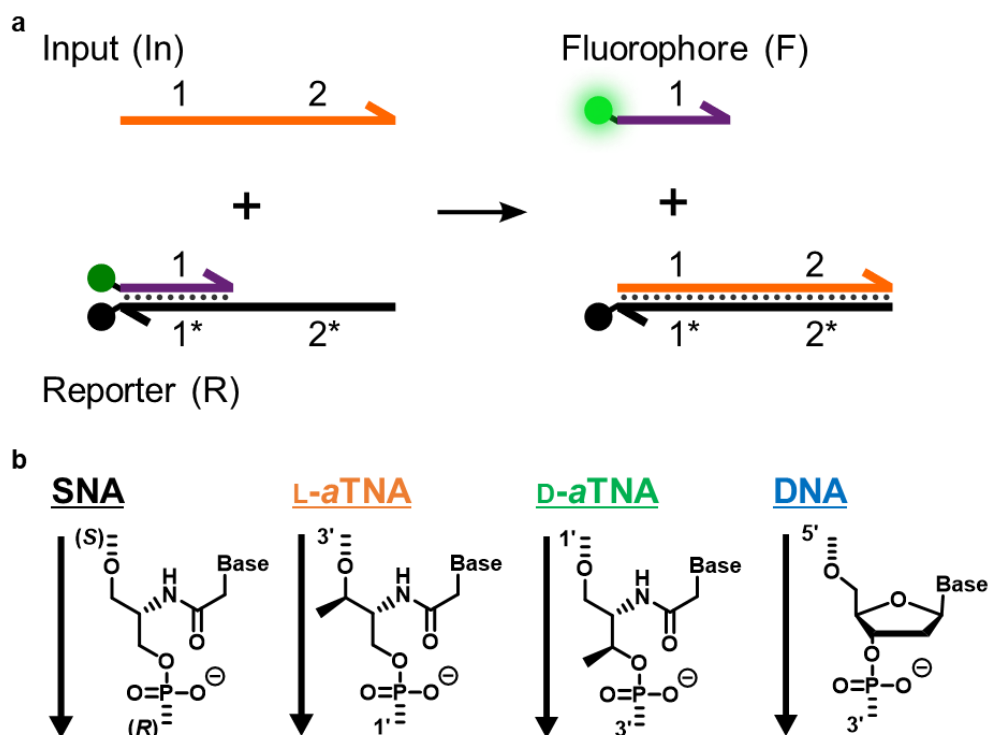


Figure 3-3. (a) Schematic illustration of a one-step strand displacement reaction to analyze the kinetics. The addition of input strand (In) causes strand displacement reaction with reporter complex (R), releasing fluorophore strand (F), and then emitting fluorescence. (b) Definition of the arrows in each nucleic acid. SNA is (S) to (R) direction. L-*a*TNA is 3' to 1' direction. D-*a*TNA is 1' to 3' direction. DNA is 5' to 3' direction.

Table 3-1. Sequences of each nucleic acid.

Sequence	
Input (→)	CCTACTACCG CTTGACACTTATTAC
F (→)	FAM CCTACTACCG
Q (←)	Dab GGATGATGGC GAACTGTGAATAATG

3-4. Results and discussions

3-4-1. Heterochiral strand displacement reaction with artificial nucleic acids

We first examined heterochiral strand displacement reaction with S-Q strands which forms reporter complexes (S-R, LS-R, and DS-R) with S-F, L-F, and D-F. FAM fluorescence upon the addition of S-In, L-In, or D-In, whose toehold length was from 2 to 15 nt, was monitored and then the reaction rate constants k was calculated by fitting the fluorescence data (Table S3-2). The values of k are plotted semilogarithmically against the toehold length (Figure 3-4 and Figure S3-1). Figure 3-4a shows the result when S-In was added to three types of reporter complexes. The reaction rate of the homoduplex of S-R was slightly faster than the heteroduplex of LS-R and DS-R, which assumed that the stabilization or helicity slowed down the reaction (Figure S3-2). Figure 3-4b shows the result when L-In was added to reporter complexes. No significant difference in the reporter types was observed. Figure 3-4c shows the result when D-In was added to reporter complexes. The heterochiral reaction upon the addition of D-In to LS-R slightly slowed down than D-In to S-R or DS-R. In summary, a few heterochiral effects (the addition of D-In to LS-R) are observed, but in general, there are little differences in all combinations between the input and reporter with SNA, L-*a*TNA, and D-*a*TNA. The helicity changes between L-*a*TNA and D-*a*TNA may not inhibit the strand displacement reaction, which will be effective for orthogonal systems via SNA interface, such as L-*a*TNA input → D-*a*TNA output.

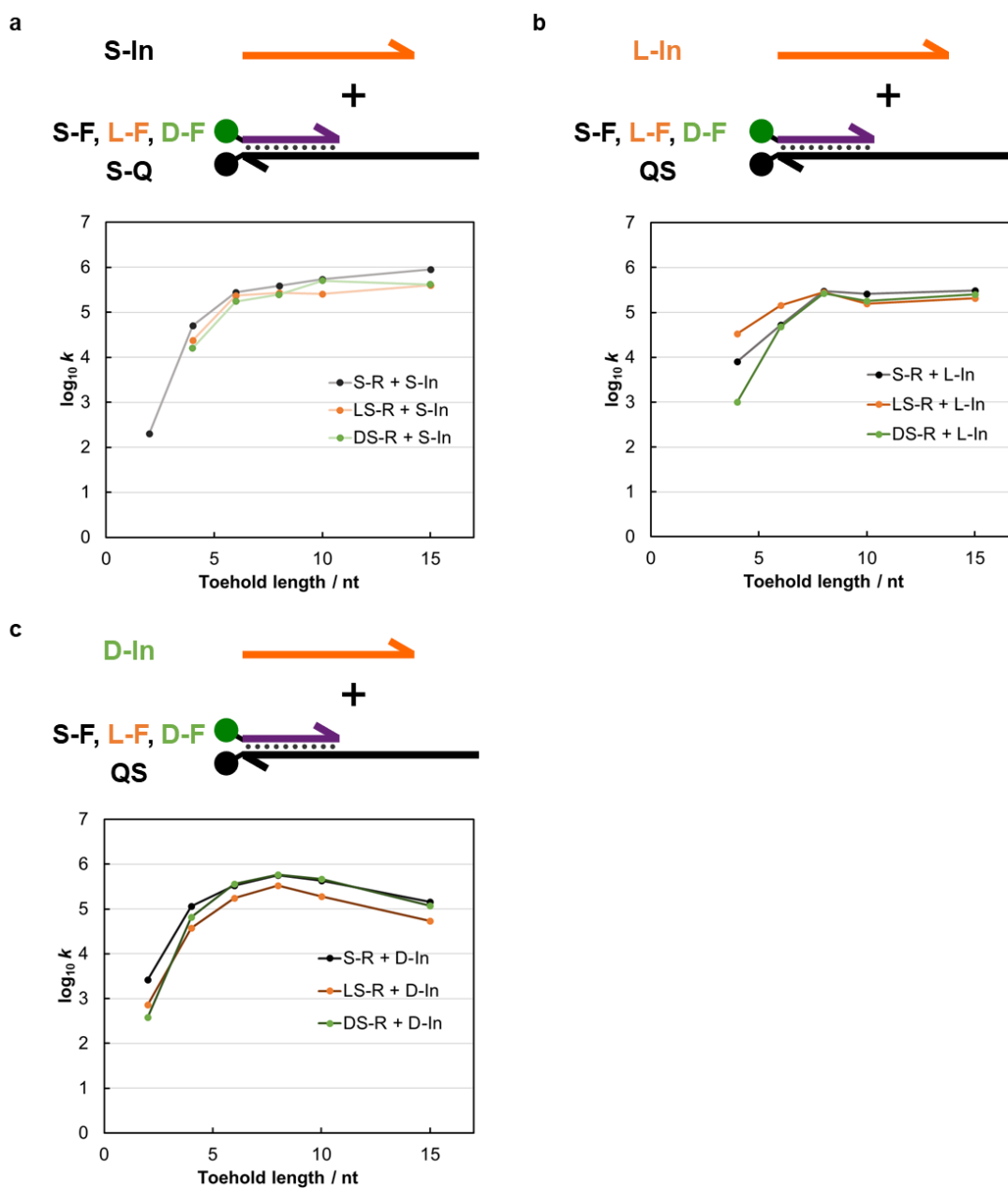


Figure 3-4. Summary of strand displacement rate constants k plotted against the toehold length. The y-axis shows the base 10 logarithm. (a-c) The addition of (a)S-In, (b) L-In, or (c) D-In to S-R (black), LS-R (orange), DS-R (green). Conditions: $[R] = 50-150$ nM, $[In] = 75-1500$ nM, TE/Mg²⁺ buffer (12.5 mM MgCl₂, 10 mM Tris-HCl (pH 8.0), 1.0 mM EDTA), 1 μ M dT₂₀ carrier strands, 25 °C, Ex. = 488 nm, Em. = 520 nm. The details of oligomer concentration are shown in the appendix.

3-4-2. The kinetics of strand displacement reaction with artificial nucleic acids

We next examined the strand displacement reaction with a general toehold length of 6 nt (SNA: S-In6, L-aTNA: L-In6, D-aTNA: D-In6, DNA: DNA-In6) at 25°C (Figure 3-5). Reaction rate constants k were calculated from the fluorescence data. The fluorescence intensity was increased upon the addition of the input strands, where the reaction was assumed to be completed in the second order. As a result, the reaction rate constant in DNA was $k_{(DNA, 6)} = 0.572 \times 10^6 \text{ M}^{-1} \text{ s}^{-1}$. The reaction rate constants in SNA, L-aTNA, and D-aTNA were slightly lower, $k_{(S, 6)} = 0.277 \times 10^6 \text{ M}^{-1} \text{ s}^{-1}$, $k_{(L, 6)} = 0.028 \times 10^6 \text{ M}^{-1} \text{ s}^{-1}$, $k_{(D, 6)} = 0.226 \times 10^6 \text{ M}^{-1} \text{ s}^{-1}$, respectively.

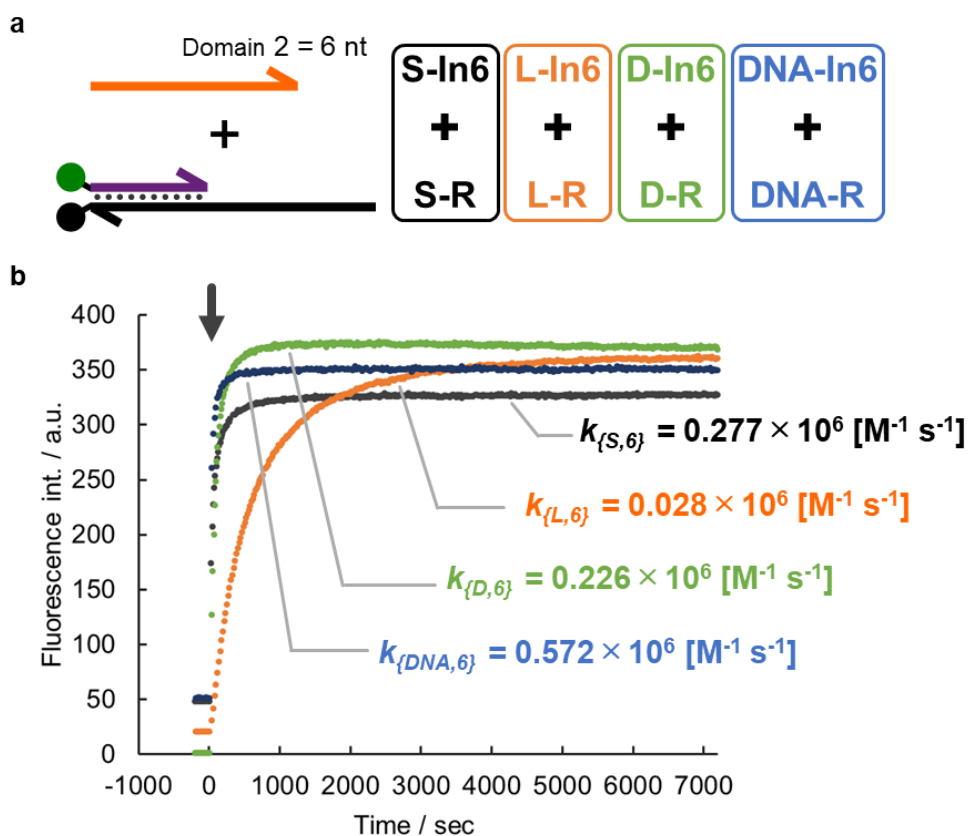


Figure 3-5. (a) Schematic illustration of strand displacement reaction with the input of 6 nt toehold length. SNA: S-In6 + S-R, L-aTNA: L-In6 + L-R, D-aTNA: D-In6 + D-R, DNA: DNA-In6 + DNA-R. (b) Fluorescence monitoring of strand displacement reaction with SNA, L-aTNA, D-aTNA, and DNA combinations. The input strand was added at the time point indicated by arrows. Conditions: $[R] = 50 \text{ nM}$, $[In] = 75 \text{ nM}$, TE/Mg²⁺ buffer (12.5 mM MgCl₂, 10 mM Tris-HCl (pH 8.0), 1.0 mM EDTA), 1 μM dT₂₀ carrier strands, 25 °C, Ex. = 488 nm, Em. = 520 nm.

We next performed the same measurements by varying the toehold length from 2 to 15 nt to systematically investigate the effects of the toehold length (Table S3-3). The values of k are plotted semilogarithmically against the toehold length as shown in Figure 3-6. The reaction rate of DNA increased with increasing toehold length until about 6 nt and reached a plateau which was about $1.0 \times 10^6 \text{ M}^{-1} \text{ s}^{-1}$. This observation is well consistent with the study of DNA strand exchange reaction²⁰. The reaction rates of SNA, L-*a*TNA, and D-*a*TNA also increased with increasing toehold length and reached a plateau, whereas the values k were decreased at all toehold lengths than DNA.

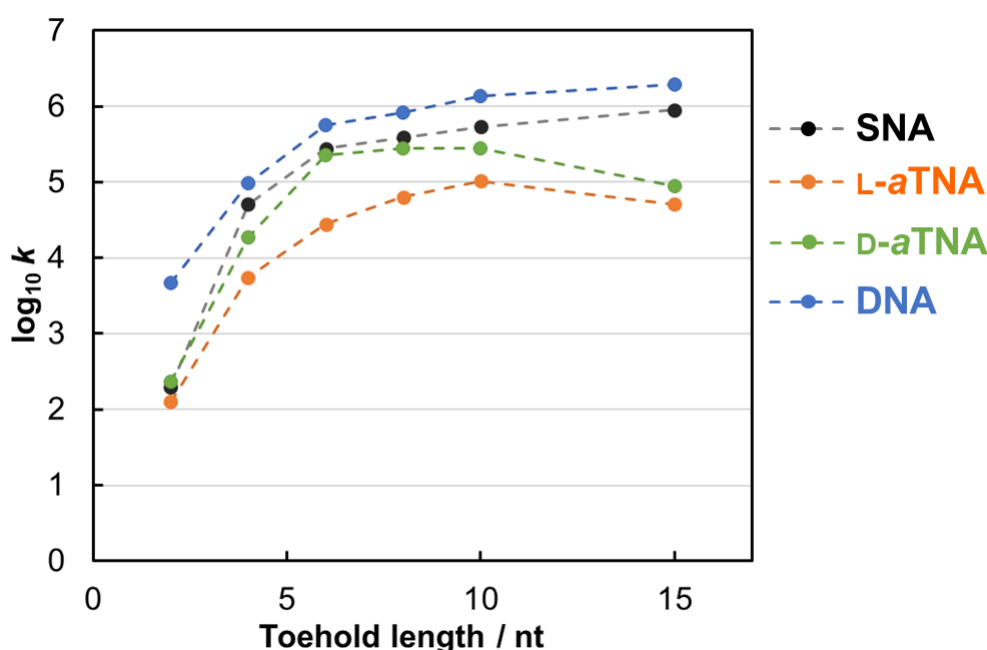


Figure 3-6. Summary of strand displacement rate constants k plotted against the toehold length. The y-axis shows the base 10 logarithm. Conditions: $[R] = 50\text{-}150 \text{ nM}$, $[In] = 75\text{-}1500 \text{ nM}$, TE/Mg²⁺ buffer (12.5 mM MgCl₂, 10 mM Tris-HCl (pH 8.0), 1.0 mM EDTA), 1 μM dT₂₀ carrier strands, 25 °C, Ex. = 488 nm, Em. = 520 nm. The details of oligomer concentration are shown in the appendix.

3-4-3. Thermodependency of strand displacement reaction

We assumed that the reaction rates decreased due to the strong formation of acyclic artificial nucleic acids. The melting temperature T_m of DNA 10 bp reporter duplex was 37.0 °C, whereas the T_m of SNA, L-*a*TNA, and D-*a*TNA was significantly higher at 54.6 °C, 66.1 °C, and 74.0 °C, respectively (Figure S3-3). This hybridization stability may require an appropriate high temperature for strand displacement reaction. We next investigated the thermodependency of

strand displacement reaction at temperatures from 10 to 45 °C by using input strands of 6 nt toehold length (Figure 3-7, and Table S3-4). DNA reporter duplex cannot form stable duplex at 45 °C, thus was reacted up to 29 °C. The DNA reaction rate constant k increased little with increasing temperature, $0.533 \times 10^6 \text{ M}^{-1} \text{ s}^{-1}$ at 21 °C and $0.746 \times 10^6 \text{ M}^{-1} \text{ s}^{-1}$ at 29 °C, only about 1.3-fold. In contrast, the reaction of L-*a*TNA and D-*a*TNA was over 21 times faster with increasing temperature, for example, the value k of D-*a*TNA was $0.118 \times 10^6 \text{ M}^{-1} \text{ s}^{-1}$ at 21 °C but $2.52 \times 10^6 \text{ M}^{-1} \text{ s}^{-1}$ at 45 °C, and the value k of L-*a*TNA was $0.015 \times 10^6 \text{ M}^{-1} \text{ s}^{-1}$ at 21 °C but $0.519 \times 10^6 \text{ M}^{-1} \text{ s}^{-1}$ at 45 °C. This thermodependency of L-*a*TNA and D-*a*TNA is a remarkable feature lacking in DNA. The improvement of reaction rate supposed that stable reporter duplexes disrupted branch migration due to the large energy barrier by strong base pairing. The reaction rate k of SNA showed a moderate dependence on temperature, probably because of lower duplex stability than L-*a*TNA and D-*a*TNA. Notably, the reaction rate of D-*a*TNA increases at high temperatures as much as or more than that of DNA.

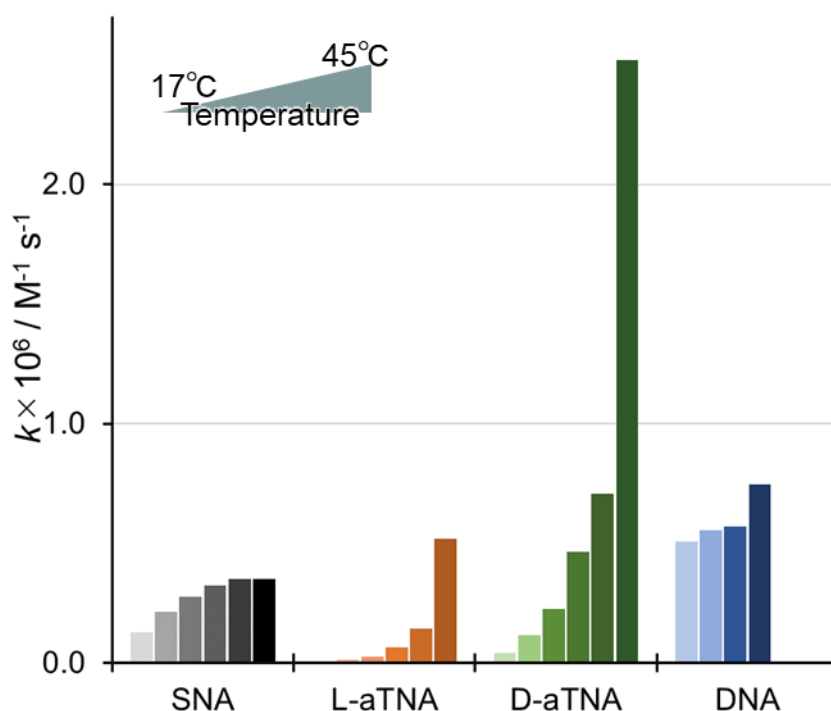


Figure 3-7. Summary of strand displacement rate constants k at various temperatures. Conditions: $[R] = 50 \text{ nM}$, $[In] = 75 \text{ nM}$, TE/Mg²⁺ buffer (12.5 mM MgCl₂, 10 mM Tris-HCl (pH 8.0), 1.0 mM EDTA), 1 μM dT₂₀ carrier strands, 17, 21, 25, 29, 35, 45 °C, Ex. = 488 nm, Em. = 520 nm.

3-4-4. Orthogonal strand displacement reaction system

L-*a*TNA and D-*a*TNA enantiomers cannot hybridize with each other, thus it will allow to design the orthogonal strand displacement reaction. Specifically, the L-*a*TNA reporter can react with the L-*a*TNA input strand but cannot react with D-*a*TNA input, whereas the D-*a*TNA reporter can react with D-*a*TNA input but cannot react with L-*a*TNA. This system will expand nucleic acid nanotechnology including DNA computing. The fluorescence monitoring of the orthogonal strand displacement reaction system with L-*a*TNA reporter (Figure 3-8a) and D-*a*TNA reporter (Figure 3-8b) showed expected orthogonality because the desired fluorescence increases were observed. Only the addition of D-In10 to the L-*a*TNA reporter resulted in slight fluorescence. This result suggested an unexpected interaction between L-*a*TNA and D-*a*TNA. As a result, the high orthogonality in strand displacement reaction with L-*a*TNA and D-*a*TNA was confirmed and will help in the development of new orthogonal nucleic acid nanotechnology.

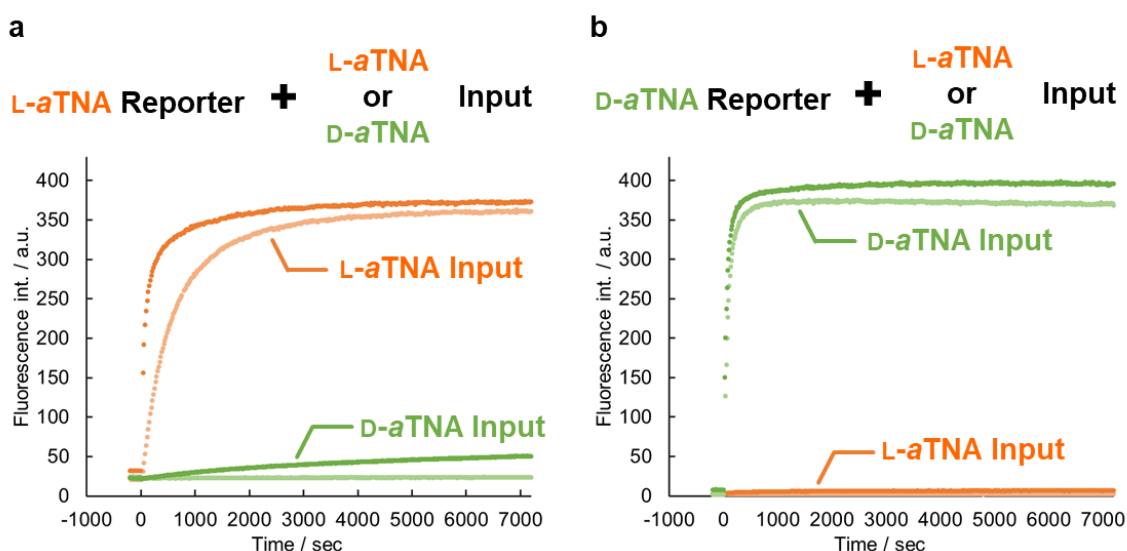


Figure 3-8. Fluorescence monitoring of strand displacement reaction with (a) L-*a*TNA reporter and (b) D-*a*TNA reporter upon the addition of L-In10 (dark orange), L-In6 (light orange), D-In10 (dark green), and D-In6 (light green). Conditions: [R] = 50 nM, [In] = 75 nM, TE/Mg²⁺ buffer (12.5 mM MgCl₂, 10 mM Tris-HCl (pH 8.0), 1.0 mM EDTA), 1 μM dT₂₀ carrier strands, 25 °C, Ex. = 488 nm, Em. = 520 nm.

3-5. Conclusion

First, we investigated the kinetics of the heterochiral strand displacement reaction between D-*a*TNA and L-*a*TNA via an SNA interface. No significant difference in the reaction rates was observed for any combinations among acyclic nucleic acids. This result is somewhat inconsistent with the study of the PNA heterochiral system¹⁴. This is likely due to the difference between SNA and PNA. PNA hybridizes to the enantiomer of D-DNA and L-DNA which have the same base sequence, whereas D-*a*TNA and L-*a*TNA oligomers that hybridize to certain SNA oligomer are not enantiomers. As shown in the list of oligomer sequences in Table S3-1, D-*a*TNA and L-*a*TNA have reverse base sequences. In addition, no difference in the heterochiral system using acyclic nucleic acids indicated that input information of L-*a*TNA convert to orthogonal D-*a*TNA output easily. Therefore, the heterochiral system will be applied to the high detection system of natural DNA and RNA, and novel bioorthogonal nucleic acid machine.

Next, the kinetics of strand displacement reaction using SNA, L-*a*TNA, and D-*a*TNA with toehold length were compared to that of DNA. The reaction rate increased depending on the toehold length up to about 6 nt but remained almost constant above that length, and these observations were consistent with those of DNA. Therefore, SNA, L-*a*TNA, and D-*a*TNA can be used in the same design as DNA. In contrast, the reaction rates of acyclic nucleic acids were slower than that of DNA, which is likely due to their greatly increased binding affinity. We also investigated the kinetics at different reaction temperatures, which revealed that the reaction rates of D-*a*TNA and L-*a*TNA increased significantly with increasing temperature. This remarkable feature is not seen in DNA and is likely due to the extremely stable base pairing of *a*TNAs. We believe that a detailed analysis of reactions using artificial nucleic acid will provide new functions and insights into nucleic acids.

We also confirmed the orthogonality between L-*a*TNA and D-*a*TNA as in a previous study¹⁹. Therefore, a nucleic acid circuit with L-*a*TNA and D-*a*TNA can work independently of each other. In particular, D-*a*TNA possesses biorthogonality in which it forms no duplex with natural nucleic acids and is hardly recognized by enzymes, thus independent nucleic acid computer will work under biological conditions and *in vivo*.

3-6. Experimental section

Preparation of oligomers

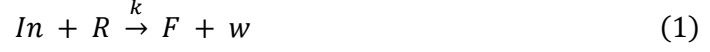
T, G, A, C, and Dabcyl D-*a*TNA monomers were synthesized according to the reported procedures^{17, 22-23}. The D-*a*TNA oligomers were synthesized on an automated DNA synthesizer (H-8-SE, Gene World) by using synthesized phosphoramidite D-*a*TNA monomers and standard reagents. Amino lcaa CPG (Controlled Pore Glass) 500-Å support (ChemGenes) tethering D-*a*TNA monomers was used as a solid support. The coupling efficiency of D-*a*TNA monomers was as high as that of the conventional monomers, as judged by the coloration of the released trityl cation. After the recommended work-up, oligomers were purified by RP-HPLC and were characterized by MALDI-TOFMS (Autoflex, Bruker Daltonics). All SNA, L-*a*TNA, D-*a*TNA, and DNA oligomers used in this report are listed in Table S3-1).

Fluorescence measurements

The fluorescence measurements were performed on a JASCO model FP-8500. Dried oligomers for reporter complex (F and Q strands) were dissolved in TE/Mg²⁺ buffer (12.5 mM MgCl₂, 10 mM Tris-HCl (pH 8.0), 1.0 mM EDTA). Reporter solutions in a tube were heated at 90 °C for 5 min, then cooled down to 20 °C over about 1 h. The fluorescence of the reporter solution at an initial state was measured, and then an input strand was added. Excitation and emission wavelengths of FAM were 488 nm and 520 nm, respectively.

Calculation of the reaction rate of strand displacement reaction

The reaction kinetics are assumed to be one-step second-order reactions between the input strand (In) and reporter complex (R) as shown in Figure 3-3.



During the reaction, the input strand (In) and reporter complex (R) combine to form a waste complex (w) and released fluorophore strand (F). This reaction proceeds with the reaction rate constant k .

The reaction used the following rate equation:

$$\frac{d[In]}{dt} = -k[In][R] \quad (2)$$

When $[In] \neq [R]$, yielded:

$$[R] = \frac{[R]_0([R]_0 - [In]_0)}{[R]_0 - [In]_0 e^{([In]_0 - [R]_0)kt}} \quad (3)$$

The mass balance equations is:

$$[F] = [R]_0 - [R] \quad (4)$$

When combined, equations (3) and (4) yielded:

$$[F] = [R]_0[In]_0 \frac{1 - e^{([In]_0 - [R]_0)kt}}{[R]_0 - [In]_0 e^{([In]_0 - [R]_0)kt}} \quad (5)$$

Fluorescence intensity I is calculated as follows:

$$\begin{aligned} I &= \frac{[R]}{[R]_0} I_R + \frac{[F]}{[R]_0} I_F \\ &= \left(1 - \frac{[F]}{[R]_0}\right) I_R + \frac{[F]}{[R]_0} I_F \end{aligned} \quad (6)$$

Where I_R is the fluorescence intensity of the quenched reporter complex and I_F is the measured fluorescence intensity at the reaction completion.

The rate constant k was fitted using least-squares method between the fluorescence value of the data at the time t and calculated fluorescence value I at time t .

3-7. Reference

1. Yurke, B.; Turberfield, A. J.; Mills, A. P.; Simmel, F. C.; Neumann, J. L., A DNA-fuelled molecular machine made of DNA. *Nature* **2000**, *406* (6796), 605-608.
2. Shin, J.-S.; Pierce, N. A., A Synthetic DNA Walker for Molecular Transport. *J. Am. Chem. Soc.* **2004**, *126* (35), 10834-10835.
3. Choi, H. M. T.; Chang, J. Y.; Trinh, L. A.; Padilla, J. E.; Fraser, S. E.; Pierce, N. A., Programmable in situ amplification for multiplexed imaging of mRNA expression. *Nat. Biotechnol.* **2010**, *28* (11), 1208-1212.
4. Green, Alexander A.; Silver, Pamela A.; Collins, James J.; Yin, P., Toehold Switches: De-Novo-Designed Regulators of Gene Expression. *Cell* **2014**, *159* (4), 925-939.
5. Chappell, J.; Westbrook, A.; Verosloff, M.; Lucks, J. B., Computational design of small transcription activating RNAs for versatile and dynamic gene regulation. *Nat. Commun.* **2017**, *8* (1), 1051.
6. Oesinghaus, L.; Simmel, F. C., Switching the activity of Cas12a using guide RNA strand displacement circuits. *Nat. Commun.* **2019**, *10* (1), 2092.
7. McKenzie, L. K.; El-Khoury, R.; Thorpe, J. D.; Damha, M. J.; Hollenstein, M., Recent progress in non-native nucleic acid modifications. *ChSRv* **2021**, *50* (8), 5126-5164.
8. Morihira, K.; Kasahara, Y.; Obika, S., Biological applications of xeno nucleic acids. *Mol. Biosyst.* **2017**, *13* (2), 235-245.
9. K. Singh, S.; A. Koshkin, A.; Wengel, J.; Nielsen, P., LNA (locked nucleic acids): synthesis and high-affinity nucleic acid recognition. *Chem. Commun.* **1998**, (4), 455-456.
10. Olson, X.; Kotani, S.; Yurke, B.; Graugnard, E.; Hughes, W. L., Kinetics of DNA Strand Displacement Systems with Locked Nucleic Acids. *The Journal of Physical Chemistry B* **2017**, *121* (12), 2594-2602.
11. Nielsen, P. E.; Egholm, M.; Berg, R. H.; Buchardt, O., Sequence-Selective Recognition of DNA by Strand Displacement with a Thymine-Substituted Polyamide. *Science* **1991**, *254* (5037), 1497-1500.
12. Wittung, P.; Nielsen, P. E.; Buchardt, O.; Egholm, M.; Norde'n, B., DNA-like double helix formed by peptide nucleic acid. *Nature* **1994**, *368* (6471), 561-563.
13. Kabza, A. M.; Young, B. E.; Sczepanski, J. T., Heterochiral DNA Strand-Displacement Circuits. *J. Am. Chem. Soc.* **2017**, *139* (49), 17715-17718.
14. Kundu, N.; Young, B. E.; Sczepanski, J. T., Kinetics of heterochiral strand displacement from PNA–DNA heteroduplexes. *Nucleic Acids Res.* **2021**, *49* (11), 6114-6127.
15. Kashida, H.; Murayama, K.; Toda, T.; Asanuma, H., Control of the Chirality and Helicity of Oligomers of Serinol Nucleic Acid (SNA) by Sequence Design. *Angew. Chem. Int. Ed.* **2011**, *50* (6), 1285-1288.
16. Murayama, K.; Kashida, H.; Asanuma, H., Acyclic l-threoninol nucleic acid (l-aTNA) with suitable structural rigidity cross-pairs with DNA and RNA. *Chem. Commun.* **2015**, *51* (30), 6500-6503.

17. Asanuma, H.; Toda, T.; Murayama, K.; Liang, X.; Kashida, H., Unexpectedly Stable Artificial Duplex from Flexible Acyclic Threoninol. *J. Am. Chem. Soc.* **2010**, *132* (42), 14702-14703.
18. Murayama, K.; Nagao, R.; Asanuma, H., D-aTNA Circuit Orthogonal to DNA Can Be Operated by RNA Input via SNA. *ChemistrySelect* **2017**, *2* (20), 5624-5627.
19. Chen, Y.; Nagao, R.; Murayama, K.; Asanuma, H., Orthogonal Amplification Circuits Composed of Acyclic Nucleic Acids Enable RNA Detection. *J. Am. Chem. Soc.* **2022**, *144* (13), 5887-5892.
20. Zhang, D. Y.; Winfree, E., Control of DNA Strand Displacement Kinetics Using Toehold Exchange. *J. Am. Chem. Soc.* **2009**, *131* (47), 17303-17314.
21. Wang, B.; Thachuk, C.; Ellington, A. D.; Winfree, E.; Soloveichik, D., Effective design principles for leakless strand displacement systems. *Proceedings of the National Academy of Sciences* **2018**, *115* (52), E12182-E12191.
22. Makino, K.; Hattori, Y.; Kashida, H.; Asanuma, H., Preparation of Artificial Hexaplex Composed of Non-Natural Nucleic Acid. *Current Protocols* **2021**, *1* (4), e106.
23. Asanuma, H.; Shirasuka, K.; Takarada, T.; Kashida, H.; Komiyama, M., DNA-Dye Conjugates for Controllable H* Aggregation. *J. Am. Chem. Soc.* **2003**, *125* (8), 2217-2223.

3-8. Appendixes

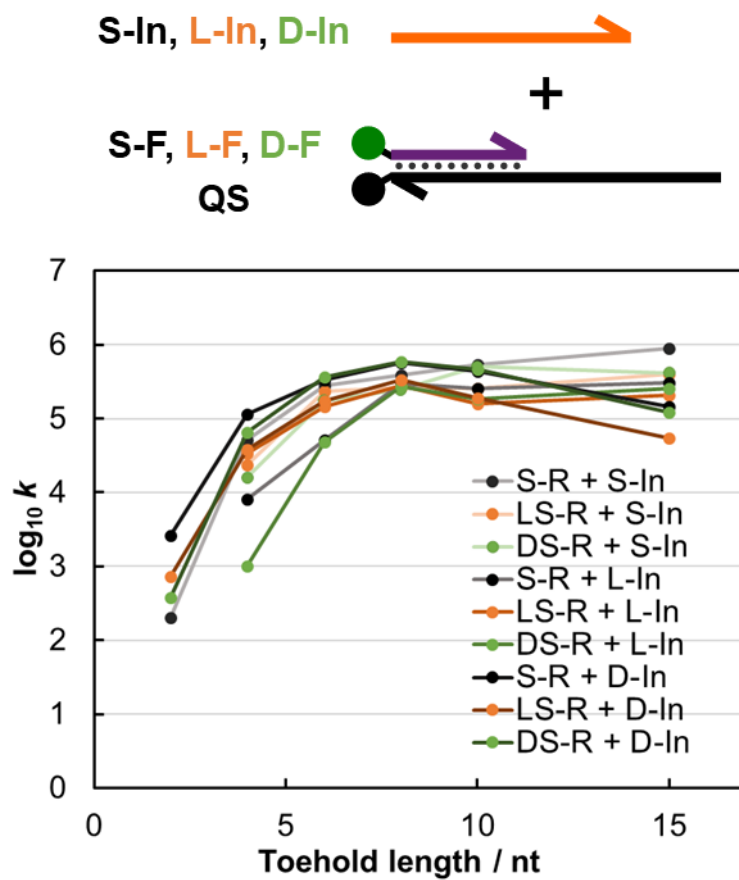


Figure S3-1. Summary of strand displacement rate constants k plotted against the toehold length. The y-axis shows the base 10 logarithm as shown in Figure 3-4. Conditions: $[R] = 50\text{-}150$ nM, $[In] = 75\text{-}1500$ nM, TE/Mg²⁺ buffer (12.5 mM MgCl₂, 10 mM Tris-HCl (pH 8.0), 1.0 mM EDTA), 1 μ M dT₂₀ carrier strands, 25 °C, Ex. = 488 nm, Em. = 520 nm.

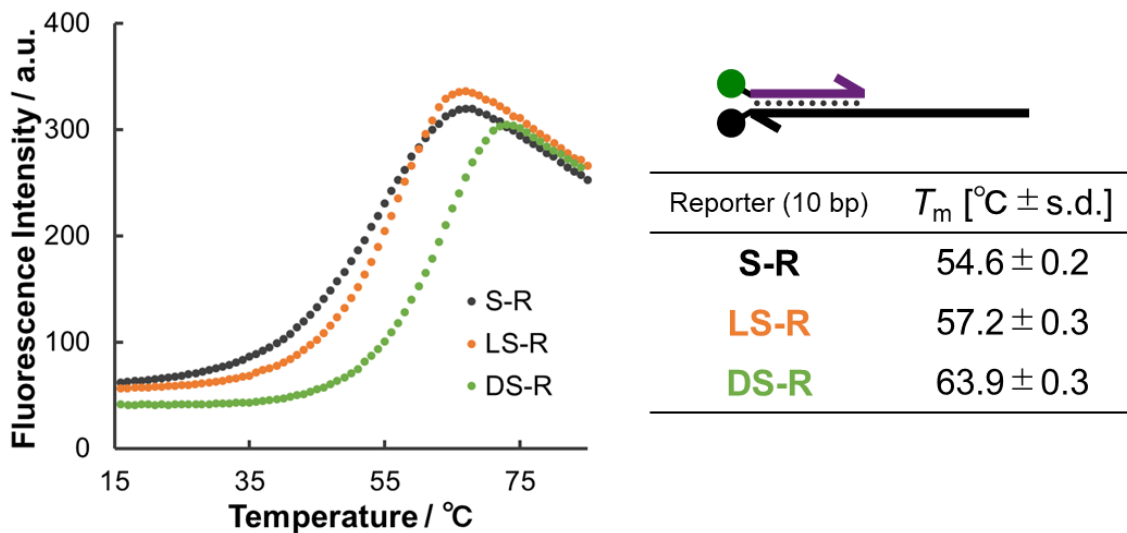


Figure S3-2. Fluorescence melting curves of 10 bp reporter complex, of SNA homo-duplex (S-R) (black), L-aTNA/SNA hetero-duplex (LS-R) (orange), and D-aTNA/SNA hetero-duplex (DS-R) (green). Conditions: [R] = 50 nM, TE/Mg²⁺ buffer (12.5 mM MgCl₂, 10 mM Tris-HCl (pH 8.0), 1.0 mM EDTA), 1 μM dT₂₀ carrier strands, Ex. = 488 nm, Em. = 520 nm.

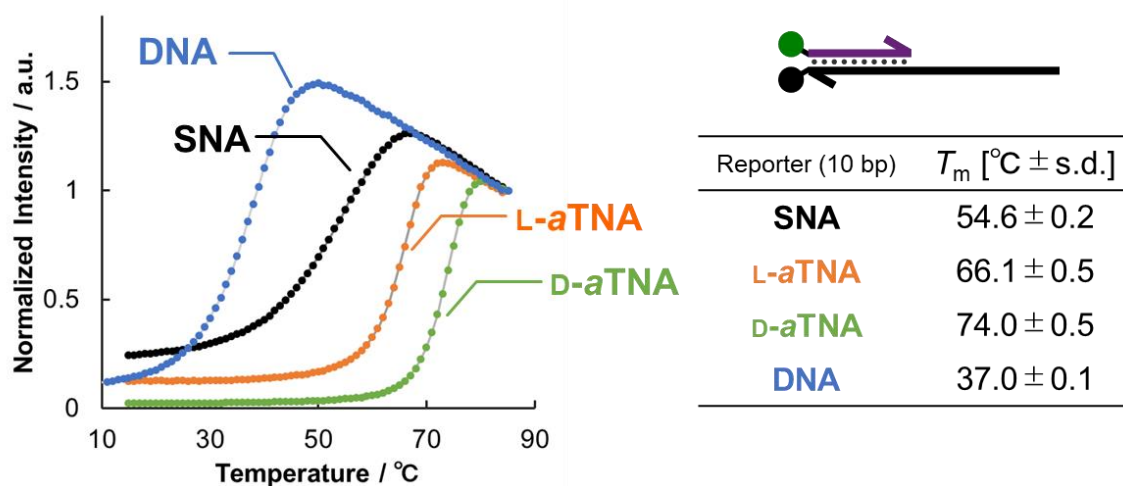


Figure S3-3. Fluorescence melting curves of 10 bp reporter complex, of SNA (black), L-aTNA (orange), D-aTNA (green), and DNA (blue). Fluorescence intensities were normalized by the intensity at 90 °C. Conditions: [R] = 50 nM, TE/Mg²⁺ buffer (12.5 mM MgCl₂, 10 mM Tris-HCl (pH 8.0), 1.0 mM EDTA), 1 μM dT₂₀ carrier strands, Ex. = 488 nm, Em. = 520 nm.

Table S3-1. Sequences of each nucleic acid.

	Name	Sequence (X→Y)	XNA	
Input	L-In15	3' CCTAC TACCG CTTGA CACTT ATTAC	1' L-aTNA	
	L-In10	3' CCTAC TACCG CTTGA CACTT	1' L-aTNA	
	L-In8	3' CCTAC TACCG CTTGA CAC	1' L-aTNA	
	L-In6	3' CCTAC TACCG CTTGA C	1' L-aTNA	
	L-In4	3' CCTAC TACCG CTTG	1' L-aTNA	
	L-In2	3' CCTAC TACCG CT	1' L-aTNA	
	S-In15	(S) CCTAC TACCG CTTGA CACTT ATTAC	(R) SNA	
	S-In10	(S) CCTAC TACCG CTTGA CACTT	(R) SNA	
	S-In8	(S) CCTAC TACCG CTTGA CAC	(R) SNA	
	S-In6	(S) CCTAC TACCG CTTGA C	(R) SNA	
	S-In4	(S) CCTAC TACCG CTTG	(R) SNA	
	S-In2	(S) CCTAC TACCG CT	(R) SNA	
	D-In15	1' CCTAC TACCG CTTGA CACTT ATTAC	3' D-aTNA	
	D-In10	1' CCTAC TACCG CTTGA CACTT	3' D-aTNA	
	D-In8	1' CCTAC TACCG CTTGA CAC	3' D-aTNA	
	D-In6	1' CCTAC TACCG CTTGA C	3' D-aTNA	
	D-In4	1' CCTAC TACCG CTTG	3' D-aTNA	
	D-In2	1' CCTAC TACCG CT	3' D-aTNA	
	DNA-In15	5' CCTAC TACCG CTTGA CACTT ATTAC	3' DNA	
	DNA-In10	5' CCTAC TACCG CTTGA CACTT	3' DNA	
	DNA-In8	5' CCTAC TACCG CTTGA CAC	3' DNA	
	DNA-In6	5' CCTAC TACCG CTTGA C	3' DNA	
	DNA-In4	5' CCTAC TACCG CTTG	3' DNA	
	DNA-In2	5' CCTAC TACCG CT	3' DNA	
	F	L-F	3' (FAM) CCTAC TACCG	1' L-aTNA
		S-F	(S) (FAM) CCTAC TACCG	(R) SNA
		D-F	1' (FAM) CCTAC TACCG	3' D-aTNA
D-F_Cy3		1' (Cy3) CCTAC TACCG	3' D-aTNA	
DNA-F		5' (FAM) CCTAC TACCG	3' DNA	
Q	L-Q	3' GTAAT AAGTG TCAAG CGGTA GTAGG (DabcyI)	1' L-aTNA	
	S-Q	(S) GTAAT AAGTG TCAAG CGGTA GTAGG (DabcyI)	(R) SNA	
	D-Q	1' GTAAT AAGTG TCAAG CGGTA GTAGG (DabcyI)	3' D-aTNA	
	DNA-Q	5' GTAAT AAGTG TCAAG CGGTA GTAGG (DabcyI)	3' DNA	

L-aTNA and SNA oligomers were purchased from Hokkaido System Science Co., Ltd.

DNA oligomers were purchased from Integrated DNA Technologies.

Cy3 was incorporated with Cyanine 3 Phosphoramidite (Glen Research, 10-5913).

FAM was incorporated with 5'-Fluorescein Phosphoramidite (Glen Research, 10-5901).

DabcyI was incorporated with 3'-DabcyI CPG (Glen Research, 20-5912).

Table S3-2. Kinetics of heterochiral strand displacement reaction with different toehold lengths.

		[Reporter]	[Input]	k [$\times 10^6 \text{ M}^{-1} \text{ s}^{-1}$]
S-R	S-In2	150 nM	1500 nM	0.0002
	S-In4	50 nM	75 nM	0.051
	S-In6	50 nM	75 nM	0.277
	S-In8	50 nM	75 nM	0.391
	S-In10	50 nM	75 nM	0.541
	S-In15	50 nM	75 nM	0.898
LS-R	S-In4	50 nM	75 nM	0.024
	S-In6	50 nM	75 nM	0.236
	S-In8	50 nM	75 nM	0.267
	S-In10	50 nM	75 nM	0.257
	S-In15	50 nM	75 nM	0.397
DS-R	S-In4	50 nM	75 nM	0.016
	S-In6	50 nM	75 nM	0.174
	S-In8	50 nM	75 nM	0.247
	S-In10	50 nM	75 nM	0.502
	S-In15	50 nM	75 nM	0.413
S-R	L-In4	50 nM	75 nM	0.008
	L-In6	50 nM	75 nM	0.052
	L-In8	50 nM	75 nM	0.295
	L-In10	50 nM	75 nM	0.257
	L-In15	50 nM	75 nM	0.304
LS-R	L-In4	50 nM	75 nM	0.034
	L-In6	50 nM	75 nM	0.144
	L-In8	50 nM	75 nM	0.279
	L-In10	50 nM	75 nM	0.159
	L-In15	50 nM	75 nM	0.208
DS-R	L-In4	50 nM	75 nM	0.001
	L-In6	50 nM	75 nM	0.048
	L-In8	50 nM	75 nM	0.270

	L-In10	50 nM	75 nM	0.183
	L-In15	50 nM	75 nM	0.254
S-R	D-In2	150 nM	1500 nM	0.0026
	D-In4	50 nM	75 nM	0.116
	D-In6	50 nM	75 nM	0.333
	D-In8	50 nM	75 nM	0.566
	D-In10	50 nM	75 nM	0.431
	D-In15	50 nM	75 nM	0.144
	LS-R	D-In2	150 nM	1500 nM
D-In4		50 nM	75 nM	0.038
D-In6		50 nM	75 nM	0.174
D-In8		50 nM	75 nM	0.333
D-In10		50 nM	75 nM	0.191
D-In15		50 nM	75 nM	0.054
DS-R		D-In2	150 nM	1500 nM
	D-In4	50 nM	75 nM	0.065
	D-In6	50 nM	75 nM	0.361
	D-In8	50 nM	75 nM	0.581
	D-In10	50 nM	75 nM	0.470
	D-In15	50 nM	75 nM	0.120

Table S3-3. Kinetics of homo-duplex strand displacement reaction with different toehold lengths.

		[Reporter]	[Input]	k [$\times 10^6 \text{ M}^{-1} \text{ s}^{-1}$]
SNA-R	S-In2	150 nM	1500 nM	0.0002
	S-In4	50 nM	75 nM	0.051
	S-In6	50 nM	75 nM	0.277
	S-In8	50 nM	75 nM	0.391
	S-In10	50 nM	75 nM	0.541
	S-In15	50 nM	75 nM	0.898
L-aTNA-R	L-In2	150 nM	1500 nM	0.0001
	L-In4	100 nM	1000 nM	0.0055
	L-In6	50 nM	75 nM	0.028
	L-In8	50 nM	75 nM	0.064
	L-In10	50 nM	75 nM	0.103
	L-In15	50 nM	75 nM	0.051
D-aTNA-R	D-In2	150 nM	1500 nM	0.0002
	D-In4	100 nM	1000 nM	0.019
	D-In6	50 nM	75 nM	0.226
	D-In8	50 nM	75 nM	0.278
	D-In10	50 nM	75 nM	0.276
	D-In15	50 nM	75 nM	0.088
DNA-R	DNA-In2	150 nM	1500 nM	0.0047
	DNA-In4	50 nM	500 nM	0.098
	DNA-In6	50 nM	75 nM	0.572
	DNA-In8	50 nM	75 nM	0.841
	DNA-In10	50 nM	75 nM	1.355
	DNA-In15	50 nM	75 nM	1.943

Table S3-4. Thermodependency of strand displacement reaction.

$k [\times 10^6 \text{ M}^{-1} \text{ s}^{-1}]$	17 °C	21 °C	25 °C	29 °C	35 °C	45°C
SNA	0.128	0.213	0.277	0.324	0.351	0.349
L-aTNA	0.006	0.015	0.028	0.065	0.144	0.519
D-aTNA	0.043	0.118	0.226	0.466	0.709	2.520
DNA	0.508	0.553	0.572	0.746		

List of Publications

(1) Makino, K.; Susaki, E. A.; Endo, M.; Asanuma, H.; Kashida, H., Color-Changing Fluorescent Barcode Based on Strand Displacement Reaction Enables Simple Multiplexed Labeling. J. Am. Chem. Soc. 2022, 144 (4), 1572-1579.

List of Presentations

International conference

Oral

(1) Koki Makino, Hiroyuki Asanuma, Hiromu Kashida. “Development of fluorescent barcode utilizing strand exchange reaction of nucleic acids” The 2021 International Chemical Congress of Pacific Basin Societies, December 17-22, Virtual, Session#102 No.8 (2021).

Poster

(2) Koki Makino, Hiroyuki Asanuma, Hiromu Kashida. “Multiplexed Imaging with Color-Changing Fluorescent Barcode Based on Strand Displacement Reaction” The 49th International Symposium on Nucleic Acids Chemistry (ISNAC 2022), November 2-4, Tokyo (JAPAN), 1P-57 (2022).

Internal conference

22 presentations. Omitted.

List of Awards

- (1) 「日本化学会東海支部長賞」 日本化学会東海支部（卒業論文発表会）2018, Mar.
- (2) 「高分子学会東海支部 東海高分子優秀学生発表賞」 第49回中部化学関係学協会
支部連合秋季大会 2018, Nov.
- (3) 「東海高分子研究会学生研究奨励賞」 第169回東海高分子研究会講演会（夏期合
宿）2019, Aug.
- (4) 「優秀ポスター賞」 第13回バイオ関連化学シンポジウム 2019, Sep.
- (5) 「名大鏡友会賞」 名古屋大学修士論文発表会 2020, Mar.
- (6) 「FIBER 核酸化学学生優秀ポスター賞」 FIBER 日本核酸化学会若手フォーラム
2021, Aug.
- (7) 「学生講演賞」 日本化学会第102春季年会(2022) 2022, Apr.
- (8) 「博士学術賞」 名大鏡友会 2022, Oct.
- (9) 「ISNAC Outstanding Poster Award」 ISNAC2022 2022, Nov.

Acknowledgment

The present article is a thesis for application of a doctoral degree at the Department of Biomolecular Engineering, Graduate School of Engineering, Nagoya University. All the study work was conducted under the direction of Professor Hiroyuki Asanuma from April 2017 to March 2023.

I would particularly like to thank Prof. Hiroyuki Asanuma, who is my supervisor. I have had a lot of support and encouragement from him. He taught me how to think logically, how to express my ideas to other researchers, and how to enjoy research, especially DNA chemistry and photochemistry.

I would like to express my deepest appreciation to Associate Professor Hiromu Kashida, who has discussed most with me about my work, presentation, and any aspects of my research life during this six year. He provided me many constructive comments and suggestions to progress this work.

I also especially thank Assistant Professor Keiji Murayama, who gave me a lot of technical supports including the repair of equipment. I have talked and discussed with him easily and received valuable comments.

I thank Associate Professor Yukiko Kamiya, who provided a lot of advises in the application of CCFB to cellular biology.

I would like to say thanks to my co-worker in Asanuma Laboratory, Dr. Yuhei Yamano, Dr. Yanglingzhi Chen, Mr. Zehua Liu, Ms. Hikari Okita, Mr. Hidenori Azuma, and other members for my research progress.

I am also greatly indebted to “SUMBOR SCHOLARSHIP” and “Interdisciplinary Frontier Next-Generation Researcher Program of the Tokai Higher Education and Research System.” for their financial support.

I would also like to give special thanks to Professor Hiroshi Murakami and Professor Kentaro Tanaka for giving helpful comments and suggestions on this thesis.

Finally, I would like to thank my mother and father for their understanding and support.